Development and assessment of advanced continuum models for drying porous media on the basis of discrete pore network simulations

Dissertation

zur Erlangung des akademischen Grades

Doktoringenieur

(Dr.-Ing.)

von M.Sc. Faeez Ahmad

geb. am 05.05.1988 in Lahore, Pakistan

genehmigt durch die Fakultät für Verfahrens- und Systemtechnik

der Otto-von-Guericke-Universität Magdeburg

Promotionskommission: Prof. Dr. Berend van Wachem (Vorsitz)

PD. Dr.-Ing. habil. Abdolreza Kharaghani (Betreuer, Gutachter)

Prof. Dr.-Ing. habil. Evangelos Tsotsas (Gutachter)

Prof. Dr. Marc Prat (Gutachter)

eingereicht am: 30.05.2022

Promotionskolloquium am 07.10.2022

Declaration

I hereby declare that I prepared the dissertation with the title:

"Development and assessment of advanced continuum models for drying porous media on the basis of discrete pore network simulations"

without inadmissible assistance and without the use of any aids other than those indicated. Facts or ideas taken from other sources, either directly or indirectly, have been marked as such. In particular, I did not use the services of a commercial graduation consultation. Further, I have not made payments to third parties either directly or indirectly for any work connected with the contents of the submitted dissertation.

The work has not so far been submitted either in Germany or abroad in same or similar form as a dissertation and has also not yet been published as a whole.

Magdeburg, May, 2022

M.Sc. Faeez Ahmad

Abstract

The process of drying of porous media is a subject of active research and development in the industry and the scientific community due to its various applications in fields such as food processes, production of fuel cells and batteries, chemical process engineering, soil salinization, and salt weathering in buildings. The modeling approaches that are used to simulate the process of drying in porous media are traditionally based on continuum modeling, which considers the transport phenomena at the macroscopic scale. Another approach which has seen significant development in the last two decades is a discrete pore scale approach known as pore network modeling. While pore network modeling describes the pore scale phenomena based on first principles, its application to large sized porous media is limited by its very high computational cost. On the other hand, as the continuum modeling approach considers averaged behavior of the transport through conservation equations that are solved for a much larger volume, the continuum models are very robust and fast. The idea behind this thesis is to use the pore network simulations to assess and overcome the prediction capability of the existing continuum models for drying capillary porous media.

In this thesis, we consider drying of rigid capillary porous medium (pore size in the range of micrometers) at ambient conditions (considering drying as an isothermal process). In such capillary porous media, the sorption phenomenon is negligible and the material is considered as non-hygroscopic. In this context, it has been shown by pore network simulations reported in recent literature that the traditional assumption of local equilibrium between the liquid and vapor phases is not valid, as significant non-equilibrium effects are observed at the macroscopic scale. In this context, this work aims to develop a continuum model of drying that captures the non-local equilibrium effect. This continuum model will be superior to the commonly used one-

equation continuum model that regards saturation as the only process variable. It will account for the liquid and vapor phase transport by explicitly considering one transport equation for each of these phases. The two equations of this continuum model (referring to saturation and partial vapor pressure as the process variables) will be coupled by a source/sink term which should capture the non-local equilibrium phase change. This two-equation continuum model should also address other drawbacks of the one-equation continuum model and describe more realistically the physics of drying at the macroscopic scale. We will approach this problem in two successive steps.

In the first step, we will focus on a simplified situation, upscaling the process of evaporation and vapor diffusion in a partially saturated porous medium, in which the liquid phase is immobile. We will formulate and validate a two-equation continuum model that captures important physical effects (such as non-local equilibrium effect) for the limiting case of immobile liquid phase. The two-equation CM will be formally derived from the upscaling of the pore-scale mass conservation equations of the liquid and vapor phases. This will enable us to obtain a deeper understanding and interpretation of the effective transport parameters and will also lead to the consideration of interfacial area as a macroscopic parameter of drying. In the next step, we will address the more complex situation of a fully saturated porous medium where the macroscopic capillary transport in the liquid phase is also taken into account. Here, we will address the modeling of mass transport at the porous medium surface (which is still an unresolved issue) by presenting correlations for the boundary conditions of the liquid and vapor transport equations. We will verify the solution of the two-equation continuum model through independent reproduction of phase distributions, the drying kinetics and the non-local equilibrium effect.

We will also evaluate the commonly used continuum model of drying with dissolved solute transport based on the classical macroscopic advective-diffusive transport equation by means of pore network simulations. The analysis will be focused on the first drying period (till the porous medium surface stays wet), since the most likely place of crystallization of the dissolved solute is the evaporative surface. The analysis

will study the impact of liquid fragmentation process on the dynamics of solute transport. With the help of pore network simulations, the transport phenomena at the surface will be studied based on 2D mapping of the liquid connectivity and solute concentration and Monte Carlo PNM simulations will stochastically characterize the respective pore scale effects.

Overall, the work focuses on various fundamental aspects of drying capillary porous media and aims at bridging the gap between microscopic discrete models of drying and macroscopic continuum models. The insights presented in this work are expected to empower our ability of improving drying processes and the respective products, with a plethora of potential applications in practice.

Kurzzusammenfassung

Der Prozess der Trocknung poröser Medien ist aufgrund seiner vielfältigen Anwendungen in Bereichen wie Lebensmitteltechnik, Herstellung von Brennstoffzellen und Batterien, chemische Verfahrenstechnik, Bodenversalzung und Verwitterung in Gebäuden Gegenstand aktiver Forschung und Entwicklung in Industrie und Wissenschaft. Die Modellierungsansätze, die verwendet werden, um den Trocknungsprozess in porösen Medien zu simulieren, basieren traditionell auf der Kontinuumsmodellierung, die die Transportphänomene im makroskopischen Maßstab berücksichtigt. Ein weiterer Ansatz, der in den letzten zwei Jahrzehnten eine bedeutende Entwicklung erfahren hat, ist ein Ansatz auf diskreter Porenskala, der als Porennetzwerkmodellierung bekannt ist. Während die Porennetzwerkmodellierung porenskalige Vorgänge basierend auf ersten Prinzipien beschreibt, ist ihre Anwendung auf großformatige poröse Medien durch ihren sehr hohen Rechenaufwand begrenzt. Da der Kontinuumsansatz andererseits das gemittelte Verhalten des Transports durch Erhaltungsgleichungen berücksichtigt, die für ein viel größeres Volumen gelöst werden, sind die Kontinuumsmodelle sehr robust und schnell. Die Idee hinter dieser Arbeit ist, die Porennetzwerksimulationen zu verwenden, um die Voraussagefähigkeit der bestehenden Kontinuumsmodelle für die Trocknung kapillarporöser Medien zu bewerten und ihre Einschränkungen zu überwinden.

In dieser Arbeit betrachten wir die Trocknung von starren kapillarporösen Medien (Porengröße im Mikrometerbereich) bei Umgebungsbedingungen (unter Annahme isothermer Bedingungen). In solchen kapillarporösen Medien ist die Sorption vernachlässigbar und das Material wird als nicht hygroskopisch angesehen. In diesem Zusammenhang wurde durch Porennetzwerksimulationen aus der neueren Literatur gezeigt, dass die traditionelle Annahme eines lokalen Gleichgewichts zwischen der

flüssigen und der Dampfphase nicht gültig ist, da signifikante Nichtgleichgewichtseffekte im makroskopischen Maßstab beobachtet werden. Daher zielt diese Arbeit darauf ab, ein Kontinuumsmodell der Trocknung zu entwickeln, das lokale Ungleichgewichte erfasst. Dieses Kontinuumsmodell wird dem üblicherweise verwendeten Eingleichungs-Kontinuumsmodell überlegen sein, das die Sättigung als einzige Zustandsvariable betrachtet. Es wird den Flüssigkeits- und Dampftransport durch eine explizite Transportgleichung für jede dieser Phasen berücksichtigten. Die beiden Gleichungen dieses Kontinuumsmodells (mit Sättigung und Partialdampfdruck als Zustandsvariablen) werden durch einen Quellen- bzw. Senkenterm gekoppelt, der das lokale Ungleichgewicht erfassen soll. Dieses Zweigleichungen-Kontinuumsmodell sollte auch andere Nachteile des Eingleichungs-Kontinuumsmodells adressieren und die Physik des Trocknens im makroskopischen Maßstab realistischer beschreiben. Wir werden uns diesem Problem in zwei aufeinanderfolgenden Schritten nähern.

Im ersten Schritt konzentrieren wir uns auf eine vereinfachte Situation, indem wir den Prozess der Verdeenstung und Dampfdiffusion in einem teilgesättigten porösen Medium, in dem die flüssige Phase immobil ist, hochskalieren. Wir werden ein Kontinuumsmodell mit zwei Gleichungen formulieren und validieren, das wichtige physikalische Effekte (wie den lokalen Ungleichgewichtseffekt) für den Grenzfall der immobilen flüssigen Phase erfasst. Das Zweigleichungen-Modell wird formal aus der Hochskalierung der Massenerhaltungsgleichungen der Porenskala für Flüssigkeit und Dampfphase abgeleitet. Dies wird uns ein tieferes Verständnis und eine bessere Interpretation der effektiven Transportparameter ermöglichen und auch zur Phasengrenzfläche als makroskopischen Parameter der Trocknung führen. Im nächsten Schritt werden wir uns der komplexeren Situation eines vollständig gesättigten porösen Mediums widmen, bei dem auch der makroskopische Kapillartransport in der flüssigen Phase berücksichtigt wird. Hier werden wir die Modellierung des Stofftransports an der Oberfläche des porösen Mediums (die noch ein ungelöstes Problem ist) adressieren, indem wir Korrelationen für die Randbedingungen der Flüssigkeits- und Dampftransportgleichungen darstellen. Wir werden die Lösung des Zweigleichungs-Kontinuumsmodells durch unabhängige

Reproduktion der Phasenverteilungen, der Trocknungskinetik und des lokalen Ungleichgewichts verifizieren.

Wir werden auch das häufig verwendete Kontinuumsmodell der Trocknung mit Transport gelöster Stoffe basierend auf der klassischen makroskopischen advektiv-diffusiven Transportgleichung mit Hilfe von Porennetzwerksimulationen evaluieren. Die Analyse konzentriert sich auf den ersten Trocknungsabschnitt (solange die Oberfläche des porösen Mediums nass bleibt), da der wahrscheinlichste Ort der Kristallisation des gelösten Stoffes die Verdunstungsoberfläche ist. Die Analyse wird den Einfluss des Prozesses der Fragmentierung der Flüssigkeit auf die Dynamik des Transports gelöster Stoffe untersuchen. Mit Hilfe von Porennetzwerksimulationen werden die Transportvorgänge an der Oberfläche anhand von 2D-Kartierungen der Flüssigkeitskonnektivität und der Konzentration gelöster Stoffe untersucht. Monte Carlo PNM-Simulationen werden, die jeweiligen Porenskaleneffekte stochastisch charakterisieren.

Insgesamt konzentriert sich die Arbeit auf verschiedene grundlegende Aspekte der Trocknung von kapillarpörosen Medien und hat das Ziel, die Lücke zwischen mikroskopischen diskreten Modellen der Trocknung und makroskopischen Kontinuumsmodellen zu schließen. Die in dieser Arbeit vorgestellten Erkenntnisse sollen unsere Fähigkeit zur Verbesserung von Trocknungsprozessen und der entsprechenden Produkte steigern, mit einer Fülle von Anwendungsmöglichkeiten in der Praxis.

Contents

Nomenclature

Notations

A	cross-sectional area	m^2
a	specific interfacial area	m^{-1}
C	concentration	kgm^{-3}
D	diffusion coefficient	$m^2\ s^{-1}$
g	acceleration of gravity	ms^{-2}
H	network height	m
h	height	m
J	mass flow rate	$kg\ s^{-1}$
j	mass flux	$kg\ s^{-1}\ m^{-2}$
j	slice-averaged volumetric flow rate	$m^3\ s^{-1}$
k	mass exchange coefficient	m/s
k_B	Boltzmann constant	$J\ K^{-1}$
L	length	m
$\tilde{M}$	molar mass	$kg\ kmol^{-1}$
m	mass	kg
$\dot{m}$	specific evaporation rate	$kg\ m^{-3}\ s^{-1}$
n,N	numbers	-
$\mathbf{n}$	unit vector	-
P	pressure	Pa

$\tilde{R}$	universal gas constant	J kmol^{-1} K^{-1}
r	radius	m
S	saturation	-
T	temperature	K
t	time	s
U	macroscopic liquid velocity	ms^{-1}
V	macroscopic volume	m^3
$\mathbf{v}$	liquid mass average velocity	ms^{-1}
$\mathbf{w}$	velocity of liquid-gas interface	ms^{-1}
x,y,z	space coordinates	-

Greek symbols

γ	surface tension	Nm^{-1}
ε	porosity	-
θ	equilibrium contact angle	grad
κ	absolute permeability	m^2
κ_r	relative permeability	-
μ	statistical probability	-
μ_l	liquid phase viscosity	Pa s
ξ	normalized network depth	-
ρ	density	kgm^{-3}
σ	accommodation coefficient	-

Superscripts and subscripts

a	air
abs	absolute
atm	atmospheric
bl	boundary layer
c	capillary
cth	capillary threshold
D	Darcian
dry	dry
eff	effective
g	gas
ic	isolated cluster
ini	initial
irr	irreducible
l	liquid
loc	local
mc	main cluster
min	minimum
net	network
ref	reference
rel	relative
res	residual
sat	saturation
s	solute

sur,surf	surface
t	throat
v	vapor
w,wet	wet
∞	ambient
0	original

Abbreviations

BT	breakthrough point
Ca	capillary number
CM	continuum model
CRP	constant rate period
CFD	computational fluid dynamics
CV	control volume
FRP	falling rate period
IP	invasion percolation
LE	local equilibrium
LBM	Lattice Boltzmann method
NLE	non-local equilibrium
PN	pore network
Pe	Péclet number
REV	representative elementary volume
RFP	receding front period

Chapter 1

Introduction

1.1 Overview

A porous medium consists of a solid matrix and void volume in the form of interconnected pores. The degree of connectivity of the pores and the variation in the pore sizes is material dependent. Some examples of naturally existing porous materials include soil, rocks, fruits and vegetables. Synthetically produced porous materials include construction materials, such as bricks, paper, catalyst supports, electrodes, and the electrolyte membrane in fuel cells. A porous material is characterized mainly by its porosity (ratio of the void volume to the total bulk volume of the material), pore size distribution (degree of overall variation and distribution of the size of pores) and connectivity of the pores. Also, the shape of the individual pores can be an important parameter. The pores are usually randomly distributed with different shapes and sizes within the solid matrix leading to an irregularly structured material. The structural characteristics of the porous medium play a direct role in the transport and distribution of fluids through it.

One of the most important transport processes within porous media is the process of drying. In the context of multi-phase flow, the process of drying can also be referred to as a two-phase flow process coupled with phase transition. Owing to its numerous complexities, it has been the subject of scientific research since many decades. The method of drying can entail freeze drying, vacuum drying, dielectric drying or, most usually, convective drying; either standalone or in combination with one another. In

this thesis, we consider convective drying, where the wet porous medium is exposed to sufficiently dry fresh air that acts as the drying agent.

In convective drying, after the material subject to drying has been sufficiently warmed up by the air, drying is initiated. The process of drying is classically divided into two stages, namely: the first drying period and the second drying period. In the first drying period, which is also referred to as constant rate period (CRP), the surface of the material stays sufficiently wet and the liquid evaporates at a constant rate. The drying rate in the first drying period is a function of external conditions such as temperature, pressure, humidity of the drying air and its flow velocity. For a capillary porous medium, the surface stays wet until the viscous resistance in the liquid phase dominates the capillary forces (which are responsible for transport of liquid to the surface). Once, the surface dries out, the evaporation rate drops as a result of increase in the mass transfer resistance associated with vapor diffusion through the subsurface layers of the porous medium. During the entire process of drying, the transport phenomena can be influenced by various forces such as capillarity, gravity and viscous forces. The various environmental and industrial applications of drying range from soil physics, food processes and chemical engineering applications to many other industrial uses, see, e.g., Mujumdar (2014).

Another important aspect in the drying of porous media is the drying in the presence of dissolved solute, which is still a topic of active research due to its diverse complexities and several environmental and engineering applications. The drying induced capillary transport of the dissolved solute towards the evaporation sites leads to the buildup of a concentration gradient in the liquid, which results in a simultaneous back-diffusion of the solute. Once the concentration has reached the solubility limit, the solute can precipitate into solid crystals. Interestingly, on one hand, the process of crystallization is undesirable, for example in construction bricks (Rijniers et al., 2005; Shahidzadeh-Bonn et al., 2010); On the other hand, there are various industrial processes where the formation of crystals is a desirable process, such as in the production of catalysts (Komiyama, 1985). The understanding of the transport phenomenon of the dissolved solute is important in addressing problems

like soil salinization (Chen, 1992; Sghaier et al., 2009) and salt weathering in building materials (Goudie et al., 2010).

Due to its various aforementioned practical aspects, the research on the understanding of drying and two-phase flow in porous media is still relevant and active especially in the context of thin porous media (Prat et al., 2015; Vorhauer et al., 2018), which is a rapidly emerging field with applications in batteries (Altaf et al., 2020), fuel cells (Carrère et al., 2020; García-Salaberri et al., 2015; Médici et al., 2013) and loop heat pipes (Le et al., 2016).

The research on the modeling of drying dates back to the beginning of the twentieth century. The more classical approaches are based on continuum modeling where the porous medium is considered as a fictitious continuum. The most basic notion towards modeling of drying in porous media is the so-called diffusion theory (Sherwood, 1929). This was a rather overly simplistic approach, which lacked the distinct consideration of the important pore scale mechanisms such as gravity, capillarity, external pressure, thermal effects and viscosity. Over time, this diffusion-based treatment was developed into more complex and physically more realistic models. The drying model by Philip et al. (1957) presented a diffusion-based method, which in addition to the coupling of heat transfer, also considered vapor transport and capillarity in the liquid phase. Later, Luikov (1975) presented more detailed mass conversation equations on the basis of macroscopic flux relationships of each species where the gradient of total pressure was also considered. The most robust model was developed by Whitaker (1977) where the simultaneous mass and heat transfer equations were derived from the pore scale by means of volume averaging. Whitaker's model is still modern and comprehensive model, so it is the basis of the macroscopic continuum models of drying presented and discussed in this thesis.

While the continuum models are advantageous in regard of efficiency, short computational times and simpler approach (based on averaged description of the system elements), they have their limitations. For the solution of continuum model equations, the effective transport parameters need to be known a priori. These effective transport parameters (e.g. thermal conductivity, diffusivity and

permeability) that are needed to solve the continuum model equations depend on the drying conditions and the materials involved. Hence, it involves computing these parameters on the scale of the so called representative elementary volume (REV), where each REV is a local averaging volume which may consist of numerous pores in each coordinate axis. Consequently, the effective parameters represent the averaged behavior of the transport in pores contained in a REV. In principle, the size of the REV is determined such that the effective transport parameters do not vary upon further increase in the REV size. Also, there should be a clear distinction between the pore size, REV size and the total size of the system. In other words, the REV should be large enough compared to the size of the pores, but small enough compared to the total size of the system. This is classically referred to as the length scale separation rule (Whitaker, 1977).

The effective transport parameters are traditionally computed from laboratory experiments. However, performing experiments in order to compute these parameters can be challenging in many ways, e.g. by large costs and measurement times. An alternative to performing laboratory experiments is to conduct pore scale numerical simulations. Due to the recent advances in the development of numerical techniques and computational power, this has become a viable alternative to laboratory trials. Pore scale numerical models are based on first-principle heat and mass balance equations and provide detailed pore scale insights such as phase distributions, as well as pressure distributions inside the porous medium. In this context, direct numerical simulation techniques by highly resolved Computational Fluid Dynamics (CFD) or by means of the Lattice Boltzmann Method (LBM) offer the most detailed description of the intricate pore scale transport phenomena. However, they are limited in their utility when it comes to large domain sizes due to their very high computational costs. A more pragmatic approach is a discrete network modeling scheme known as pore network modeling. This approach offers a good compromise between the computational efficiency and the preservation of the fundamental physics.

In pore network models (PNMs) the pore space is discretized into an interconnected network of pores and throats. Depending on the chosen physical conditions, the degree of complexity in the PNMs can vary. Some relevant examples in direct relation with this thesis concern the drying of porous media in the capillary dominated regime, drying in the capillary-viscous regime, and drying with consideration of dissolved solute transport. Examples of the individual physical effects that can be incorporated in the PNMs refer to viscosity (Prat et al., 1999), gravity (Laurindo et al., 1996) and heat transfer (Plourde et. al., 2003; Surasani et al., 2008). Other examples include the presence of liquid films (e.g., Prat, 2007; Vorhauer et al., 2015; Yiotis et al., 2003), wetting (Rahimi et al., 2016), and drying in presence of dissolved solute (Rahimi, 2019).

In addition to the computation of the effective parameters, which are needed as input parameters to solve the macroscopic CM equations (e.g., Attari Moghaddam et al., 2017; Nowicki et al., 1992; Vorhauer et al., 2010; Kharaghani, 2020), the PNMs are also used to gain valuable insights about the importance and role of different mechanisms in the dynamics of the drying of porous media (Prat, 2002). The PNM used in this thesis is described in Chapter 2.

Apart from PNMs, another discrete approach is the bundle of capillaries model (Metzger et al., 2005; Vu et al., 2019). In the bundle of capillaries model each throat is replaced by a bundle of capillaries such that the connection between two network nodes is represented by a bundle of capillaries instead of one cylindrical throat. This approach offers more flexibility in the representation of the volume porosity and area porosity of the porous medium (Metzger, 2019). However, a disadvantage of the bundle of capillaries model is that the influence on the drying behavior of factors other than the pore size distribution cannot be analyzed. In comparison, the PNM is a more comprehensive approach to simulate the drying of porous media.

As mentioned, the PNM simulations can be used to compute effective transport parameters for macroscopic continuum models. This can be useful especially in the case of simulation of large-scale systems, where the PNM cannot be used standalone due to the high computational cost associated with the PNM. In the context of

coupling of the micro and macro scale approaches, this particular approach, where the effective parameters needed for the continuum model solution are computed from PNM simulations, can be referred to as sequential coupling. This sequential coupling approach however, has its limitations. For example, the information transfer in this approach is one-way, i.e. from micro scale to macro scale. In contrast to the sequential coupling approach, the coupling of the micro and macro scale approaches can also be achieved such that more synergy is produced, allowing us to take advantage of the strengths of both approaches. One example is the concurrent coupling (also known as real-time coupling), where two-way information exchange between the micro and the continuum scale is possible. In this approach, the interfaces at the boundary of the two systems are linked through interfacial flux and pressure distribution, see Sheng (2013) and references therein for more details on the advantages, limitations and implementation of the concurrent coupling approach. Note that in this thesis, we work with sequential coupling approach, i.e. by means of the computation of effective parameters and the development of continuum models through upscaling of the pore scale data obtained from PNM simulations.

Before discussing the concept of upscaling, it would be worth understanding the fundamental parameters that are used to quantify macroscopically the state of the system. The most important parameters are porosity, saturation, and the evaporation rate of the system. Porosity is the ratio of total void space to the total volume of the system and is therefore a macro scale parameter. Here, it is important to mention that at the pore scale, the saturation and the evaporation rate refer to the degree of occupancy of volume of a throat with water and the rate of evaporation of water from that throat, respectively. Whereas, at the macroscopic scale they correspond to the degree of occupancy of the total void space with water and the sum of evaporation rate of all the evaporating meniscus throats in the system, respectively.

The translation from pore to macro scale, of the parameters that quantify the liquid and vapor transport, is not straightforward and can require some modifications and adaptations. For example, in a drying porous medium, the diffusion of the water vapor at the pore scale is represented by the binary diffusion coefficient. However, for

the description at the macro scale, this will be replaced by the effective vapor diffusivity. Similarly, for the computation of liquid flow, the Darcy law at the pore scale is changed to the generalized Darcy law (consisting of effective permeability) at the macro scale. The capillary pressure at the scale of the individual throats is modified to the capillary pressure curve (that relates the average network saturation and the macroscopic capillary pressure) at the macroscopic scale. Apart from these parameters, there are other parameters that need to be upscaled, for example the effective solute diffusivity in the case of drying of a porous medium saturated with a saline solution.

1.2 Motivation

In the drying of porous media, it is commonly assumed that at the interface between the liquid and gas, there exists an equilibrium between the two phases such that the vapor pressure at the interface corresponds to the saturation vapor pressure. While this assumption is suitable for the liquid-gas interface at the pore-scale, it may not be appropriate for the local or REV scale, i.e. the scale at which the continuum model is discretized. For example, for hygroscopic materials (pore sizes are typically smaller than 100 nm (Geoffroy et al., 2014)), at the local scale, the partial vapor pressure varies from the saturation vapor pressure. This variation is characterized with respect to the material saturation and in the case of drying of hygroscopic porous media, the relationship between the saturation and vapor pressure is referred to as the desorption isotherm.

In the case of non-hygroscopic porous media also referred to as capillary porous media (pore sizes are typically in the order of micrometers and water exists as free liquid (Geoffroy et al., 2014)), usually local equilibrium is considered between the liquid and gas phases. However, this has been recently questioned. It has been shown that in the pore network simulations (based on capillary porous media) reported by Attari Moghaddam et al. (2017) that a noticeable non-local-equilibrium effect (NLE) is present. It was found that during drying, within the porous medium, the average vapor pressure deviated from saturation vapor pressure. This deviation from saturation vapor pressure, also referred to as NLE effect was found to be especially

significant on the porous medium surface. It was demonstrated in Attari Moghaddam et al. (2017) that similarly to the hygroscopic porous media, where the NLE effect is found to be significant (Bénet et al., 2009; Bénet et al., 1982), the NLE effect should also be considered in the simulation of drying capillary porous media.

In Attari Moghaddam et al. (2017) a CM that combines the liquid and vapor flow equations into a single equation was used to reproduce the results of drying PNM simulations. This model has only saturation as the process variable, which makes it relatively simple to implement. The moisture transport coefficient, which represents the combined or lumped diffusivity of both the liquid and vapor phases, is computed by summing up liquid and vapor phase diffusivities. While this one-equation CM led to a good reproduction of the PNM saturation profiles, there are some issues and limitations that are intrinsic to the model. For example, it requires as input, the moisture transport coefficient function, which depends on local saturation as well as on the network saturation. This entailed three functions for the moisture transport coefficient each valid for different ranges of the network saturation. As long as the porous medium surface is wet, the boundary condition, i.e. the total evaporation rate, is a function of the surface NLE function (computed from the PNM simulation results). Once the evaporative surface becomes desaturated, the relationship between the total evaporation rate and the network saturation is needed to further continue the CM solution. This implies that instead of computing the boundary condition from the physical process conditions such as the boundary layer thickness and the partial vapor pressure, the one-equation CM requires information about the drying rate from PNM simulations, either directly or in the form of a surface NLE function. Therefore, the one-equation CM is unable to independently reproduce the drying kinetics.

The factors that are discussed above strongly indicate that the one-equation CM is not suitable to simulate drying of capillary porous media due to the limitations that are inherent in its formulation. Therefore, a CM which is superior to the one-equation CM should be developed. In this regard, it is essential to capture the NLE effect that is evident from the PNM simulations of capillary drying porous media. This makes it vital that in addition to the saturation, we consider explicitly the vapor pressure as a

process variable as well. This will lead to a two-equation CM consisting of liquid and vapor phase equations, where the mass transport will be described by the simultaneous consideration of saturation and vapor pressure as the process variables.

As mentioned in Sec. 1.1, the first drying period or CRP is the period in which the drying rate is the highest, owing to the non-zero surface saturation that prevails during this period. Due to the high evaporation rate, this period is considered desirable in many industrial applications of drying, as its extension translates into savings of time and energy associated with drying. Due to this consideration, the understanding of the transport phenomena at the surface is of great importance. Also, in many applications involving drying with a dissolved solute, the understanding of dynamics of mass transfer at the surface gains more significance, as the surface is the most likely location for the formation of crystals.

In the development of the two-equation CM, one of the problems that will be addressed is the description of the mass transport at the surface at the macroscopic scale. This is because the structure of the two-equation CM demands the description of the mass transport at the surface in terms of both, the liquid and vapor phase. In other words, the solution of the two-equation CM would require individual boundary conditions for the liquid and vapor phase. This would require the development of better closure relationships between the mass transfer at the surface and the degree of saturation of the surface (Attari Moghaddam et al., 2018). As pointed out by Attari Moghaddam et al. (2018), the consideration of the non-local equilibrium effect at the surface will lead to an improved description of the transport at the surface.

When discussing the mass transport at the surface, it is vital to mention the edge effect, which refers to a sharp variation of saturation in a thin region adjacent to the surface. As indicated by experiments and PNM simulations of drying, the edge effect is an intrinsic feature of the drying of capillary porous media (Attari Moghaddam et al., 2018; Le Bray et al., 1999; Gupta et al., 2014). However, in the CMs of drying, this feature has not yet been considered. The consideration of this effect will make the CMs physically more realistic. Therefore, we should investigate whether we can capture this effect in the frame of the continuum modeling approach or not.

The study of drying of capillary porous media, where the liquid phase includes dissolved solute, is a topic of active research due to the various environmental and engineering applications. The transport of solute inside a drying porous medium is based on an interplay of advective (caused by capillary pumping of liquid towards the evaporating surface) and diffusive transport (Guglielmini et al., 2008; Huinink et al., 2002; Sghaier et al., 2007). If the solute concentration reaches the solubility limit, the solute precipitates into solid crystals. This process of crystallization can lead to undesirable effects such as material damage and changes in transport dynamics of fluid (Börnhorst et al., 2016; Larsen et al., 2017; Naillon et al., 2018; Scherer, 2004). Therefore, many researches have been conducted to understand the transport phenomena that lead to crystallization of dissolved solute (Guglielmini et al., 2008; Hidri et al., 2013; Huinink et al., 2002; Sghaier et al., 2007). These works are based on the continuum modeling (CM) approach (Whitaker, 1977), whereby the solute concentration is obtained by solving the advective-diffusive transport equation (ADE). In Pel et al. (2002) the reported results of experiments were found to be in good qualitative agreement with the solution of ADE. However, from other comparisons with experimental data (e.g., Shokri-Kuehni et al., 2018; Shokri, 2014), it has been argued that the classical macroscopic ADE might not lead to good results in the situation of drying. Therefore, in this thesis, we evaluate the ability of the classical ADE to predict solute transport under conditions of drying.

The classical macroscopic advection-diffusion CM considers the liquid phase as continuous and connected at all times. However, it is known that during the drying of capillary porous media, the liquid phase gets fragmented into a main cluster, isolated clusters and isolated single menisci (see, e.g., Moghaddam et al. (2017) and references therein). Hence, it should be analyzed as to how the assumption that the liquid phase remains connected throughout the drying process will impact the development of the solute concentration profiles.

1.3 The new work

The various negative aspects and shortcomings in the state-of-the-art macroscopic CMs that have been discussed in the previous section consist mainly of: the flawed

assumption of local equilibrium between liquid and vapor phases, the inadequate modeling of mass transport at the surface, and the missing assessment of CM for drying in the presence of dissolved solute transport. For the analysis of the CMs, we will use PNM drying simulations as a benchmark and guide. The detailed information obtained from PNM simulations will aid the mathematical derivations and the development of new closure relationships, which are involved in the process of upscaling.

In order to address the erroneous assumption of local equilibrium between liquid and vapor phase, we will work on the development of a CM that considers the NLE effect i.e. the local non-equilibrium between the liquid and gas phase. As mentioned, we will use PNM simulations for modeling insights and comparison of results. As a first step, we will consider a simplified situation in which the liquid phase is initially distributed in the form of small isolated clusters. This implies that the macroscopic transport in the liquid phase can be neglected, allowing us to focus on a situation where the mass transport occurs primarily in the vapor phase. This approach is similar to that in a previous work on the NLE effect (Ouedraogo et al., 2013), where the focus has been on hygroscopic porous medium at low saturation (i.e. soil that behaves as a hygroscopic porous medium when water content becomes very low).

The NLE CM will be derived with the help of volume averaging method. The liquid and gas phase equations will be coupled by a NLE mass exchange term. The formulation of this NLE phase change term will entail the introduction of specific interfacial area as a macroscopic transport parameter. The relationship between the specific interfacial area and the local saturation will be obtained from the PNM simulations. The behavior of this parameter in this limiting regime of immobile liquid phase will also be discussed.

The PNM simulations will generate the saturation profiles and the drying kinetics that will be used as reference data to analyze the results of the NLE CM. The macroscopic parameters that are needed to solve the NLE CM will be based on the results from PNM simulations. For this purpose, a method is developed that discretizes the 3D PNM computational domain into slices. The ground of this method stems from the

work by Attari Moghaddam et al. (2017), where the 3D PNM domain was discretized into slices or local averaging volumes. However, in this thesis, we will need to alter the discretization scheme, owing to the fact that we also need to perform the slice averaging of the partial vapor pressure (which is now also a state variable). Hence, contrary to the consideration in Attari Moghaddam et al. (2017) where two successive rows of pores were considered as part of a slice, our slice can only comprise of one row of pores (along with the interconnected throats). Also, the composition of the surface slice also varies from what was considered by Attari Moghaddam and coauthors, such that the surface slice now consists of only the surface pores and the vertical surface throats. The vapor pressure profiles and the total vapor flux obtained from the PNM are used to derive the effective vapor diffusivity. Similarly, the macroscopic specific interfacial area is computed by considering all the interfacial throats that are present in a slice.

In the next step, a two-equation CM that captures the NLE effect for a fully saturated porous medium will be developed. This model will be an extension of the NLE CM for the limiting case of immobile liquid phase such that the macroscopic capillary transport in the liquid phase will also be taken into account. The mass transport in the liquid phase will be described by Hagen-Poiseuille equation, and the liquid pressure field and liquid flux will be obtained from the PNM simulation of drying. The introduction of far-field capillary transport in the liquid phase implies that we will address the problem of mass transport at the surface by presenting the formulations of the individual boundary conditions for the vapor and liquid phase equations. The macroscopic transport parameters computed from PNM simulations using the aforementioned slice averaging method, will serve as a guide and reference for the input parameters needed to solve the two-equation CM.

In this thesis, we will analyze the CM of drying with dissolved solute transport, in terms of its ability to reproduce the solute concentration profiles obtained from PNM simulations. We will focus on the first drying period (also known as CRP), where the liquid at the surface remains connected with the liquid deep within the network. In the CRP, the classical CM of drying of capillary porous media considers the saturation

profiles to remain flat (no consideration of the edge effect) at all times during the drying process. We will investigate how this assumption affects the evolution of the solute concentration profiles.

With the help of PNM simulations, we will study the relationship of connectivity and distribution of liquid phase at the surface with the solute concentration in the surface throats. Also, we will statistically characterize the transport at the porous medium surface with the help of PNM Monte Carlo simulations. In doing so, we will analyze the probability of onset of crystallization based on an arbitrarily selected threshold value of saturation concentration. Additionally, we will also characterize the liquid phase structure by computing, with respect to network saturation, the expected probability that a saturated surface throat is an isolated single throat, a main cluster throat, or an isolated cluster throat.

Also, we will discuss the underlying reasons for the differences between the solute concentration profiles predicted by PNM simulations and CM solution. We will also discuss the averaged solute concentration profiles and the saturation profiles obtained from PNM simulations in comparison with the statistical analysis (that is performed with the help of Monte Carlo PNM simulations). We will elucidate the various pore scale mechanisms that control the solute concentration profiles and suggest a pathway for improvement in the CM of drying with dissolved solute transport.

1.4 Outline of contents

The organization of the next chapters of this thesis is as follows:

Chapter 2 consists of the description of the pore network model that is used in this thesis. The chapter explains the geometry of the pore network as well as the fundamentals of the pore network model algorithm. The chapter is divided into sections based on the distinction in the respective transport regimes, such as capillary dominated regime, viscous-capillary regime, and pore network model with dissolved solute transport. It is explained in detail how the respective mechanisms for fluid and solute transport are implemented in the pore network model algorithm.

Chapter 3 describes the formulation of NLE two-equation CM for the limiting case of immobile liquid phase. Then, the method used for the extraction of macroscopic parameters from PNM simulations is explained. The results of the PNM simulations (i.e. phase distributions, drying kinetics, and NLE effect) are presented. This is followed by a discussion of the macroscopic parameters (i.e. effective vapor diffusivity and specific interfacial area) which are obtained from PNM simulation results. Subsequently, the NLE CM solution is compared with the corresponding results of the PNM simulations. The NLE CM is also discussed in comparison with classical LE CM (front model). The drying regime that consists of immobile liquid phase used in this chapter is also compared with the receding front period (RFP). Finally, the methodology adapted in this chapter and the key findings are summarized.

In Chapter 4, the NLE two-equation CM for the full drying situation (drying of a fully saturated porous medium) is derived. The CM presented in this chapter considers the capillary liquid transport as well as the local evaporation and diffusion in the gas phase. This is followed by the comparison between the macroscopic parameters that are used for NLE CM solution and those computed from PNM simulations. The method for extraction of macroscopic parameters from PNM simulations is the same as that described in Chapter 3. The solution of the NLE CM, i.e. the phase distributions, drying kinetics and NLE effect, are compared to the corresponding PNM reference data. Then a sensitivity study of the macroscopic transport parameters is presented. This is followed by recapitulation of the key features and results obtained.

In Chapter 5, we assess and evaluate the widely used CM that is based on macroscopic advective-diffusive transport equation using PNM simulations. First, the formulation and underlying assumptions of this CM are described. Then, the solute concentration profiles and saturation profiles obtained from PNM simulations for different network saturation values are presented. In conjunction, the influence of pore scale heterogeneities on the evolution of solute concentration is clearly highlighted with the help of a graphical illustration obtained from a 2D PNM simulation. Then, the effective solute diffusivity is obtained from PNM simulations and subsequently used for the

CM solution. The CM solution, i.e. the resulting solute concentration profiles, are then evaluated in comparison with the corresponding PNM profiles. This is followed by a detailed analysis of the liquid and solute transport at the surface with the help of PNM simulations. Finally, the key aspects of the study are summarized and discussed.

In Chapter 6, we present a summary and overview of all chapters of this thesis. Finally, some possible pathways for future research related to this thesis are discussed.

Chapter 2

Pore network drying model

A part of this chapter is taken from "Ahmad, F., Rahimi, A., Tsotsas, E., Prat, M., Kharaghani, A.: From micro-scale to macro-scale modeling of solute transport in drying capillary porous media. Int. J. Heat Mass Transf. 165, 120722 (2021)". Another part is taken from "Ahmad, F., Talbi, M., Prat, M., Tsotsas, E., Kharaghani, A.: Non-local equilibrium continuum modeling of partially saturated drying porous media: Comparison with pore network simulations. Chem. Eng. Sci. 228, 115957 (2020)".

Pore network modeling is a discrete mesoscale approach where the pore scape is conceptualized by a network of narrow channels or throats that are interconnected through pores (see Fig. 2.1). The pore network model used in this thesis consists of volume-less pore nodes that act only as computational points. For detail on the pore network models with pore volume, see Lu et al. (2020) and references therein. In this thesis, the pore network model is based on a regularly structured 3D cubic lattice geometry, based on the work in Metzger et al. (2007), where the throats are cylindrical in shape. The throat length, i.e. the distance between two adjacent pores, is uniform and called the lattice spacing. The radii of the cylindrical throats follow a normal distribution which is based on mean radius and standard deviation. The lateral edges are connected to each other (periodic boundary condition), whereas the bottom side of the network is impermeable. The network of pore nodes extends outside of the pore network domain through the top edge into the discretized boundary layer. External

mass transport occurs through this diffusive boundary layer from the evaporating meniscus throats at ambient conditions.

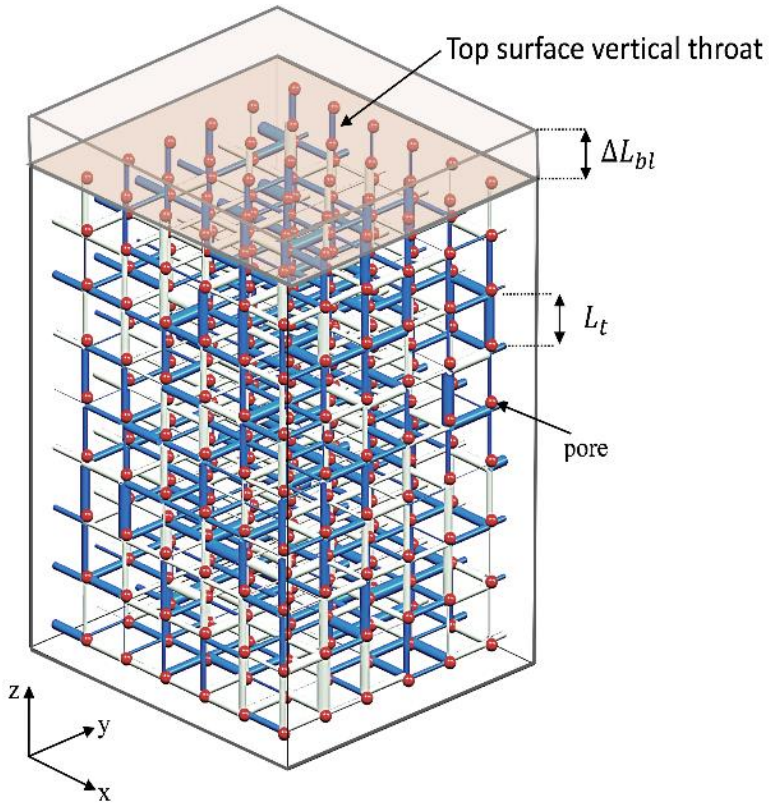

Fig 2.1: A sample three-dimensional pore network illustration with evaporative surface on top and a gas diffusion boundary layer of thickness ΔL_{bl} (the pore nodes in the boundary layer are not shown here). The throats filled with liquid are represented in blue, the gas-filled throats in gray and all pores in red color.

2.1 Drying algorithm in absence of viscous effect

Throughout the drying process, we keep track of the structure of the liquid phase, i.e. the state of its connectivity, in terms of the total number of liquid clusters, and isolated liquid throats are always accounted for. A liquid cluster is defined as a set of liquid throats interconnected by liquid pores. The information about the connectivity of the pores and throats is stored in the form of matrices. Each pore and throat in the inside of the network and in the boundary layer is indexed. The matrix that stores the information about the neighbor throats of each respective throat is referred to as tnt. Similarly, the information about the neighbor pores of each respective pore is stored

in a matrix referred to as pnp. The information about the neighbor throats of each pore and vice-versa is stored in pnt and tnp, respectively. These matrices used in conjunction can provide the index numbers of all the neighbors of the throats and pores inside the network and in the boundary layer. For more detail on the construction of these matrices, see Metzger et al. (2007). Using these matrices together with the information about the degree of saturation of the throats and pores, the state of the liquid phase connectivity, i.e. the individual liquid clusters and single throats, can be identified.

In the beginning of the drying process, evaporation occurs in the throats where the liquid phase forms an interface with the gas phase i.e., the throats at the surface that are exposed to the boundary layer. The interfacial throats are also referred to as meniscus throats. In each liquid cluster, the interfacial throat with the lowest capillary threshold is identified. The capillary threshold pressure P_c is calculated by the Young-Laplace equation as

$$P_c = \frac{2\gamma cos\theta}{r_t}, \tag{2.1}$$

where γ is the surface tension, θ the wetting angle and r_t the throat radius. In each liquid cluster, the throat with the lowest capillary pressure threshold is the throat with the highest potential to be invaded by the gas phase. See Fig. 2.2 for a simple illustration of the capillary pumping phenomenon. In other words, for each liquid cluster, the throat with the highest liquid pressure

$$P_l = P_g - P_c, \tag{2.2}$$

where P_g is the gas pressure, will be invaded by the gas phase. For the computation of evaporation rate from meniscus throats, we need the vapor pressure at each pore inside the network and in the boundary layer. The vapor transport is based on Stefan's flow, which for a throat k between the nodes i and j is expressed as

$$J_{v,k} = \pi r_t^2 \frac{\tilde{M}_v}{\tilde{R}\, T\, L_t} P_{atm} D_{va} ln\left(\frac{P_{v,i} - P_{atm}}{P_{v,j} - P_{atm}}\right), \tag{2.3}$$

where L_t, $\tilde{M}_v$, $\tilde{R}$, T, D_{va} and P_v denote length of the throat, molar mass of vapor, universal gas constant, temperature, air-vapor binary diffusion coefficient and vapor pressure, respectively. For more details on Stefan's flow, see Irawan (2006). At each pore node, mass balance for vapor flux is applied, enabling us to obtain a system of equations, which is then numerically solved to obtain the vapor pressure field. This means that we obtain values of partial vapor pressure at each pore node present inside and outside (boundary layer) the network. The pores that lie next to a partially or fully saturated throat are considered to have saturation vapor pressure, whereas the pores at the top of the boundary layer are considered to have zero vapor pressure. These serve as boundary conditions for the numerical solution of the vapor pressure field.

The discretization of the drying process is associated with the time for emptying of one meniscus throat, during which the vapor flow is assumed to be quasi-steady. For each cluster, the total evaporation rate from all the meniscus throats (computed from Eq. (2.3)) is assigned to the meniscus throat with the lowest capillary threshold for the respective cluster. Then, for each cluster, the time for emptying of all these meniscus throats is computed, the lowest among which is assigned as the time step. The phase distribution is updated, i.e. the saturation of the emptying throat is set to zero. For the next time step, the vapor pressure field is calculated based on the updated boundary conditions.

As the drying process goes on, the liquid clusters shrink and split into isolated menisci. The calculation of vapor transport is considered independently for each cluster. To this end, it is essential to label the liquid clusters. This is achieved by employing a variant of the Hoshen-Kopelman algorithm (Metzger et al., 2006). The labeling algorithm is used to relabel the liquid clusters at each time step. The drying process goes on until the liquid in the network has been entirely evaporated.

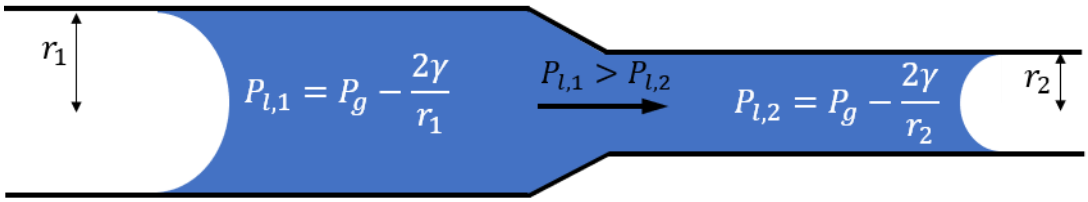

Fig. 2.2: An illustration of capillary transport of liquid phase as a result of variation in capillary pressures across the two sections of a tube. The liquid phase is shown in blue and the gas phase in white.

2.2 Drying algorithm in presence of viscous effect

The presence of viscosity requires some modifications in the drying algorithm presented in Sec. 2.1. Due to the viscous resistance, the water from the cluster meniscus with the lowest capillary pressure threshold may not be pumped to the evaporating meniscus throats of the cluster (see Fig. 2.3). As a result, other menisci may also empty as the rate of evaporation from the menisci could overcome the insufficient compensation of water through capillary pumping. The challenge is to identify the moving menisci during each time step. For this purpose, it is necessary to compute the liquid pressure field inside each cluster.

Firstly, for each cluster, the menisci with the lowest capillary threshold as well as the partially saturated ones are considered as moving, whereas the rest of menisci are considered to be stationary. Then stationary menisci are simply the ones whose mass loss from evaporation is fully compensated by the capillary pumping. However, the moving menisci have two categories: the ones that are emptying or receding and the ones that are refilling. The situation of a refilling meniscus can simply occur when, e.g., after a time step a newly formed meniscus within the considered cluster happens to be sufficiently larger, such that its liquid pressure is enough to compensate for the viscous forces that caused a meniscus to recede in the previous time step. As a result of this, a receding meniscus throat may turn into a refilling throat. However, the state of the moving meniscus does not impact the calculation of the liquid pressure field.

Note that the refilling only occurs in the partially saturated throats and the liquid cannot migrate into fully dried throats.

The fact, whether a meniscus is moving or stationary, determines the boundary condition for the calculation of liquid pressure field. For the stationary menisci, the evaporation rate associated with the individual meniscus directly provides the information about the incoming liquid flow rate, whereas for the moving menisci, the liquid pressure at the interface computed from Eq. (2.2) is assigned as the boundary condition. Based on the known boundary conditions for the stationary and moving menisci, the liquid pressure field is obtained by applying liquid mass balance at each pore. The liquid flow rate $J_{l,k}$ through a throat k that neighbors the pores i and j is computed based on the Hagen-Poiseuille equation as

$$J_{l,k} = \frac{\pi r_t^4 \rho_l}{8\mu_l L_t}\left(P_{l,i} - P_{l,j}\right), \tag{2.4}$$

where μ_l is the liquid viscosity. Due to the presence of viscous resistance to the liquid flow, the initially assumed states of the liquid throats have to be examined and, if necessary, modified through a number of iterative steps. Firstly, for all stationary throats, the discrepancy between incoming liquid flow and the outflowing liquid (mass loss through evaporation) is computed. Then the status of the stationary meniscus with largest negative discrepancy is updated to moving (emptying), as having a negative discrepancy means that the incoming liquid flow is not sufficient to compensate for the liquid outflow. Then, based on the updated boundary conditions, the liquid pressure field is computed again and the status of the meniscus with largest discrepancy is changed again to moving. Based on the updated boundary conditions, the liquid pressure field is computed repeatedly in a loop until there are no more stationary throats with negative discrepancy. The only difference between the non-viscous and the viscous drying algorithm is linked to the correct identification of the status of meniscus throats. The rest of the algorithm is the same as described in Sec. 2.1.

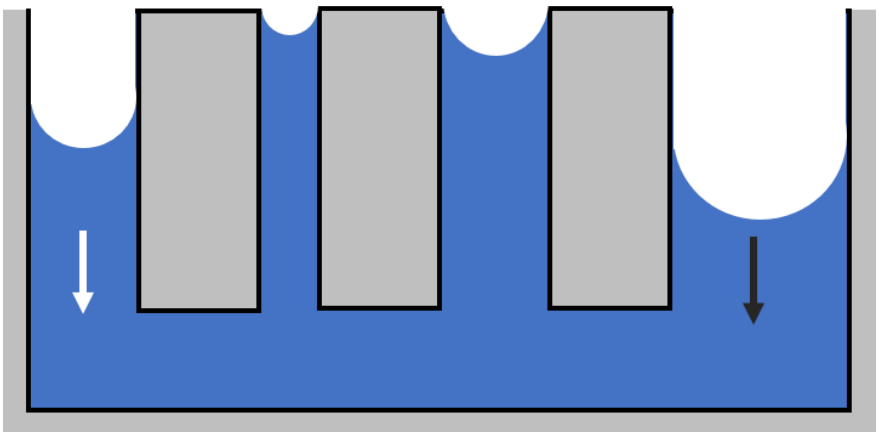

Fig. 2.3: An illustration of capillary liquid transport in presence of viscous resistance to the liquid flow. The liquid phase is shown in blue and the gas phase in white. Evaporation is from the top side of the container. The arrow in black shows the direction of liquid flow from the biggest throat to all other throats. The arrow in white shows the movement of meniscus which is receding as a result of insufficient liquid compensation due to viscous forces.

2.3 Drying algorithm with dissolved solute transport

The advective-diffusive transport of the dissolved solute in the liquid phase is modeled at the pore scale within the throats. Figure 2.4 illustrates a simple case of advective-diffusive solute transport inside a drying solution and the resulting variation in concentration field. The PNM with dissolved solute transport used in this thesis is set for a 3D regular cubic network, based on the work presented by Rahimi (2019). In the PNM algorithm that does not account for solute transport, the drying process is discretized according to time for emptying of one meniscus throat, here referred to as global time step. During each discretized time step, the boundary conditions for vapor pressure field are assumed to be stationary. However, in the PNM that accounts for solute transport, the time step is discretized according to the stability criterion of the advection-diffusion equation with an explicit solution scheme

(Licsandru et al., 2019). The explicit form of the equation governing the solute transport between nodes *i* and *j* for a throat *k* is given as

$$\frac{dC_k}{\partial t} = U\frac{C_i - C_k}{L_t} + \frac{2D_s}{L_t}\left(\frac{C_j - 2C_k - C_i}{L_t}\right), \tag{2.5}$$

where C_k denotes the solute concentration of throat *k*, C_i and C_j the concentration at the nodes *i* and *j*. The concentration at the nodes is computed assuming perfect mixing of the liquid at each node. In other words, we apply the mass balance at each node considering the total advective and diffusive solute flow between a pore and its neighboring throats. For the simple case of 2D pore network, the concentration at node *i* is expressed as

$$C_i = \frac{\sum_{k=1}^{2} u_k A_k C_k + \sum_{k=1}^{4} 2D_s \frac{A_k C_k}{L_k}}{\sum_{k=3}^{4} u_k A_k + \sum_{k=1}^{4} 2D_s \frac{A_k}{L_k}}, \tag{2.6}$$

where *k* indicates the neighbor throats of the pore *i*. Throats 1 and 2 provide liquid flow to pore *i*, whereas throats 3 and 4 transport liquid away from pore *i*. Solute transport calculations are carried out within these time increments, assuming constant capillary flow rates until the global time step has elapsed. The time steps that satisfy the stability criteria for advection and diffusion are computed as

$$\Delta t_{adv} \leq \frac{L_k}{U} \tag{2.7}$$

and

$$\Delta t_{diff} \leq \frac{1}{2}\frac{\left(\frac{L_k}{2}\right)^2}{D_s}, \tag{2.8}$$

respectively. The minimum of Δt_{adv} and Δt_{diff} is considered as the salt time step. An adaptive sub-discretization algorithm, based on the local Péclet number, is utilized for the throats to improve numerical accuracy of the model while keeping the computational time in check. If the Péclet number in a throat is above unity, it is discretized into sub-elements until the Péclet number in each sub-element is below unity.

When the solute concentration in a throat reaches a threshold referred to as the critical concentration (C_{cr}), crystallization occurs and the solution in the vicinity of the crystals rapidly becomes close to the solubility, also referred to as the saturation concentration (C_{sat}), see, for example, Naillon et al. (2018), Patankar (1980). As a result, the solute concentration value does not supersede the threshold value of C_{sat} after the time step has elapsed. As mentioned earlier, since the focus in this study is on the solute distribution prior to crystallization, no particular threshold value for crystallization is considered. The concentration can thus increase as dictated only by the competition between advection and back-diffusion and the changes in liquid saturation. Also, for simplicity, we neglect the influence of the solute concentration on the properties of the fluid.

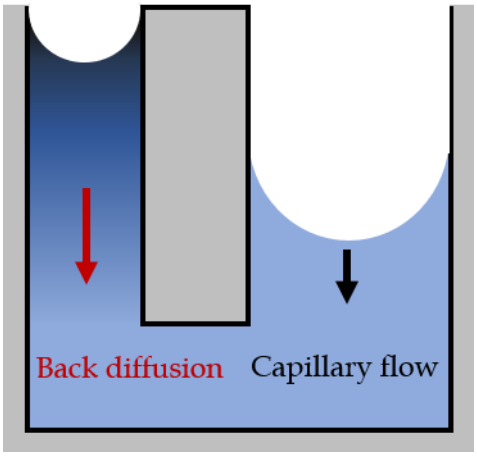

Fig. 2.4: An illustration of advective transport of dissolved solute through capillary liquid flow and back diffusion as a result of solute concentration built up in the solvent. Evaporation is from the top side of the container.

Chapter 3

NLE continuum modeling: The limiting case of immobile liquid phase

This chapter is partly taken from "Ahmad, F., Talbi, M., Prat, M., Tsotsas, E., Kharaghani, A.: Non-local equilibrium continuum modeling of partially saturated drying porous media: Comparison with pore network simulations. Chem. Eng. Sci. 228, 115957 (2020)".

The modeling of drying porous media has been a subject of research for decades. Heat and mass transfer during the two stages of drying is more commonly described using the concept of continuum modeling (CM). A presentation of the most popular continuum model in this context can be found in Whitaker (1977), where heat and mass transfer during evaporation in a porous medium was extensively modeled in the framework of the volume averaging method. This widely used CM combines the equations for the liquid flow and for the vapor flow into a single equation under the assumption of local equilibrium (LE) between the vapor and the liquid phases. However, this assumption has been questioned (Bénet and Jouanna, 1982). It was argued that the equilibrium characteristic time $t_{eq} \approx L^2/D_v$, where L is a characteristic length of the porous medium and D_v is the vapor diffusivity, was too long for the local equilibrium condition to be satisfied during drying. This leads to a different class of models where the liquid flow equation and the vapor flow equation are not merged into a single equation and both contain a non-equilibrium phase change term. One can refer, for instance, to Li et al. (2019) for a presentation of the NLE CM together with

the more classical LE CM model. The NLE effect is considered to be especially significant in hygroscopic materials (see, e.g., Bénet and Jouanna 1982; Bénet et al., 2009; Ouedraogo et al., 2013), where vapor pressure is influenced by the degree of saturation of the material. However, in capillary porous materials, in which adsorption phenomena are negligible and the vapor pressure is influenced only by temperature, the NLE effect has been treated as a seemingly less important issue. However, the pore network model (PNM) simulations reported in Attari Moghaddam et al. (2017) clearly indicate that the NLE effect is also present during the drying of capillary porous media. As a consequence of the NLE effect, it was shown that the saturation profiles computed from the pore network simulations could not be simulated with the classical LE model using a single set of macroscopic parameters (Vorhauer et al., 2010). Also, the drying kinetics could not be simulated over the complete drying process using the classical one-equation CM model (Attari Moghaddam et al., 2017b). The conclusion was therefore that a NLE CM formulation should be considered not only for hygroscopic materials as suggested by Bénet and co-workers but also for capillary porous media. The present work is a step in this direction.

The methodology used in this work is the same as in Attari Moghaddam et al. (2017). PNM simulations are used for generating reference data, such as saturation profiles and drying kinetics. Then, the NLE CM is tested against the volume averaged PNM data. Compared to Attari Moghaddam et al. (2017), the new feature is that a NLE continuum model is considered. Hints on the formulation of the NLE phase change term in this model are obtained using the volume averaging method. Also, as in previous work on the NLE effect, i.e. Ouedraogo et al. (2013), we focus on the conditions of low initial saturation. In our case, this corresponds to a situation where the liquid phase is formed by a set of disconnected small clusters. This implies that, in the context of PNM, while capillary pumping is considered, we can neglect the influence of viscosity in the liquid phase.

These liquid clusters are minimally sized and are located randomly inside the network (see Fig. 3.1). We follow an iterative process to ensure that each cluster consists of just

one saturated node. In 3D PNM, this means that each cluster may consist of a maximum of six saturated throats that are connected through a saturated node. To generate this disconnected liquid phase distribution, we choose an initial fraction of nodes that would be assigned a saturation of one. Then, the chosen number of nodes are distributed randomly inside the network and assigned a saturation value of one. Next, the neighbor throats that are connected to these randomly located nodes are also assigned a saturation value of one. Following this, we begin a node by node scan of the whole network and ensure that each node has no other saturated node connected to it. For example, if a scanned node *i* has a neighbor node *i+1* that is saturated, then we assign a saturation value of zero to one of the neighbor throats of node *i+1*. This in turn makes the node *i+1* unsaturated. This is because a node becomes unsaturated if at least one of its neighbor throats becomes unsaturated. This process is repeated until all clusters are minimally sized, i.e. consist of one saturated node.

This enables us to concentrate on a situation where the vapor transport is a dominant mechanism. Similarly to Attari Moghaddam et al. (2017), evaporation controls the mass transfer and the temperature variation is negligible.

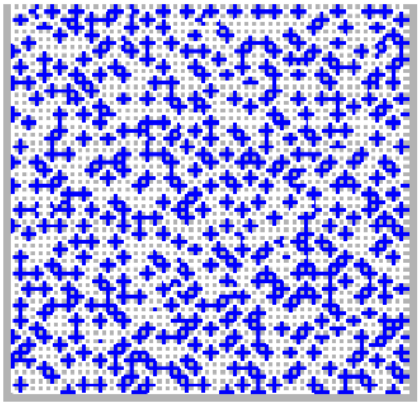

Fig. 3.1: A 2D representation of 50×50 pore network in which the liquid phase (shown in blue) is distributed as isolated clusters. The gas and solid phases are represented in white and grey, respectively. Note that for our discrete simulations 3D pore networks are used.

3.1 Description of the NLE CM for the limiting case of immobile liquid phase

As discussed in several previous works, i.e. Li et al. (2019), Ouedraogo et al. (2013) and references therein, the NLE continuum model can be expressed as a system of two coupled equations, one for the liquid flow and one for the vapor flow. When the liquid phase is formed by small disconnected clusters, there is no macroscopic flow in the liquid phase and the model can be simplified. Under these circumstances, it can be expressed as

$$\varepsilon \frac{\partial (1-S) P_v}{\partial t} = \nabla . \left(\varepsilon (1-S) D_{eff} \nabla P_v \right) + \frac{\tilde{R} T}{\tilde{M}_v} \dot{m} \tag{3.1}$$

for the vapor flow and

$$\varepsilon \rho_l \frac{\partial S}{\partial t} = -\dot{m} \tag{3.2}$$

for the liquid phase (considered to be immobile). In Eqs. (3.1) and (3.2), ε, t, D_{eff}, S, ρ_l and P_v denote the porosity, time, macroscopic vapor diffusion coefficient, liquid saturation, water density and water vapor partial pressure, respectively. $\tilde{M}_v$, $\tilde{R}$ and T represent the molar mass of water, universal gas constant, and temperature; $\dot{m}$ is the phase change rate between the liquid and vapor phases. The latter is also referred to as the NLE phase change term. Different formulations are proposed for $\dot{m}$ in the literature. In the works of Bénet and co-workers, i.e. Ouedraogo et al. (2013) and references therein, $\dot{m} = \beta \frac{\tilde{R} T}{\tilde{M}_v} ln \left(\frac{P_v}{P_{v,eq}} \right)$, where $P_{v,eq}$ is the equilibrium vapor pressure and β is a phenomenological coefficient which notably depends on the porous medium microstructure. In Li et al. (2019), this term was expressed as $\dot{m} = b\varepsilon(S - S_{res}) \frac{\tilde{R} T}{\tilde{M}_v} \left(P_{v,eq} - P_v \right)$, where b is a coefficient and S_{res} is the residual water content. The same expression was used in Pujol et al. (2011) with S_{res} = 0. In order to clarify the formulation of $\dot{m}$ a derivation using the volume averaging method (Whitaker, 2013) is presented in the following, taking advantage of the mathematical analogy with the problem of diffusion with heterogeneous reaction presented in Whitaker (2013).

Starting point is the pore scale description of vapor transport in the domain occupied by the gas phase in the porous medium

$$\frac{\partial \rho_v}{\partial t} = \nabla.(D_{va}\nabla\rho_v), \tag{3.3}$$

where ρ_v and D_{va} denote the vapor density and air-vapor binary diffusion coefficient, respectively. The boundary condition at the solid-gas interface can be expressed as

$$-D_{va}\nabla\rho_v.\mathbf{n}_{gs} = 0, \tag{3.4}$$

where $\mathbf{n}_{gs}$ is the unit vector in the direction perpendicular to the solid-gas interface. At the liquid-gas interface (A_{gl}), we make use of the Hertz-Knudsen-Schrage (HKS) equation (Schrage, 1953) and express the boundary condition as

$$-D_{va}\nabla\rho_v.\mathbf{n}_{gl} = -\frac{2\sigma}{2-\sigma}\sqrt{\frac{\widetilde{M}_v}{2\pi k_B}}\left(\frac{P_{v,sat}}{\sqrt{T_l}} - \frac{P_v}{\sqrt{T_g}}\right), \tag{3.5}$$

where $\mathbf{n}_{gl}$, $\widetilde{M}_v$, k_B, σ, T_g, T_l denote the unit normal vector perpendicular to the gas-liquid interface, molar mass of water vapor, Boltzmann constant, accommodation coefficient, gas temperature and liquid surface temperature, respectively. Assuming $T_l = T_g$ and using T to represent the temperature, Eq. (3.5) can be expressed as

$$-D_{va}\nabla\rho_v.\mathbf{n}_{gl} = -\frac{2\sigma}{2-\sigma}\sqrt{\frac{\widetilde{M}_v}{2\pi k_B T}}\left(P_{v,sat} - P_v\right). \tag{3.6}$$

Using ideal gas law, we can express Eq. (3.3) in terms of P_v as

$$\frac{\partial P_v}{\partial t} = \nabla.(D_{va}\nabla P_v). \tag{3.7}$$

Similarly expressing Eqs. (3.4) and (3.6) in terms of P_v

$$-D_{va}\nabla P_v.\mathbf{n}_{gs} = 0, \tag{3.8}$$

$$-D_{va}\nabla P_v.\mathbf{n}_{gl} = -k\left(P_{v,sat} - P_v\right), \tag{3.9}$$

where

$$k = \frac{2\sigma}{2-\sigma}\sqrt{\frac{T\tilde{R}^2}{2\pi k_B \widetilde{M}_v}}. \tag{3.10}$$

Here, with the intention to re-formulate the vapor transport equations at the pore-scale we define a new variable P_v^* as

$$P_v^* = P_{v,sat} - P_v. \tag{3.11}$$

Using Eq. (3.9) we re-formulate the problem of vapor transport at the pore-scale in terms of P_v^* and express Eq. (3.7) as

$$\frac{\partial P_v^*}{\partial t} = \nabla.(D_{va}\nabla P_v^*). \tag{3.12}$$

Similarly, we can express Eqs. (3.8) and (3.9) as

$$-D_{va}\nabla P_v^*.\mathbf{n}_{gs} = 0, \tag{3.13}$$

$$-D_{va}\nabla P_v^*.\mathbf{n}_{gl} = kP_v^*. \tag{3.14}$$

Invoking the advantage of the analogy between the problem of diffusion and heterogeneous reaction presented in Whitaker (2013) and using the volume averaging method (Whitaker, 2013), we upscale the problem leading to the volume transport macroscopic equation

$$\varepsilon(1-S)\frac{\partial P_v^*}{\partial t} = \nabla.\left(\varepsilon(1-S)D_{eff}\,\nabla P_v^*\right) + \nabla.(\mathbf{u}P_v^*) - a_{gl}kP_v^*, \tag{3.15}$$

where we use the same notation for the volume averaged partial pressure as in the pore scale problem. In Eq. (3.15), a_{gl} is the liquid-gas interfacial area per unit volume

$$a_{gl} = \frac{A_{gl}}{V}. \tag{3.16}$$

It is argued in Whitaker (2013) that the term $\nabla.(\boldsymbol{u}P_v^*)$ in Eq. (3.15) is negligible. Thus, Eq. (3.15) can be expressed as

$$\varepsilon\frac{\partial(1-S)P_v}{\partial t} = \nabla.\left(\varepsilon(1-S)D_{eff}\,\nabla P_v\right) + a_{gl}k(P_{sat} - P_v). \tag{3.17}$$

It is important to note that the effective diffusivity D_{eff} is computed assuming zero flux on the liquid-gas interface. Also, note that the HKS theory was introduced for convenience in order to start from a formulation analogous to the one considered in

Whitaker (2013). It is to be noted that the HKS theory is not included in the PNM drying algorithm.

For the characterization of liquid phase, we begin with the pore-scale expression

$$\frac{\partial \rho_l}{\partial t} = \nabla.(\rho_l \mathbf{v}). \tag{3.18}$$

Applying the volume averaging method leads to

$$\varepsilon \rho_l \frac{\partial S}{\partial t} = \nabla.\langle \rho_l \mathbf{v} \rangle + \frac{1}{V}\int_{A_{lg}} \rho_l(\mathbf{v}-\mathbf{w}).\mathbf{n}_{lg} dA, \tag{3.19}$$

where $\mathbf{v}$ is the liquid phase mass average velocity and $\mathbf{w}$ is the velocity of liquid-gas interface. At a meniscus, we have

$$\rho_l(\mathbf{v}-\mathbf{w}).\mathbf{n}_{lg} = \rho_v(\mathbf{v_v}-\mathbf{w}).\mathbf{n}_{lg}, \tag{3.20}$$

where $\mathbf{v_v}$ is the velocity of the water vapor and

$$\rho_v(\mathbf{v_v}-\mathbf{w}).\mathbf{n}_{lg} = -\frac{\widetilde{M}_v}{\tilde{R}T} D_{va} \nabla P_v.\mathbf{n}_{gl}. \tag{3.21}$$

Assuming isolated liquid clusters and considering Eq. (3.9), the convective liquid flow can be neglected, enabling us to express Eq. (3.19) as

$$\varepsilon \rho_l \frac{\partial S}{\partial t} = -\frac{A_{gl}}{V} k \frac{\widetilde{M}_v}{\tilde{R}T}\left(P_{v,sat} - P_v\right). \tag{3.22}$$

Taking into account Eq. (3.16), we express Eq. (3.22) as

$$\varepsilon \rho_l \frac{\partial S}{\partial t} = -a_{gl} k \frac{\widetilde{M}_v}{\tilde{R}T}\left(P_{v,sat} - P_v\right). \tag{3.23}$$

The final form of the liquid and vapor phase equations of the two-equation CM for the limiting case of immobile liquid phase can thus be expressed as

$$\varepsilon \frac{\partial (1-S)P_v}{\partial t} = \nabla.\left(\varepsilon(1-S) D_{eff}\, \nabla P_v\right) + a_{gl} k\left(P_{v,sat} - P_v\right), \tag{3.24}$$

$$\varepsilon \rho_l \frac{\partial S}{\partial t} = -a_{gl} k \frac{\widetilde{M}_v}{\tilde{R}T} \left(P_{v,sat} - P_v\right). \tag{3.25}$$

Therefore, the NLE phase change term can be expressed as

$$\dot{m} = -a_{gl} k \frac{\widetilde{M}_v}{\tilde{R}T} \left(P_{v,eq} - P_v\right), \tag{3.26}$$

where a_{gl} is the specific interfacial area between liquid and vapor phases and k is a coefficient. In our case $P_{v,eq}$ is equivalent to $P_{v,sat}$. $P_{v,sat}$ is the saturation water vapor partial pressure since adsorption phenomena are not considered in the PNM simulations on the ground that they are negligible in capillary porous media. Another noticeable outcome from the derivation presented above is that the effective coefficient D_{eff} can be computed as if the liquid was simply acting as a solid obstacle to vapor diffusion. In other terms, and contrary to the consideration on vapor diffusion in drying by Philip and De Vries (1957), the derivation does not suggest that an enhancement effect should be considered in the determination of D_{eff} as a result of phase change within the representative elementary volume. One can refer, for instance, to Plumb et al. (1999) for more details on the vapor diffusion enhancement factor.

To simulate the drying problem with the NLE CM (Eqs. (3.24) and (3.25)), three macroscopic coefficients must be determined, namely a_{gl}, D_{eff} and k, noting that a_{gl} and D_{eff} are functions of saturation. The method to determine these coefficients is presented in Sec. 3.2. Then, initial and boundary conditions must be specified. The pore network is initially saturated with liquid and supposed to be at equilibrium. Thus $P_v = P_{v,sat}$ throughout the computational domain at $t = 0$. The initial liquid phase saturation is computed by volume averaging the initial liquid water distribution in the pore network.

The two-equation CM is solved in 1D by discretizing the computational domain by using finite volume method. At the bottom of the domain, a zero-flux boundary condition is applied, whereas at the evaporative surface the specific evaporation rate is computed by the following equation:

$$\varepsilon(1-S)\frac{\widetilde{M}_v}{\tilde{R}\,T}D_{eff}\nabla P_v.\mathbf{n} = -\frac{\widetilde{M}_v}{\tilde{R}\,T}D_{va}\frac{P_{v,surf}-P_{v,\infty}}{L_{bl}}, \tag{3.27}$$

where D_{va}, L_{bl}, $\mathbf{n}$, $P_{v,surf}$ and $P_{v,\infty}$ denote the water vapor molecular diffusion coefficient, external boundary layer thickness, unit normal vector directed toward the external boundary layer, vapor pressure of the surface volume element and vapor pressure in the bulk air, respectively. The formulation of the boundary conditions at the evaporative surface is actually not that obvious with the two-equation NLE CM model since both liquid and vapor pores can be present at the surface. The question thus arises as to how the external evaporation flux should be split into a contribution from the evaporation of the surface liquid pores and a contribution from surface pores occupied by the gas phase. However, the consideration of an immobile liquid phase simplifies the modeling of the exchange at the evaporative surface, since no boundary condition is actually needed in conjunction with Eq. (3.2). For the CM solution, we require only the boundary condition for Eq. (3.1).

3.2 Extraction of macroscopic transport parameters from drying PNM simulations

Macroscopic parameters can be determined from dedicated PNM simulations (Øren et al., 1998; Blunt et al., 2001). Most of the literature in this regard pertains to the drainage process, and the focus is on relative and absolute permeabilities and capillary pressure curve. The use of PNM for drying porous media (Nowicki et al., 1992; Attari Moghaddam et al., 2017) has also been done along similar lines with the addition of computation of vapor diffusivity. This requires developing specific computations over a representative elementary volume (REV). In what follows, we proceed somewhat differently and apply a method inspired from the method used to determine the moisture transport coefficient from drying experimental results in previous works. Typically, in these experiments, transient saturation profiles were determined for a given set of conditions (e.g. Schoeber, 1976; Marchand and Kumaran, 1994; Pel et al., 1996; Gomez et al., 2007). Subsequently, these saturation profiles were used to compute moisture transport coefficients. In our case, the saturation profiles are

obtained from volume averaging of the appropriate PNM drying simulation data and we also use the volume averaged vapor pressure profiles.

The macroscopic parameters determined from PNM drying simulations are effective vapor diffusivity and specific interfacial area. As mass transport is in the gas phase only (immobile liquid phase), we do not compute liquid diffusivity. The dependency of macroscopic effective vapor diffusivity and specific interfacial area on local saturation is determined using the data obtained from PNM drying simulations. For our PNM, the computation is carried out on two levels: on the scale of pore throats, we compute the liquid saturation, and on the scale of volume-less pore nodes, we compute partial vapor pressure.

The data at the pore scale is transformed into macroscopic scale by dividing the three-dimensional pore network into horizontal slices of thickness Δz – an exemplary 3D pore network is illustrated in Fig. 3.2. Here one slice is the macroscopic averaging volume over which local saturation and vapor pressure are computed. As shown in Fig. 3.2, we characterize a slice such that it consists of pore-nodes which lie on the side of top bounding plane of the slice, horizontal throats directly connected to these pore-nodes and the neighbor vertical throats that are directed towards the bottom. The local saturation of the slice is computed by calculating the ratio of liquid volume in the throats contained in the slice to the total volume of throats in the slice. For the computation of local vapor pressure in the slice, we compute the arithmetic mean of the vapor pressures of the pores contained inside the slice. The characterization of the surface slice is different from other slices due to the fact that in PNM the pore-nodes in surface plane do not have any directly connected horizontal throats.

The vapor flow rate through vertical throats in a slice is computed using the vapor pressure of pore nodes as follows

$$J_v = \pi r_t^2 \, \frac{\widetilde{M}_v}{\tilde{R}\, T\, L_t} P_{atm} D_{va} ln\left(\frac{P_{v,i} - P_{atm}}{P_{v,j} - P_{atm}}\right), \tag{3.28}$$

and summed up to give the total vapor flux passing through a slice. This total flux is then divided by the cross-section area of the plane (as illustrated in Fig. 3.2 by A_{plane}) to provide j_v which is then used to compute D_{eff} from the flux between two slices using

$$D_{eff} = -\frac{\tilde{R}\,T}{\tilde{M}_v}\frac{j_v}{\varepsilon(1-S)\,\frac{\partial P_v}{\partial z}}. \tag{3.29}$$

Apart from this, in order to neglect the local transport in liquid phase, the size of liquid clusters is kept small in a way that they do not span over a slice. Hence, interslice liquid transport is avoided by restricting the cluster size. Additionally, we compute the specific interfacial area a_{gl} by summing up cross-section area of interfacial throats belonging to a slice and divide it by the total macroscopic volume of that slice. It should be noted that the interfacial area is measured at the meniscus level and not at the pore-node, meaning that one gas pore can have several interfacial throats connected to it.

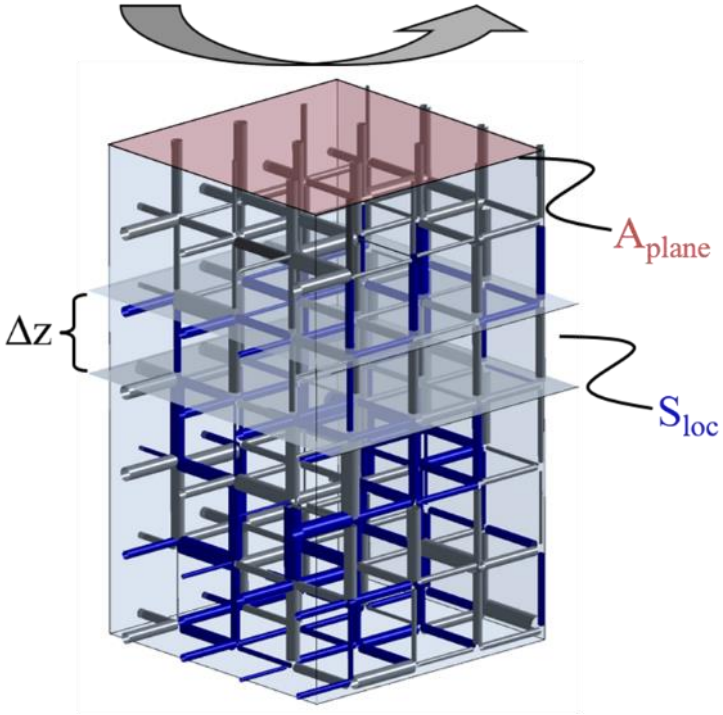

Fig. 3.2: A sample pore network illustration with evaporative surface on top and a slice (local averaging volume) cut perpendicular to z direction from the pore network consisting of one row of nodes (connected to top side of vertical throats) for computation of vapor pressure. The throats filled with liquid are represented in blue and gas-filled throats in gray. A_{plane} represents network cross-section area and Δz represents the thickness of slice. The computational nodes in the external boundary layer on top of the network are not visible here.

3.3 Simulation results

In this section, we present the macroscopic parameters computed from PNM simulations based on the method described in Sec. 3.2. Then, these parameters are used to solve the two-equation CM of drying and the consequent saturation profiles, vapor pressure profiles, evaporation rate, and non-local equilibrium effect are compared to the corresponding PNM simulation results.

3.3.1 Pore network drying simulations

The input parameters that specify the structure and physical conditions for PNM drying simulations are listed in Table 1. To minimize the influence of randomness in throat size distribution and initial liquid phase structure on the macroscopic parameters, we carried out 45 simulations, each with different realization of throat size distribution and initial liquid phase structure (location of liquid clusters). All the results shown in this section are averaged over these 45 simulations (unless stated otherwise). As the liquid phase is discontinuous and the size of clusters is very small, the viscosity of liquid phase becomes irrelevant. We operate in the capillary-dominated regime as far as the evolution of the liquid phase is concerned. Mass transport through the network is purely controlled by diffusion in the gas phase. To produce the initial liquid phase structure with discontinuous liquid phase, we can have an arbitrary amount of liquid in the network. We choose an arbitrary initial network saturation of 0.26 for the PNM drying simulations and the subsequent CM solution.

Structural property	**Unit**	**Value**	**Physical constant**	**Unit**	**Value**
Network size (nodes)	-	25×25×50	Temperature	K	293.15
Boundary layer discretization	-	25×25×4	Pressure	Pa	10^5
Mean throat radius	mm	0.25	Diffusion coefficient	m^2/s	$2.56x10^{-5}$
Standard deviation of throat radius	mm	0.025	Saturation vapor pressure	Pa	2339
Throat length	mm	1	Surface tension	N/m	0.07274
Network porosity	-	0.594			

Table 1: Structural and physical parameters for PNM simulations.

The evolution of overall network saturation S_{net} with time and the change in normalized total evaporation rate with respect to S_{net} are shown in Fig. 3.3. The evaporation rate drops sharply as the surface water evaporates, followed by a consistent decrease in evaporation rate.

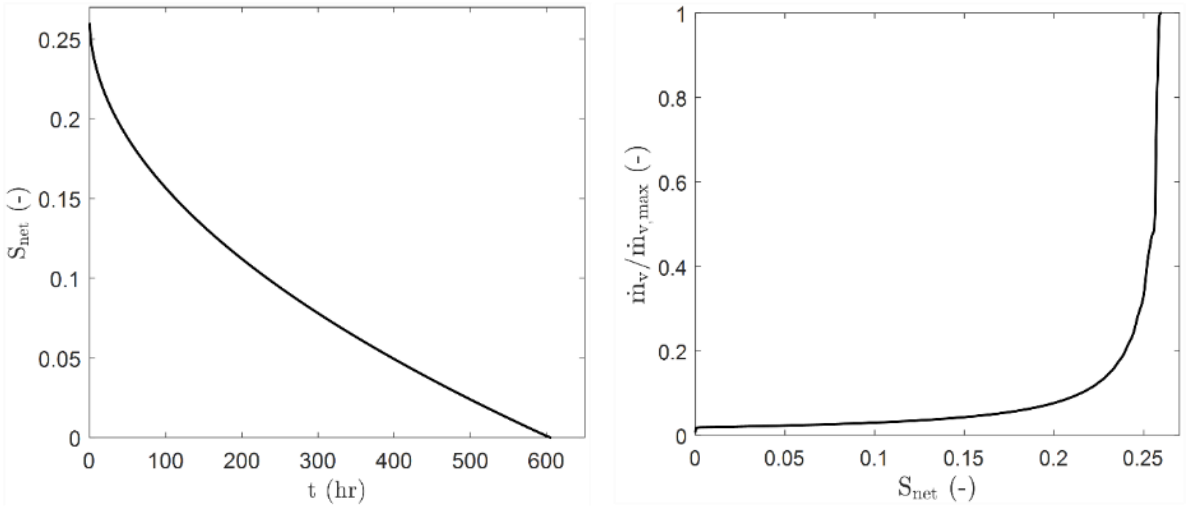

Fig. 3.3: Variation of network saturation S_{net} with drying time (left) and normalized evaporation rate with respect to S_{net} (right).

Compared to the classical drying kinetics for capillary porous media, no constant rate period (CRP) is observed. This behavior is in accordance with the initial condition imposed in our simulations for the liquid phase distribution. As illustrated in Fig. 3.4, the drying situation is characterized by a traveling drying front, where the saturation varies abruptly from the initial saturation to zero. The saturation plotted in Fig. 3.4 and denoted by S_{loc} corresponds to the saturation determined in each slice of the network (as defined in Sec. 3.2). Referring to the drying kinetics classical description in three periods (van Brakel, 1980), our case is close to the last period, referred to as the receding front period (RFP), where a dry zone develops into the porous medium from the surface (Pel et al., 1996). As will be discussed later, the dynamics of the drying front, i.e. how the position of the front scales with the elapsed time, is however different in our simulations.

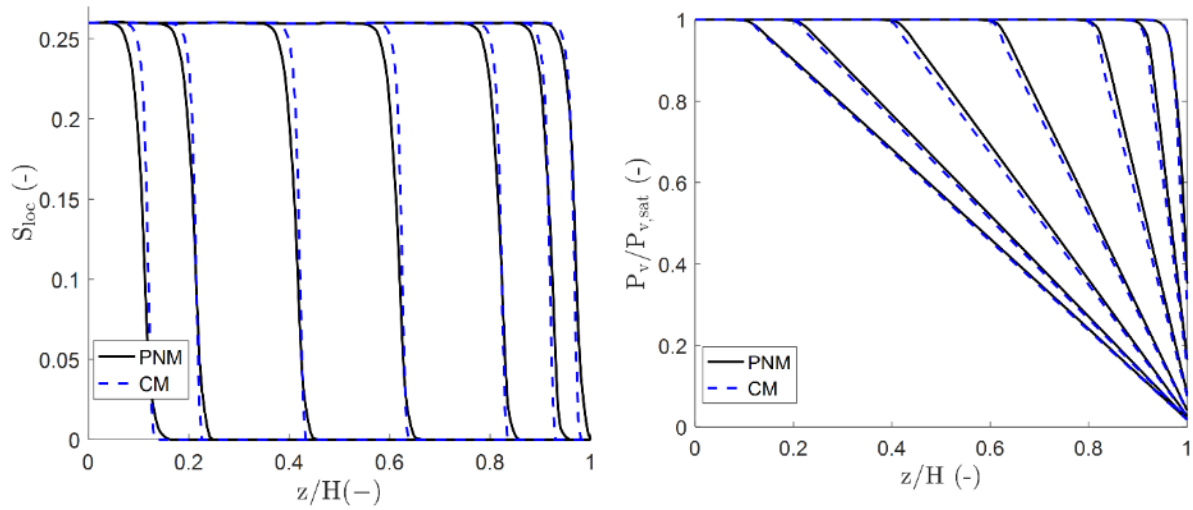

Fig. 3.4: Saturation profiles (left) and normalized vapor pressure profiles (right) obtained from two-equation CM (blue dashed lines) and PNM (black solid lines). CM results are plotted for times that correspond to S_{net} of 95, 90, 80, 60, 40, 20 and 10 % of $S_{net,ini}$ for PNM simulation results. The outer surface lies at z/H = 1 in both figures.

3.3.2 NLE effect

The ratio of P_v to $P_{v,sat}$ as a function of both local saturation and network saturation characterizing the non-local equilibrium is obtained from PNM simulations and illustrated in Fig. 3.4.

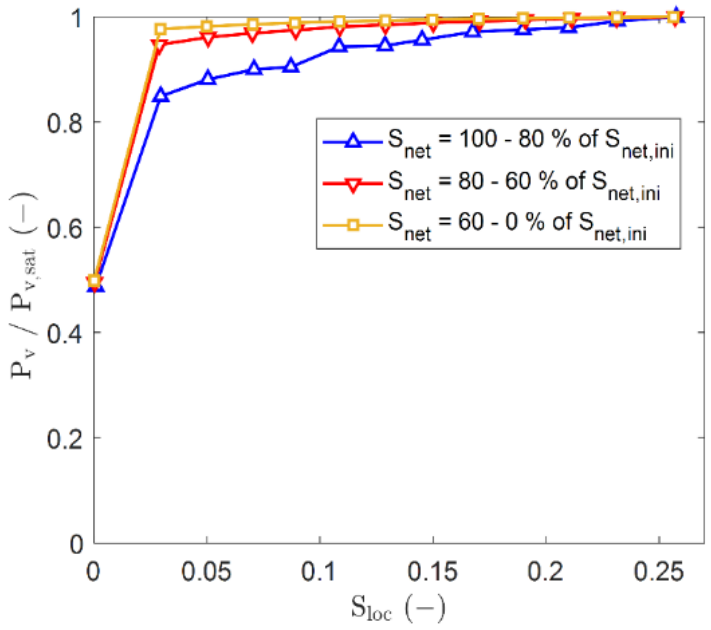

Fig. 3.5: Averaged value of NLE indicator as a function of local saturation (S_{loc}) for different intervals of network saturation (S_{net}).

Based on continuity of vapor flow, the closer a pore is to the boundary layer, the lower is the vapor pressure of the pore. Hence, when the drying front is on the surface, the vapor pores constituting the surface slice exhibit the lowest vapor pressure of any slice. As the drying front recedes into the network away from the boundary layer, the NLE effect decreases because the distance from the boundary layer increases. As shown in Fig. 3.5, the NLE effect increases abruptly, i.e. the ratio of P_v to $P_{v,sat}$ decreases significantly, for very low saturations (S_{loc} < 0.03 in Fig. 3.5); this corresponds to the drying front where the saturation varies sharply over a small distance (see the saturation profiles in Fig. 3.4).

3.3.3 Macroscopic water vapor diffusivity

Figure 3.6 shows the variation of the ratio of D_{eff} to D_{eff}^* with respect to local saturation obtained from PNM drying simulations. D_{eff}^* is D_{eff} (S_{loc}= 0), i.e. the effective vapor diffusivity for a completely dry network. The local saturation here is computed as an arithmetic mean of saturation of the two successive local averaging volumes between which the vapor transfer occurs. As expected the value of D_{eff} is highest when the vapor flux faces no resistance from the presence of liquid phase, i.e. when D_{eff} is equal to D_{eff}^*.

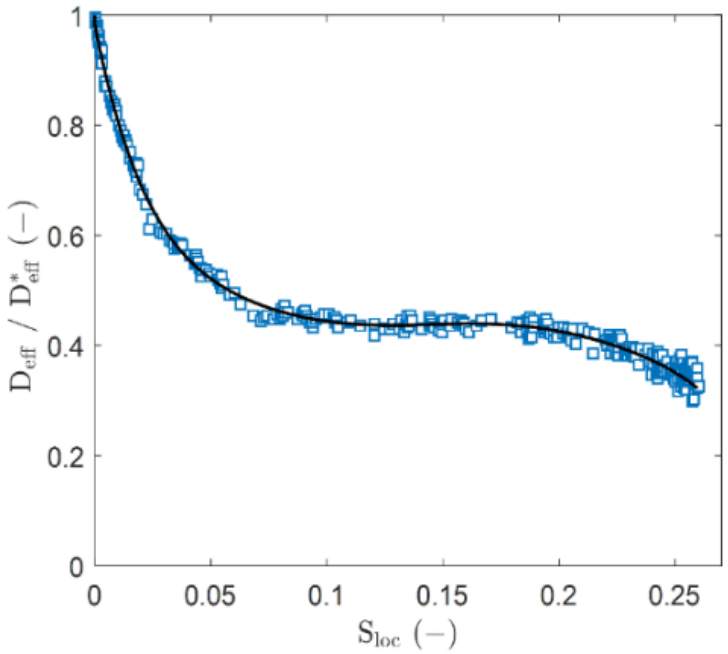

Fig. 3.6: Ratio of D_{eff} to D_{eff}^* with respect to averaged local saturation. The black solid line represents the fitted profile through the discrete data points shown by blue symbols.

We observe an initial increase in D_{eff} with decreasing S_{loc} followed by an intermediate period of approximately constant value and then a sharp increase in D_{eff} until zero local saturation has been reached. The plateau for the intermediate local saturation range has generally not been observed in previous works, i.e. Pel et al. (1996), in which the vapor diffusivity decreases continually with increasing saturation. The difference is that here we start from a different liquid phase distribution where the liquid phase is distributed in small isolated clusters. The results shown in Fig. 3.6 indicate that the tortuosity of the gas phase does not vary significantly over the intermediate range of saturations in our case.

3.3.4 Macroscopic specific interfacial area

Using PNM drying simulations, we compute the specific interfacial area a_{gl}, i.e. the sum of interfacial area of the interfacial throats contained within a local averaging slice divided by the macroscopic volume of this slice. Initially, each local slice has approximately the same moderate value of a_{gl} of around 150 m^2/m^3, as illustrated in Fig. 3.7.

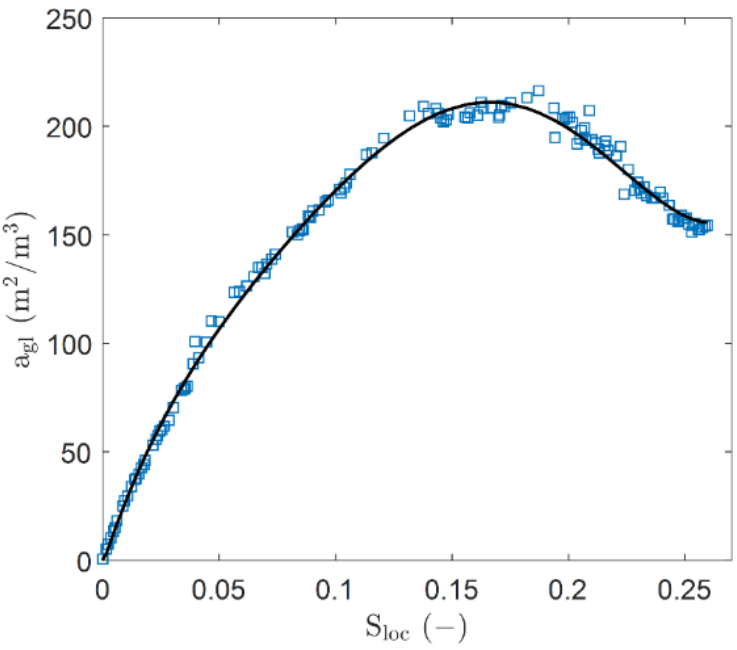

Fig. 3.7: Specific interfacial area a_{gl} as a function of local saturation S_{loc}. The data points are averaged over finite local saturation intervals. The black solid line is a fitted function of a_{gl} out of the discrete data points (blue symbols).

As the drying process begins, the uniformly distributed liquid clusters in the evaporating slices split into isolated meniscus throats. The total interfacial area of these resulting isolated menisci is greater than that of the parent cluster. This phenomenon is the cause of the initial increase in a_{gl} until a peak is reached at around S_{loc} = 0.16. Upon further drying, the rate of local production of interfacial area is overcome by the rate of removal of liquid throats, resulting in consistent decrease of a_{gl} with local saturation.

A key parameter introduced in the two-equation NLE CM is the specific interfacial area a_{gl}. It is a measure of liquid or gas phase tortuosity in a two-phase flow situation and is considered very important especially in the modeling of drainage process inside a porous medium. The general shape of the a_{gl} curve as illustrated in Fig. 3.7 is consistent with several previous results from the literature. For example in Joekar-Niasar et al. (2008, 2010) we see a similar non-monotonic polynomial relationship between saturation and specific interfacial area. For comparison with experimental results we can refer to Culligan et al. (2006), where drainage experiments are performed on glass beads that have a_{gl} values in a similar range as the one shown Fig. 3.7, i.e. from 0 to 0.23 mm^{-1}. More recently, the work done by Wang et al. (2019) has also qualitatively validated the specific interfacial area function.

While operating in the limiting regime of immobile liquid phase, we could work with different degrees of initial network saturation $S_{net,ini}$. In order to illustrate the effect of degree of initial network saturation on a_{gl}, we arbitrarily selected 4 different values of initial network saturation and performed 15 simulations for each value of $S_{net,ini}$, each with a different realization of throat size distribution and location of liquid clusters. In Fig. 3.8 the averaged a_{gl} obtained from the various realizations for each case of $S_{net,ini}$ is illustrated. For all $S_{net,ini}$, we see a qualitatively similar trend, i.e. an initial increase in a_{gl} followed by a consistent decrease with decreasing local saturation. When the results of different $S_{net,ini}$ are compared quantitatively, it is observed that overall the a_{gl} values decrease with decrease in $S_{net,ini}$ for their respective local saturation values. This is owed to the fact that while operating in the limiting regime of immobile liquid

phase, the total interfacial area per unit volume is higher when there are more liquid throats per unit volume.

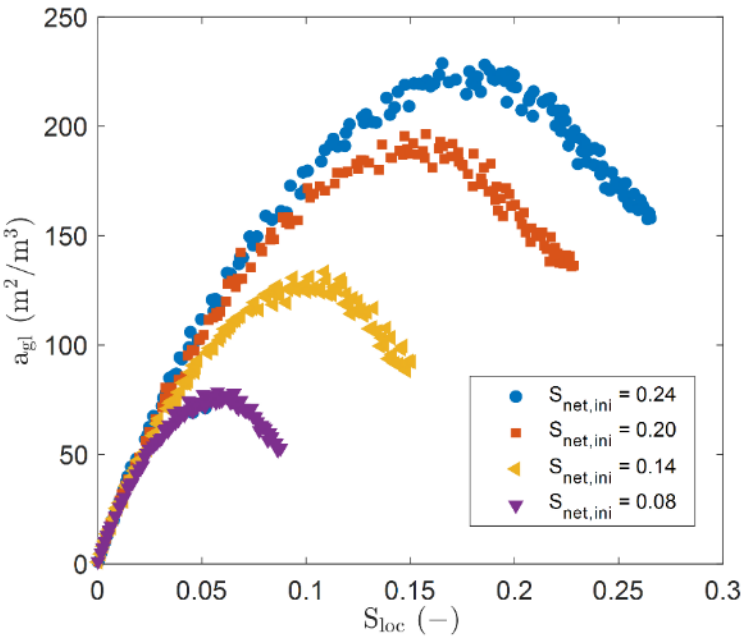

Fig. 3.8: Specific interfacial area a_{gl} as a function of local saturation S_{loc} simulated with varying degree of $S_{net,ini}$. Each of the four functions presented here is the result of averaging of 15 simulations, each with different realizations of the randomly generated throat size distribution and the liquid structure.

This dependency of a_{gl} on the initial saturation illustrated in Fig. 3.8 can be related to some considerations about a_{gl} in two-phase flow modeling, where the specific interfacial area is modeled by a dedicated conservation equation (e.g. Hassanizadeh and Gray, 1990, 1993). As shown in Joekar-Niasar et al. (2008), the classical capillary pressure-saturation relationship is incomplete without the consideration of specific interfacial area. Considering the interfacial area is a vital step to circumvent the hysteresis in the relationships between capillary pressure and relative permeability and saturation. Here, the results shown in Fig. 3.8 can be seen as another illustration of the fact that the saturation alone is not sufficient to derive the macroscopic parameters, since the parametrization of the NLE phase change term in the NLE CM, i.e. Eq. (3.3), in fact depends on the initial network saturation $S_{net,ini}$ through the dependency of a_{gl} on $S_{net,ini}$ illustrated in Fig. 3.8.

Also, it can be noted from Fig. 3.8, that a_{gl} varies roughly linearly with local saturation for sufficiently low local saturation values. Then, it can be observed that our expression of the phase change term, i.e. Eq. (3.26), is consistent with the expression used in Li et al. (2019) or Pujol et al. (2011), namely $\dot{m} = b\varepsilon(S - S_{res})\frac{\tilde{R}T}{\tilde{M}_v}\left(P_{v,eq} - P_v\right)$ in this range of saturation, which is the most critical for the NLE effect according to Figs. 3.5 and 3.7.

3.3.5 Comparison of solution of CM with PNM simulation results

The macroscopic effective vapor diffusivity D_{eff} and specific interfacial area a_{gl} (indicated by fitted functions illustrated in Fig. 3.6 and Fig. 3.7, respectively) obtained from PNM drying simulations are used to solve the two-equation CM (Eqs. (3.1) and (3.2)). The only missing parameter is the mass exchange coefficient k. The latter is used as a fitting parameter. Figure 3.4 shows the saturation profiles and normalized vapor pressure profiles obtained from the solution of two-equation CM at seven distinct times compared with corresponding PNM simulation results for the k value of 0.05 m/s. Note that k is independent of local saturation. The comparison of saturation and vapor pressure profiles indicates that the two-equation CM reproduces the profiles with good accuracy.

Figure 3.9 shows the evaporation rate obtained by the NLE CM compared with the evaporation rate obtained from corresponding PNM simulations results. The initial saturation assigned to the discretized finite volume elements of the CM is 0.26 and the corresponding initial vapor partial pressure is given as $P_{v,sat}$ for all slices. The assigned initial condition for P_v is the reason for the higher initial value of evaporation rate of CM simulation compared to the corresponding initial value of PNM simulation (as can be seen in Fig. 3.9). However, the CM adjusts the value of P_v of surface volume element (and the surrounding elements) very quickly (in the first second of drying time), therefore this discrepancy in the initial evaporation rate does not affect the solution.

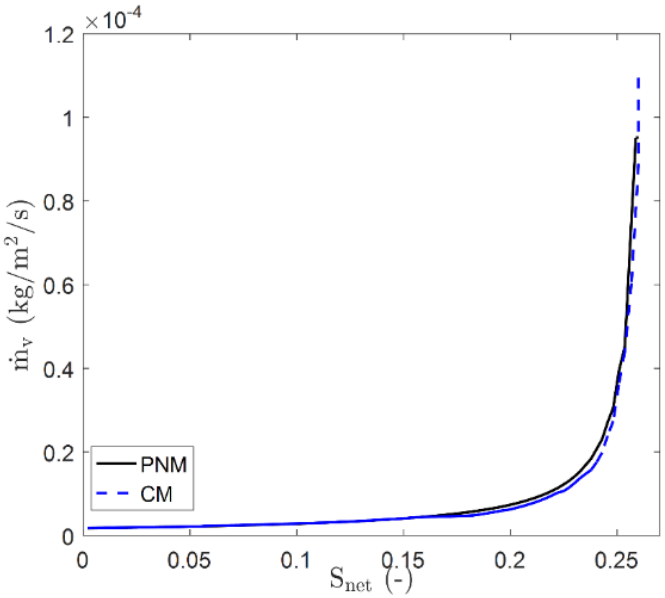

Fig. 3.9: Comparison of evaporation rates obtained from PNM drying simulations and those predicted by the two-equation CM.

Additionally, we can analyze the ability of the two-equation CM to reproduce the NLE effect. This is illustrated in Fig. 3.10. In doing so, we illustrate the comparison of NLE effect reproduced by the two-equation CM simulation and the corresponding PNM simulation results for varying ranges of network saturation. Based on the convergence of saturation profiles, vapor pressure profiles, total evaporation rate and the NLE effect, it can be said that the two-equation NLE CM produces good results.

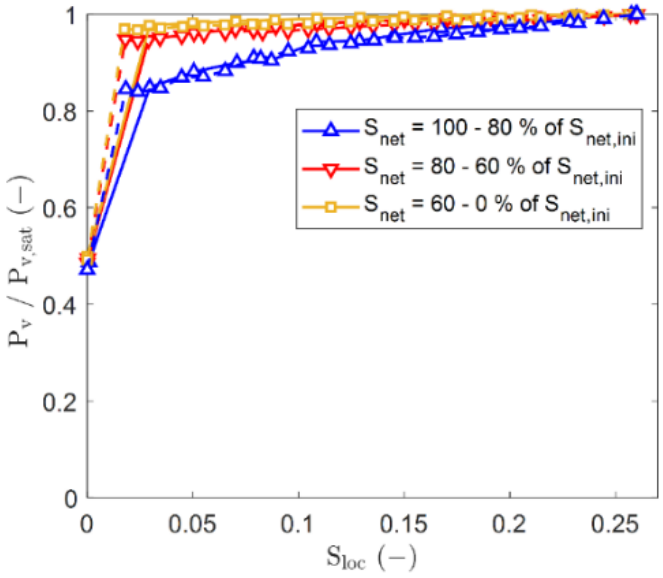

Fig. 3.10: NLE effect obtained from PNM drying simulation and solution of two-equation NLE CM for varying ranges of S_{net}. The solid lines represent the PNM results and the dashed lines represent NLE CM simulation results.

3.3.6 NLE CM simulation results compared with LE front model

Since the drying front is quite sharp, the particular situation considered in this work is classically analyzed using a traveling front model under the assumption of local equilibrium, $P_v = P_{v,sat}$ at the front, i.e. regardless of the degree of local saturation within the front region. Under the classical quasi-steady approximation for the water vapor transport, the mass balance at the front is expressed as

$$j_v = \frac{\tilde{M}_v}{\tilde{R}\,T} D_{eff}^{*} \frac{P_{v,sat} - P_{v,surf}}{z_f} = \varepsilon \rho_l S_{net,ini} \frac{dz_f}{dt}, \tag{3.30}$$

where z_f denotes the position of the front (distance from the surface) and $S_{net,ini}$ the initial network saturation. Combining Eq. (3.30) with the right-hand side of Eq. (3.27), i.e. $j_v = \frac{\tilde{M}_v}{\tilde{R}\,T} D_{va} \frac{P_{v,surf} - P_{v,\infty}}{L_{bl}}$, leads to an ordinary differential equation which can be solved analytically. This leads to a solution where the front position typically scales with the square root of time, i.e. $z_f \propto \sqrt{t}$. In what follows, the LE front model is referred to as the LE CM.

Figure 3.11 shows the drying front position predicted by LE CM compared with that obtained from PNM drying simulations and the two-equation NLE CM. It can be seen that the NLE CM reproduces the drying front position very well. On the other hand, the drying front position predicted by the LE CM is shifted by a certain amount in relation to that obtained from PNM drying simulations.

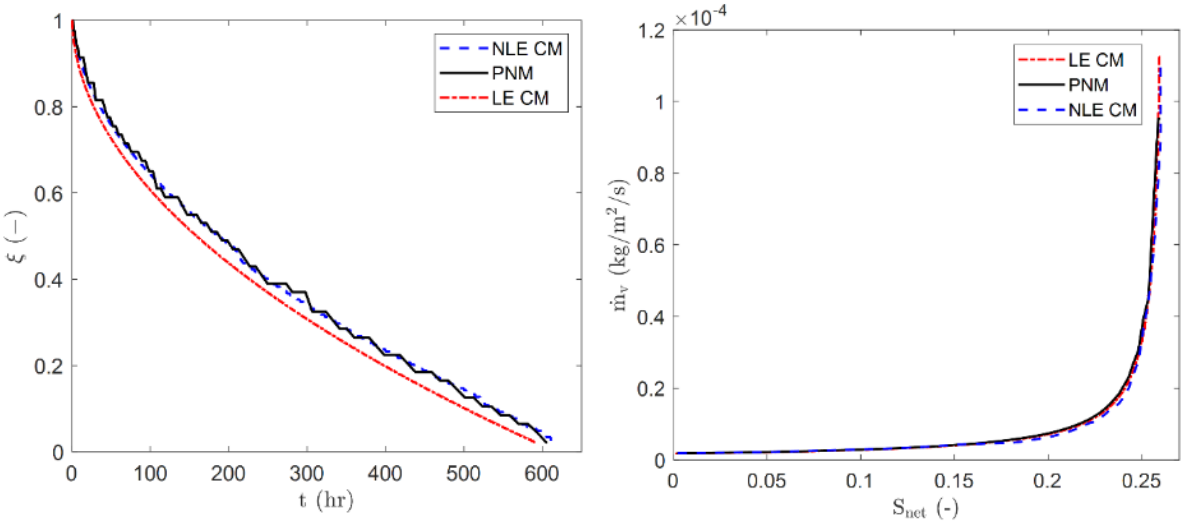

Fig. 3.11: (Left) Variation of normalized drying front position ξ with respect to time. (Right) Total evaporation rate per unit area with respect to network saturation. Both figures present a comparison of results of PNM drying simulations presented in Sec. 3.3.1 and the corresponding NLE CM and LE CM simulation results.

The corresponding comparison of evaporation rate however reveals that the evaporation rates from PNM, LE CM and NLE CM do not differ significantly in the course of the process. Though it should be noted that in NLE CM, the initial evaporation rate drops instantaneously to the correct value corresponding to the initial evaporation rate of the PNM results. On the other hand, in the LE CM the initially overestimated drying rate affects the overall drying time as well as the drying front position as can be seen in the comparison of drying front position with respect to time (Fig. 3.11). Consistently with the NLE curves in Figs. 3.5 and 3.10, the impact of the NLE effect is only important at the beginning of the drying process when the drying front is at the surface or very close to it. Nevertheless, the impact of the error at the beginning associated with the LE CM affects the position of the drying front as illustrated in Fig. 3.11.

3.3.7 Comparison with the receding front period

The saturation evolution depicted in Fig. 3.4 resembles the evolution in the receding front period (RFP) reported in several previous works where the profiles were determined experimentally (e.g. Pel et al., 2002b; Pel et al., 1996). However, there is an important difference. In the experimental results presented (Pel et al., 2002b; Pel et al., 1996), the position of the front scales linearly with time, see also Lockington et al. (2003), whereas in our case the front position scales with the square root of time (Fig. 3.11). The difference is due to the impact of the viscous effects, which are completely neglected in our simulations since the liquid phase is disconnected. In the experiments, the liquid is still connected, i.e. percolating between the front and the sample bottom, and the receding of the front results from the balance between the evaporation rate and the liquid flow at the front. In other words, the situation considered in our simulations rather corresponds to the special case where viscous effects in the liquid can be completely neglected compared to capillary effects. In this

limiting case, the liquid phase is disrupted during the receding front period, as shown for instance in Le Bray and Prat (1999).

3.4 Remarks

In this chapter, a non-local equilibrium (NLE) continuum model (CM) of drying was studied by comparison with pore network simulations for the case where the liquid phase is initially distributed in the form of small disconnected clusters. The CM was derived with the help of the volume averaging method. This led to the introduction of the specific interfacial area in the formulation of the NLE phase change term. Also, the upscaling suggests that there is no particular reason for introducing an enhancement factor in the vapor diffusion model.

Pore network model (PNM) simulations indicated that an NLE effect should be expected not only for hygroscopic materials, as suggested in several previous works (Bénet and Jouanna, 1982; Bénet et al., 2009; Ouedraogo et al., 2013), but also in the case of capillary porous materials. The study also indicates that the NLE effect is particularly marked at the surface. This should be considered in the modeling of the coupling between the internal transfer, i.e. inside the porous medium, and the external transfer, i.e. within the external boundary layer. In other words, the study suggests that a significant improvement in the modeling of the drying process by means of continuum models can be expected from the consideration of the NLE effect in the porous medium evaporative surface region.

The NLE CM led to a good agreement with the PNM drying simulations in both the saturation profiles and the drying kinetics. However, for the considered situation, the NLE CM leads to only slightly better results than the simpler LE front model. Nevertheless, the NLE CM is much more conceptually consistent with the drying PNM simulations which clearly indicate an NLE effect.

Like other macroscopic parameters, such as the capillary pressure curve or the relative permeabilities, the parameters of the drying model can be determined from PNM simulations. Within the framework of PNM, it is more classical to determine the parameters using dedicated algorithms. We mean here, for instance, a specific

algorithm to determine the permeability curve or the capillary pressure curve, see, e.g., Blunt et al. (2001) and references therein. In this respect, it would be interesting to develop a specific algorithm for determining the mass transfer coefficient k (that was used as a fitting coefficient in our two-equation continuum model) of the NLE phase change term, so as to study the impact of microstructure on this coefficient. For this purpose, in the framework of volume averaging method, this would require the development of the closure problem in order to compute k.

Chapter 4

NLE continuum modeling for a fully saturated capillary porous medium

Part of this chapter will be published as "Ahmad, F., Prat, M., Tsotsas, E., Kharaghani, A. Two-equation continuum model of drying appraised by comparison with pore network simulations".

Based on the findings in Attari Moghaddam et al. (2017), a CM was developed and presented in Chapter 3 (Ahmad et al., 2020) for a transport regime in which the NLE effect (already described in detail in Chapter 3) was expected to be more pronounced. In this transport regime, the mass transfer inside the porous medium is purely through vapor diffusion in the gas phase because the liquid phase is distributed into isolated clusters. The results indicated that the NLE mass exchange between the liquid and vapor phase was captured well by the introduction of a source/sink term that couples the liquid and vapor phase transport equations. In this chapter, we advance this NLE CM presented in Chapter 3 by considering a fully saturated capillary porous medium, whereby the mass transport within the porous medium is through liquid capillary pumping, vapor diffusion and the local evaporation through NLE mass exchange between the two phases.

Hints about the coupling of the internal mass transfer and the external transport in the boundary layer are obtained from the findings presented in Attari Moghaddam

et al. (2018). The formulation of the NLE phase change term is the same as presented in Sec. 3.1. As in Chapter 3 and the rest of the thesis, a slow drying situation where temperature variations can be neglected is considered. Also, the archetypical drying situation where the drying process is macroscopically 1D with the evaporative surface at the top is considered.

4.1 Description of the NLE CM for fully saturated porous medium

The NLE CM is based on a mass conservation equation for the liquid phase and a mass conservation equation for the vapor phase. Considering the gas phase as a binary mixture of the vapor and a stagnant gas (typically water vapor and air in many applications), these equations read, respectively,

$$\varepsilon\rho_l \frac{\partial S}{\partial t} + \nabla.(\rho_l U_D) = -\dot{m}, \tag{4.1}$$

and

$$\nabla.\left(\varepsilon(1-S)D_{eff}\frac{\widetilde{M}_v}{\tilde{R}T}\nabla P_v\right) + \dot{m} = 0, \tag{4.2}$$

where ε is the porosity, S the saturation, ρ_l the liquid mass density, U_D the liquid Darcy (filtration) velocity, $\widetilde{M}_v$ the molar mass of vapor, $\tilde{R}$ the universal gas constant, T the temperature, P_v the vapor partial pressure, D_{eff} the effective vapor diffusion coefficient and $\dot{m}$ the evaporation rate. As can be seen from Eq. (4.2), we have used the conventional quasi-steady-state assumption as regards the vapor transport. The liquid filtration velocity is expressed using the generalized Darcy's law as

$$U_D = -\frac{\kappa\kappa_r}{\mu_l}\nabla P_l, \tag{4.3}$$

where κ is the permeability, κ_r is the liquid phase relative permeability, μ_l is the liquid dynamic viscosity and P_l is the liquid pressure. Introducing the capillary curve $P_c(S)$ and noting that the total pressure in the gas phase is considered as constant, Eqs. (4.1) and (4.3) are combined to obtain

$$\varepsilon\rho_l \frac{\partial S}{\partial t} = \nabla.(\rho_l D_l(\mathrm{S})\nabla S) - \dot{m}, \tag{4.4}$$

where

$$D_l(\mathrm{S}) = -\frac{\kappa\kappa_r}{\mu}\frac{dP_c}{dS}. \tag{4.5}$$

The internal volumetric evaporation rate $\dot{m}$ is expressed as

$$\dot{m} = a_{lg}k\frac{\widetilde{M}_v}{\tilde{R}T}(P_{v,sat} - P_v), \tag{4.6}$$

where a_{lg} is the interfacial area between the gas phase and the liquid phase per unit volume of porous medium inside the REV, k is the mass exchange coefficient, $P_{v,sat}$ is the saturation vapor pressure. The mass exchange coefficient k controls the extent of the local change between the liquid and the vapor phases. For details on the formulation and upscaling of $\dot{m}$, one can refer to Chapter 3. Combining Eqs. (4.1)-(4.6), the two-equation NLE CM for drying is deduced, where the equation for the liquid phase reads

$$\varepsilon\rho_l\frac{\partial S}{\partial t} = \nabla.(\rho_l D_l(\mathrm{S})\nabla S) - a_{lg}k\frac{\widetilde{M}_v}{\tilde{R}T}(P_{v,sat} - P_v), \tag{4.7}$$

and for the gas phase follows

$$\nabla.\left(\varepsilon(1-S)D_{eff}\frac{\widetilde{M}_v}{\tilde{R}T}\nabla P_v\right) + a_{lg}k\frac{\widetilde{M}_v}{\tilde{R}T}\left(P_{v,sat} - P_v\right) = 0. \tag{4.8}$$

The boundary condition at the solid limiting surface is a no flux condition which reads

$$-\rho_l D_l(\mathrm{S})\nabla S.\mathbf{n} = 0, \tag{4.9}$$

and

$$-\varepsilon(1-S)D_{eff}\frac{\widetilde{M}_v}{\tilde{R}T}\nabla P_v.\mathbf{n} = 0. \tag{4.10}$$

In Eqs. (4.9) and (4.10) $\mathbf{n}$ is a unit vector normal to the considered surface. The boundary condition at the open surface where the porous medium is in contact with the external gas (air typically) is much less obvious and actually still one major issue in the modeling of the drying process. In the case of the two-equation model, two boundary conditions must be imposed, one for the liquid transport equation (Eq. (4.7)) and one for the vapor transport equation (Eq. (4.8)). Consider the situation starting right after the very beginning of drying when a fraction of the network has

been dried and the liquid and gas phases coexist in the porous medium at the surface. Physically, one then expects that a fraction of the vapor flux at the surface is from the dry surface pores, whereas the complementary fraction corresponds to the evaporation from the liquid pores at the surface. Based on a classical boundary layer type expression for the vapor flux at the surface, this is expressed as

$$-\rho_l D_l(\mathrm{S})\nabla S.\,\mathbf{n} = (1 - A_{surf,dry})\, D_{va} \frac{\widetilde{M}_v}{\tilde{R}T} \frac{(P_{v,sat} - P_{v,\infty})}{L_{bl}} \tag{4.11}$$

for the liquid phase equation and

$$-\varepsilon(1-S) D_{eff} \frac{\widetilde{M}_v}{\tilde{R}T} \nabla P_v.\,\mathbf{n} = A_{surf,dry}\, D_{va} \frac{\widetilde{M}_v}{\tilde{R}T} \frac{(P_{v,surf} - P_{v,\infty})}{L_{bl}} \tag{4.12}$$

for the vapor phase equation. Here, **n** is the unit normal vector directed from the porous medium surface toward the external gas boundary layer, D_{va} is the molecular diffusion coefficient, L_{bl} is the external boundary layer thickness and $P_{v,\infty}$ is the vapor partial pressure in the external gas away from the porous medium surface. In Eqs. (4.11) and (4.12), $A_{surf,dry}$ represents the fractional contribution of the dry pores to the evaporation rate, whereas the relative contribution of the wet pores to the evaporation rate is expressed by $(1 - A_{surf,dry})$. An obvious first choice is to simplify the problem and specify $A_{surf,dry}$ according to $A_{surf,dry} = 1 - \mathrm{S}_{surf}$, where S_{surf} is the saturation at the considered surface. Physically, it is expected that the vapor pressure at the surface gradually decreases along the drying process. $A_{surf,dry}$ as computed from PNM simulations will be presented later in Sec. 4.2.4. A study based on the impact of considering linear and non-linear relationship between S_{surf} and $A_{surf,dry}$ will also be presented in Sec. 4.4.4.

The one-dimensional two-equation CM is solved in MATLAB by discretizing the computational domain using the finite volume method. A fixed domain approach is considered. When the saturation becomes locally lower than a given residual value, denoted by S_{res}, then the saturation is assigned as $S = S_{res}$. In the simulations presented later in this chapter, S_{res} was taken equal to 10^{-6}.

4.2 Macroscopic transport parameters

For the solution of the liquid and vapor phase CM equations (Eqs. (4.7) and (4.8)), macroscopic transport parameters are required. Traditionally, these parameters have been determined from laboratory experiments. However, as an alternate to the tedious laboratory experiments, numerical PNM simulations have also been used to determine these parameters. In the laboratory experiments, the measured transient saturation profiles (e.g. Gomez et al., 2007; Marchand et al., 1994; Pel et al., 1996; Schoeber, 1976) are used to compute the moisture transport coefficient. This moisture transport coefficient is in fact the combined transport coefficient for the liquid and vapor phases. On the other hand, the use of dedicated numerical PNM simulations traditionally aims at computing the capillary pressure curve and the absolute and relative permeabilities (Blunt et al., 2001; Jabbari et al., 2019; Joekar-Niasar et al., 2011; Øren et al., 1998) based on the process of drainage. For the case of drying, however, the use of PNM simulations is similar to the experimental approach, i.e. it is based on the determination of saturation profiles (Attari Moghaddam et al., 2017b; Nowicki et al., 1992) and also on vapor pressure profiles obtained by the volume averaging method (as shown in Chapter 3). This approach consists of discretizing the PNM domain into slices or local averaging volumes, where the parameters are computed and averaged over the individual slices. Based on the locally averaged saturation and vapor pressure profiles, the macroscopic liquid and vapor phase diffusivities are computed. The method of discretization of the 3D PNM domain into 1D macroscopic domain is the same as described in Chapter 3 (see Fig. 3.2). For more details on the method of discretization and the method of computation of macroscopic parameters from PNM simulations, see Sec. 3.2.

Since the solution of the drying CM will be compared with PNM simulations, it is important to mention the size of the pore network and the local averaging volume over which the parameters are averaged. Due to the computational bottleneck associated with PNM simulations, the size of the pore network is 25×25×51 i.e. 51 nodes in the direction of the boundary layer. The size of the local averaging volume is equal to the size of one lattice spacing (the distance between two successive nodes) in

the vertical direction and to the size of the network in the lateral dimensions. Due to this small network size, we cannot claim that the macroscopic parameters computed from PNM simulations are in fact local. The size of local averaging volume for our PNM simulations should be rather 25 pores in each direction (Attari Moghaddam et al., 2017b) in order to be representative of the porous medium. This means that our local averaging volume and network size are much too small to fulfil the traditional length scale separation criterion (Whitaker, 1977).

The fulfillment of length scale separation criterion ensures that the transport parameters are local, i.e. they only depend on the local saturation that is the saturation over a representative elementary volume (REV). As a result, the macroscopic parameters determined over a too thin system, which do not fulfil the length scale separation criterion, may be influenced by the size of the system. As in other systems affected by finite size effects, e.g. Stauffer et al. (2018), the consideration of a small network leads to a significant data scatter in the macroscopic parameters computed from PNM simulations. In Attari Moghaddam et al. (2017), this led to consider that the macroscopic parameters were dependent on both the local saturation, i.e. the slice averaged saturation, and the overall saturation, i.e. the whole network saturation. Although interesting for the modeling of drying in thin systems, this latter approach is not relevant for the modeling of the frequently encountered systems for which the length scale separation criterion is fulfilled. For this reason, we consider in what follows macroscopic parameters that only depend on the local saturation, as traditionally considered in the classical theory of two-phase flow in porous media under the local capillary equilibrium assumption (Whitaker, 1986). Nevertheless, even though our CM is preferentially developed for systems with well separated length scales, comparisons will be performed with the results of the PNM simulations. In other words, it will be shown that insightful comparisons between the CM model and the PNM simulations can be developed despite the network small size.

In what follows, we present the profiles of the macroscopic parameters, which are used to obtain CM solution presented in Sec. 4.3, with the corresponding macroscopic parameters computed from PNM simulations for comparison. The influence of the macroscopic parameters on the CM solution will be discussed later in Sec. 4.4.

4.2.1 Liquid phase diffusivity

The liquid phase diffusivity directly controls the evolution of the liquid phase within the network. The liquid diffusivity D_l is obtained from PNM simulation results as

$$D_l = -\frac{j_l}{\rho_l \nabla S}, \tag{4.13}$$

where j_l is local liquid flux crossing the considered averaging slice, whereas ∇S is the saturation difference between the two averaging slices adjacent to the considered plane divided by the distance between the two slices, i.e. the lattice spacing. As the other macroscopic parameters, D_l is computed considering 15 realizations of the networks and saturation intervals of 0.01. For each realization of the throat size distribution, a given saturation interval can thus be obtained at various locations in the network. This means that several values of D_l are assigned to each considered saturation interval from the consideration of the various slices over time and the 15 realizations. As a result, owing to the small network size and averaging slice thickness, the liquid phase diffusivity obtained from PNM simulations shows a large scatter in the D_l values for each local saturation value. The idea is to specify D_l as sufficiently representative of the PNM microstructure in spite of the scattering.

It can be first noticed that Figure 4.1 shows that liquid phase diffusivity computed from PNM simulations is significantly larger when the local saturation is larger than the irreducible saturation S_{irr}, that is, the value of local saturation at which the continuity of the liquid phase is disrupted (the liquid phase gets fragmented into disconnected clusters). As reported in Attari Moghaddam et al. (2017), for our pore network S_{irr} is computed to approximately 0.68 . Due to the small vertical size of our local averaging volume (one lattice spacing), the isolated clusters span over more than one averaging volume and thus we obtain D_l values for $S < S_{irr}$ in the range of 10^{-14} – 10^{-10} m^2/s (as illustrated in Fig. 4.1).

In order to reproduce saturation profiles that are close to those obtained from PNM simulation results (presented in Sec. 4.3), we adopt the D_l to the averaged PNM data. As reported in Attari Moghaddam et al. (2017), we also observed that for reproducing the saturation profiles of the PNM, the D_l values should be significantly higher for $S > S_{irr}$ as compared to $S < S_{irr}$. We observed, moreover, that profiles of D_l that decrease

exponentially as we approach zero local saturation give better results. Based on these observations, a piece-wise profile was seen as the most adequate function for D_l where

$$D_l = a_1 exp(b_1 {S_{loc}}^{c_1}) \tag{4.14}$$

for $S_{loc} < S_{irr}$, and

$$D_l = a_2 S_{loc} + b_2 \tag{4.15}$$

for $S_{loc} > S_{irr}$. Equation (4.14) is based on an exponential function where the values of coefficients a_1, b_1 and c_1 are 1.92×10^{-12}, 2 and 0.5, whereas Eq. (4.15) is a linear function where a_2, b_2 are equal to 2.16×10^{-9} and -1.46×10^{-9}, respectively. In Fig. 4.1, we present the comparison of D_l based on Eqs. (4.14) and (4.15) and the discrete data points of D_l obtained from PNM simulation results over the 15 realizations, which are computed from local liquid flux j_l based on Eq. (4.13)). Note that the ordinate in Fig. 4.1 is logarithmic, which causes the linear profile of D_l for $S > S_{irr}$ to appear as non-linear.

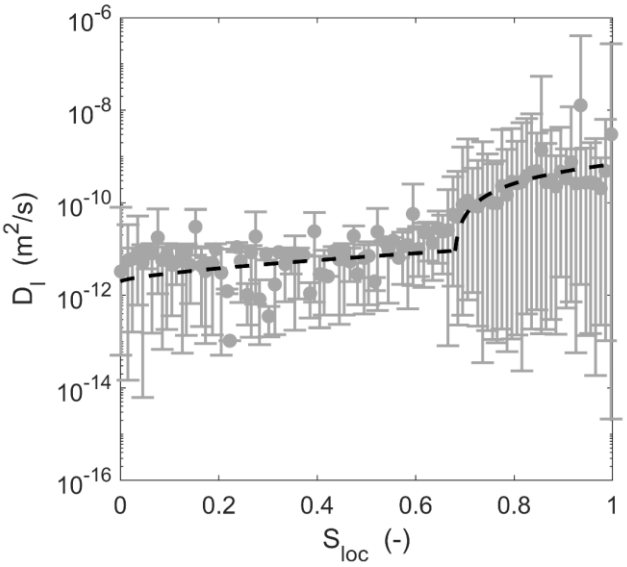

Fig. 4.1: Macroscopic liquid phase diffusivity D_l with respect to local saturation S_{loc} obtained from pore network simulations over 15 realizations. The black dashed line represents the macroscopic liquid diffusivity based on Eqs. (4.14) and (4.15). The vertical bars show the spread of the D_l obtained from PNM simulations based on Eq. (4.13) for the whole range of network saturation and the circular dots show the average of the PNM data. The discrete PNM data is averaged over local saturation intervals of 0.01.

4.2.2 Water vapor diffusivity

The formulation of the vapor diffusivity can be performed in a simpler manner as compared to the liquid phase diffusivity. This is because unlike the liquid phase diffusivity, which in fact is a lumped parameter describing the liquid viscous-capillary transport, macroscopic vapor diffusivity has a similar physical meaning and formulation (vapor pressure gradient as the driving force) as that of the pore scale vapor diffusion coefficient. Based on the upscaling procedure, similar to our related previous work (Ahmad et al., 2020), we do not consider any enhancement effect (see, e.g., Plumb et al., 1999) caused by the water evaporation in the vapor diffusion formulation. A logical first step here is to consider the situation of vapor transport through completely dry region, i.e. for region where the local saturation is zero. We refer to it as D_{eff}^{*} i.e., $D_{eff}(S_{loc} = 0)$. For our pore network, D_{eff}^{*} can be approximated from a relation based on the pore scale vapor diffusion coefficient D_{va}, the average throat radius and throat length, which can be represented as

$$\frac{\varepsilon D_{eff}^{*}}{D_{va}} \approx \frac{\pi\, r_{t,mean}^{2}}{L_{t}^{2}}. \tag{4.16}$$

Using Eq. (4.16), D_{eff}^{*} can be expressed in terms of PNM structural characteristics and can be directly computed without performing any PNM simulations. Equation (4.16) is similar to the formulation for D_{eff}^{*} presented in Vorhauer et al. (2010), where effective vapor diffusivity for drying PNM is presented based on a simple drying model with the assumption of local equilibrium at the macroscopic scale between liquid and vapor phase. However, as opposed to the formulation of vapor diffusion presented in this work, in Vorhauer et al. (2010) the porosity is implicit in the effective vapor diffusivity term. This is why we consider the term εD_{eff}^{*} in Eq. (4.16). Note that this is an empirical formulation specific to our considered PNM. For our PNM geometry (parameters given in Sec. 4.3), the value of D_{eff}^{*} is equal to approximately 8.6x10^{-6} m^2/s. Figure 4.2 shows D_{eff} computed from PNM simulations as,

$$D_{eff} = -\frac{\tilde{R}\,T}{\widetilde{M}_{v}} \frac{j_{v}}{\varepsilon(1-S)\,\nabla P_{v}}, \tag{4.17}$$

where j_v is the total vapor flux between two local averaging volumes driven by the macroscopic vapor pressure gradient between them. In the term $(1 - S)$ in Eq. (4.17), we considered the average value of the saturation of the two averaging volumes between which the vapor flow is considered. As expected, the value of D_{eff} is smaller where the resistance to vapor flow i.e. liquid phase saturation is larger. When compared with D_{eff} computed from PNM simulations based on Eq. (4.17), the average value of D^*_{eff} is approximately the same as that computed from Eq. (4.16). Similar to the liquid phase diffusivity, the effective vapor diffusivity obtained from PNM simulations also has a large scatter in the data, owing to the small size of the local averaging volume.

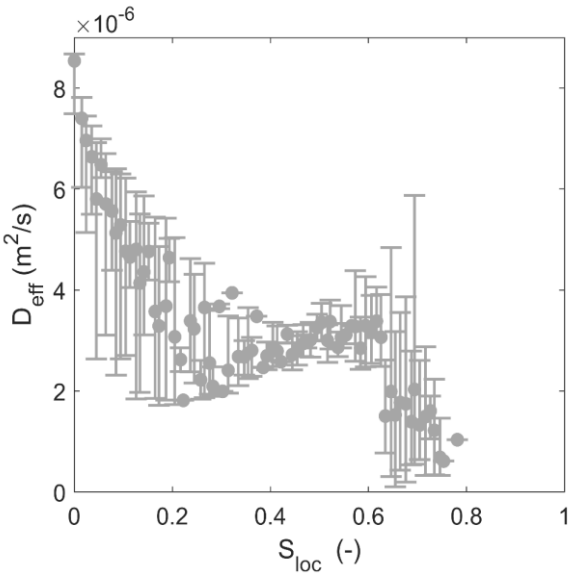

Fig. 4.2: Effective water vapor diffusivity D_{eff} with respect to local saturation S_{loc} computed from PNM simulation over 15 realizations. The vertical bars show the spread in D_{eff} values obtained from PNM simulations for whole range of network saturation and the circular dots show the average of the PNM data. The discrete PNM data is averaged for local saturation intervals of 0.01.

While considering the upscaling of the vapor diffusivity, the ratio between the effective vapor diffusivity and the pore-scale vapor diffusion coefficient is based on the tortuosity coefficient (which depends on the porous medium geometry and the gas phase saturation). For example, for granular porous medium, it is represented as $D_{eff}/D_{va} = (\varepsilon(1 - S))^{10/3}/\varepsilon^2$ (Millington et al., 1961; Moldrup et al., 2001; Ouedraogo

et al., 2013). However, for the solution of the CM presented in Sec. 4.3, we do not consider the effective diffusivity computed from PNM simulations as illustrated in Fig. 4.2. Instead, we neglect the influence of local saturation on the effective vapor diffusivity and test a simpler approach by considering the effective vapor diffusivity to be equal to D^*_{eff} i.e., independent of local saturation. This means that the main impact of the saturation on the macroscopic vapor diffusive transport is via the gas volume fraction $\varepsilon(1-S)$. Note that this simplification is specific to the situation considered in this work and is a mere simplification which would need to be reconsidered depending on the porous medium.

4.2.3 Specific interfacial area

Figure 4.3 shows the comparison of specific interfacial area a_{gl} (computed by dividing the total interfacial area of all interfacial throats within a local averaging volume with the local macroscopic volume) obtained from PNM simulation results and the profile used for the CM solution.

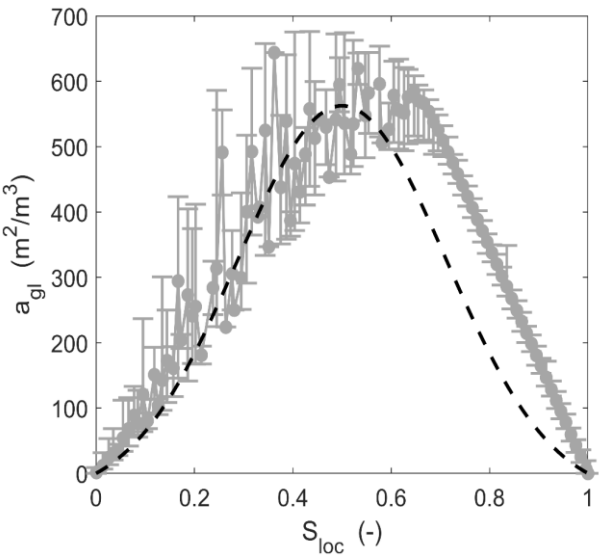

Fig. 4.3: Specific interfacial area a_{gl} as a function of local saturation S_{loc}. The vertical bars show the spread of a_{gl} computed from PNM simulations for whole range network saturation S_{net} and circular dots show the averaged a_{gl} for each local saturation interval of 0.01. The pore network simulation results are averaged over 15 realizations. Black dashed line represents the CM profile based on Eq. (4.18).

Initially, i.e., at S_{loc} = 1, the value of a_{gl} of each local slice is zero (except for the surface slice as the surface throats are exposed to the boundary layer in the beginning of the drying process). As S_{loc} deviates from unity, a_{gl} increases owing to the formation of meniscus throats. This leads to a consistent increase in a_{gl} with decrease in local saturation until a peak value is reached. Upon further drying, a_{gl} decreases consistently with local saturation as the rate of removal of liquid overcomes the rate of local production of a_{gl}.

For $S_{loc} < S_{irr}$ the specific interfacial area profile computed from PNM simulations shows scattered clouds of data similar to that of the other macroscopic transport parameters computed from PNM simulations as discussed in the above sections. For local saturation values larger than roughly the irreducible saturation S_{irr}, the specific interfacial area computed from PNM simulations does not show any scatter. As will be shown later, this is also the range of local saturation in which the deviation of vapor pressure from saturation vapor pressure is negligible. This implies that the a_{gl} profile for $S_{loc} > S_{irr}$ does not influence the CM solution. Considering this, a_{gl} profile used for CM solution complies roughly with PNM. This profile used for CM solution is expressed as

$$a_{gl} = a_3 exp\left(-\left(\frac{S_{loc}-b_3}{c_3}\right)^2\right) + d_3 \,, \tag{4.18}$$

where values of the coefficients a_3, b_3, c_3 and d_3 are 600, 0.5, 0.3, and -37.30591 m^2/m^3, respectively.

4.2.4 Interfacial area at the surface

In the surface slice, the dynamics of interfacial area with respect to local saturation is different from that of the rest of the network. This is owed primarily to the fact that the surface slice consists only of vertical surface throats as the surface pores do not have any horizontal throats connected to them (slices in the rest of the network consist of vertical and the horizontal throats connected to the upper pore-node of the slice). Hence, there is no increase in the total number of interfacial throats in the surface slice with decrease in saturation. From PNM simulations, $A_{surf,dry}$ is obtained by subtracting from unity the ratio of sum of interfacial area of saturated surface throats

to the sum of interfacial area of all surface throats. As illustrated in Fig. 4.4, $A_{surf,dry}$ computed from PNM simulations is a slightly non-linear function of surface saturation. However, for the CM solution a non-linear relationship defined as

$$A_{surf,dry} = \left(1 - S_{surf}\right)^2, \tag{4.19}$$

where S_{surf} is the saturation of the surface slice, leads to more satisfactory results (see Sec. 4.3). The impact of $A_{surf,dry}$ on the CM solution is further studied in Sec. 4.4.4, where we also present a solution based on linear relationship between $A_{surf,dry}$ and S_{surf}, i.e. $A_{surf,dry} = 1 - S_{surf}$.

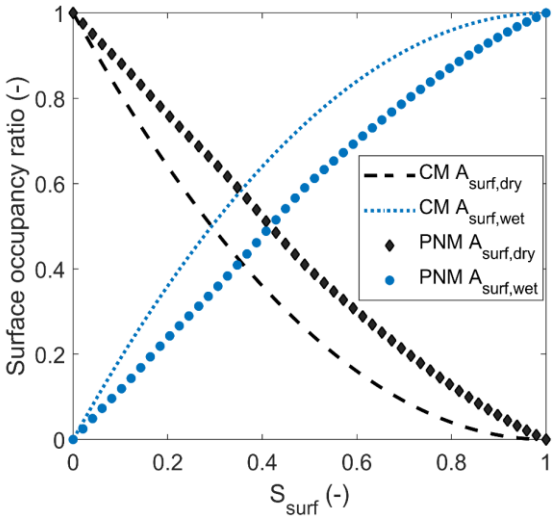

Fig. 4.4: Comparison between PNM data and CM profiles for surface occupancy ratio of liquid phase as a function of surface saturation S_{surf}. The CM profiles are based on Eq. (4.19) and $A_{surf,wet} = 1 - A_{surf,dry}$.

4.3 CM solution compared with PNM simulation results

In this Chapter, we aim to compare the solution of the two-equation NLE CM with the PNM simulations that have been presented in Attari Moghaddam et al. (2017). For the sake of completeness, we describe briefly the physical and structural parameters used for the PNM simulations in Attari Moghaddam et al. (2017). In order to minimize the influence of randomness in throat size distribution, the PNM results were averaged over 15 simulations, each with different realization of throat size distribution. The structural and physical parameters for these simulations are presented in Table 1. The

wetting angle between the liquid and solid phase is assumed to be zero. Due to the small size of the network, an unrealistically high value of liquid viscosity was chosen such that the viscous dissipation characteristic length (see e.g., Lehmann et al., 2008) is smaller than the total height of the network. This means that the thickness of two-phase zone is restricted over sufficiently long period of drying leading to a viscous-capillary drying regime with an initial capillary number of 0.014 (based on the definition in Metzger et al., 2007).

Structural property	**Unit**	**Value**	**Physical constant**	**Unit**	**Value**
Network size (nodes)	-	25×25×51	Temperature	K	293.15
Boundary layer discretization	-	25×25×10	Pressure	Pa	10^5
Mean throat radius	mm	0.25	Liquid kinematic viscosity	m^2/s	0.028
Standard deviation of throat radius	mm	0.025	Saturation vapor pressure	Pa	2339
Throat length	mm	1	Surface tension	N/m	0.07274
Network porosity	-	0.594	Diffusion coefficient	m^2/s	2.56×10^{-5}

Table 1: Structural and physical parameters for PNM simulations.

The effective vapor diffusivity D_{eff}, the specific interfacial area a_{gl}, the liquid phase diffusivity D_l and the fraction of surface dry pores $A_{surf,dry}$ as presented respectively in Figs. 4.1, 4.2, 4.3 and 4.4 are used to solve the two-equation CM (Eqs. (4.7) and (4.8)). Apart from these, the mass exchange coefficient k, which is used as a fitting coefficient, is also needed. The mass exchange coefficient k is a function of network geometry, the value of diffusion coefficient in the gas phase and possibly some other factors (Pujol et al., 2011). For example, for our case, the mass exchange coefficient can be estimated roughly by taking the ratio of pore scale binary diffusion coefficient and the characteristic length of the local averaging volume. This comes out to be roughly of the order of 2.5×10^{-2} m/s. For the results presented in this section, the value of k is 5×10^{-2} m/s, which is the same as that used in Ahmad et al. (2020) for the case of drying

of a partially saturated medium with NLE effects, see Chapter 3. The solution of two-equation CM is gauged on the basis of kinetics, phase distribution profiles and NLE effect. Initially, the saturation of the whole CM domain is unity and the respective initial vapor pressure corresponds to the saturation vapor pressure. The computational domain for the CM solution is discretized into 500 finite volume elements and it is found that the CM solution does not vary upon further refinement in the discretization.

Figure 4.5 shows the variation of network saturation and normalized evaporation rate with drying time obtained from CM solution compared with that computed from PNM simulations. The results indicate that the solution of CM reproduces reasonably the drying kinetics. Apart from these, we also analyze the reproducibility of phase distribution by the CM solution through saturation and vapor pressure profiles. Figure 4.6 shows that the CM solution reproduces the saturation profiles and vapor pressure profiles satisfactorily throughout the drying process.

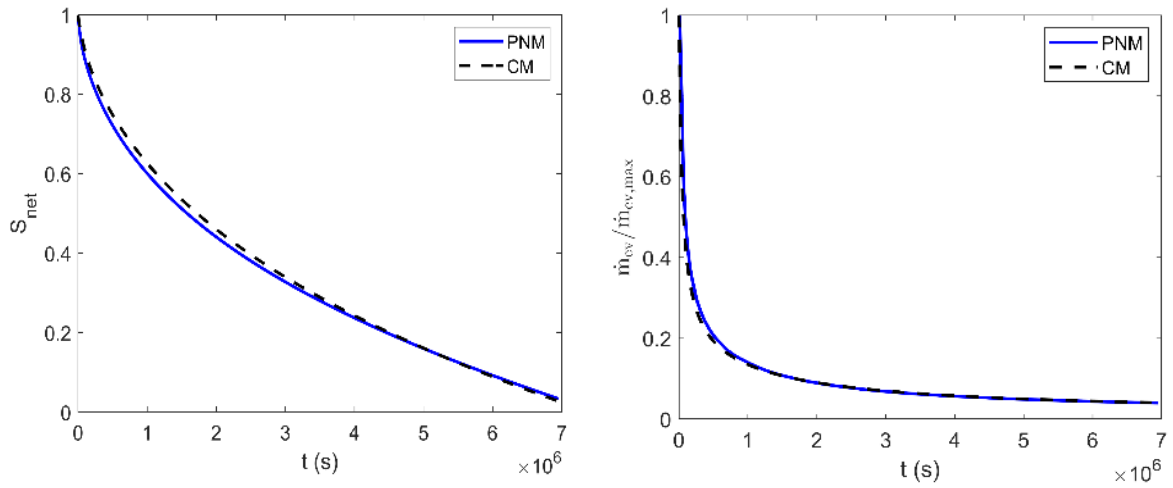

Fig. 4.5: Variation of overall network saturation S_{net} with drying time (left) and normalized evaporation rate with respect to drying time (right). The black dashed line represents the solution of CM, whereas the blue solid line represents the profile obtained from PNM simulation results.

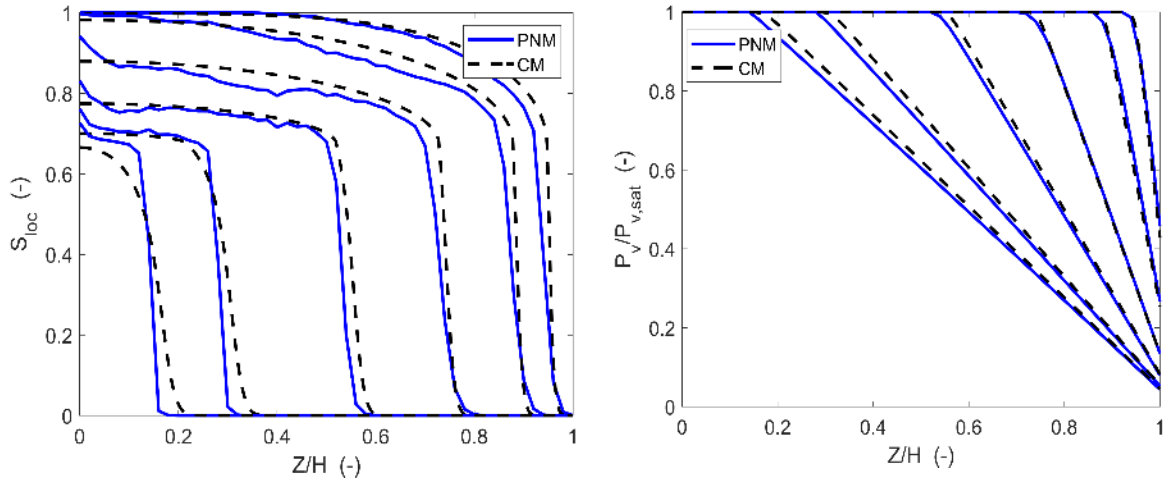

Fig. 4.6: Saturation profiles (left) and normalized vapor pressure profiles (right) obtained from two-equation CM solution and PNM simulations. The results are plotted for times that correspond to S_{net} of 0.90, 0.80, 0.60, 0.40, 0.20 and 0.10 for PNM simulation results. The outer surface lies at z/H = 1, where *H* is the network height.

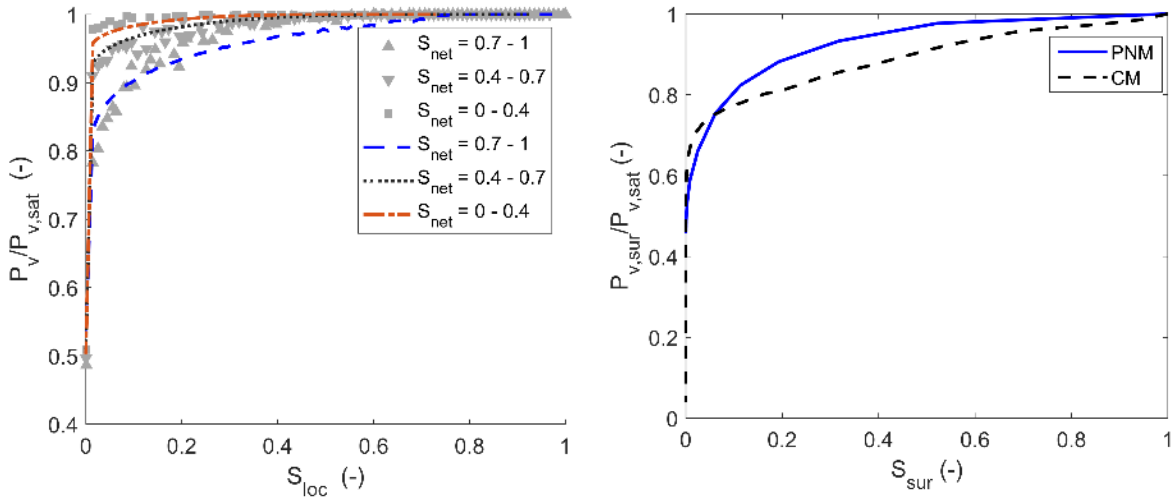

Fig. 4.7. Left: NLE effect obtained from PNM drying simulations and solution of two-equation NLE CM for varying ranges of S_{net}. The lines and grey symbols represent CM solution and PNM data, respectively. Right: NLE function at the surface obtained from PNM drying simulations and that predicted by two-equation CM.

Apart from analyzing the kinetics and phase distribution profiles, we also compare the ability of CM to reproduce the NLE effect. This is presented in Fig. 4.7 for the whole network as well as specifically for the evaporative surface. For ease of

comparison, the NLE effect for the whole network is compared with respect to different ranges of network saturation values. The results presented in Fig. 4.7 show that the CM solution reproduces satisfactorily the NLE at the surface as well as inside the whole network.

The evolution of network saturation, normalized evaporation rate, saturation profiles, vapor pressure profiles and the NLE effect (Figs. 4.5, 4.6 and 4.7, respectively) show that the two-equation CM reproduces the PNM simulation results reasonably well.

4.4 Sensitivity study

4.4.1 On the mass exchange coefficient

The mass exchange coefficient k allows control over the local phase change kinetics. An increase in the value of k implies that we approach the situation of local equilibrium where the variation in the local partial vapor pressure becomes negligible, whereas a decrease in the value of k implies that we have a local non-equilibrium situation where the variations in the local partial vapor pressure become significant. In terms of the liquid saturation profiles, this means that as the value of k increases the drying front becomes sharper (thinner), whereas as the value of k decreases, the drying front becomes smoother. A smoother and more continuous drying front allows for a better numerical convergence and as k becomes larger, the numerical convergence becomes more difficult due to the sharper drying front, which leads to larger computational times for the CM solution. Based on tests, we found that for our given set of parameters, the CM becomes unstable, i.e. numerical convergence problems arise, for values outside the range $[10^{-3} - 10]$ m/s. We present in Fig. 4.8 the influence of the value of k on the evolution of network saturation and local saturation profiles with drying time.

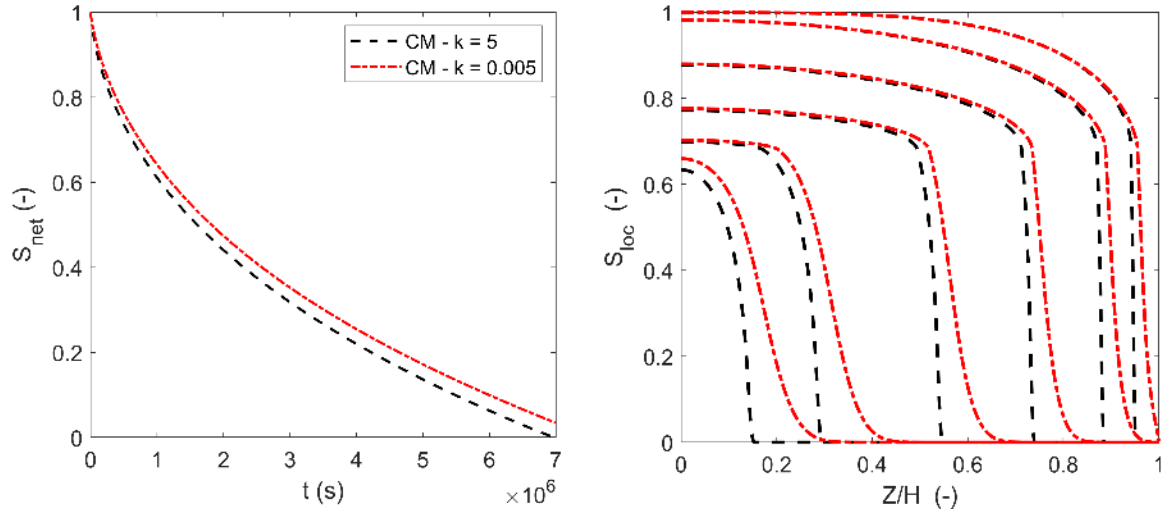

Fig. 4.8: Comparison of evolution of network saturation and saturation profiles with drying time for different values of mass exchange coefficient, k i.e. for 5 and 0.005 m/s. The legend on the figure on the left is valid for both figures. The saturation profiles on the right are plotted for six different instants in time.

We observe that for $k = 5$ m/s, the drying front is sharper, i.e. the saturation profiles are more discontinuous, whereas they are smoother and more continuous for $k = 0.005$ m/s. This is because of the fact that for $k = 5$ m/s we approach the situation of local equilibrium and the NLE effect is reduced significantly (e.g. the NLE effect at the surface where partial vapor pressure stays close to saturation vapor pressure, see Fig. 4.9) and therefore, the drying rate is higher for $k = 5$ m/s as compared to $k = 0.005$ m/s. Interestingly, the saturation profiles give the impression that the drying rate would be higher for situations where the drying front position is closer to the boundary layer. However, the extent of NLE effect is such that it overcomes the advantage provided by the less advanced position of the drying front. This comparison is analogous to comparisons between the so called traveling front model (LE CM) and NLE CM solutions (see e.g., Ahmad et al., 2020) where the drying front position reproduced by the LE CM recedes faster as compared to the NLE CM. The sharp and irregular decrease in the surface NLE function for $k = 0.005$ m/s, illustrated in Fig. 4.9, is due to numerical convergence issues which become more significant for k values smaller than 1×10^{-3} m/s.

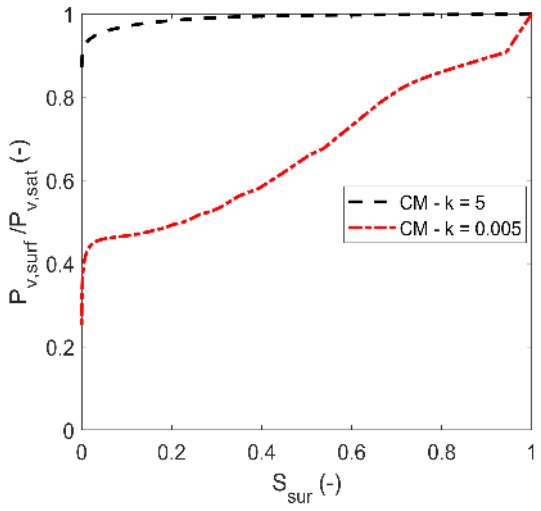

Fig. 4.9: Comparison of NLE effect at the surface for k values of 5 and 0.005 m/s.

4.4.2 On the liquid phase diffusivity

To analyze the influence of macroscopic liquid phase diffusivity on the drying behavior, we test two cases by varying the liquid diffusivity presented in Sec. 4.2.1, which we refer to as $D_{l,ref}$. The rest of the CM parameters are the same as the CM parameters described in Sec. 4.2. In Fig. 4.10, we present the network saturation variation and saturation profiles based on $D_l = 0.5D_{l,ref}$ and $D_l = 2D_{l,ref}$.

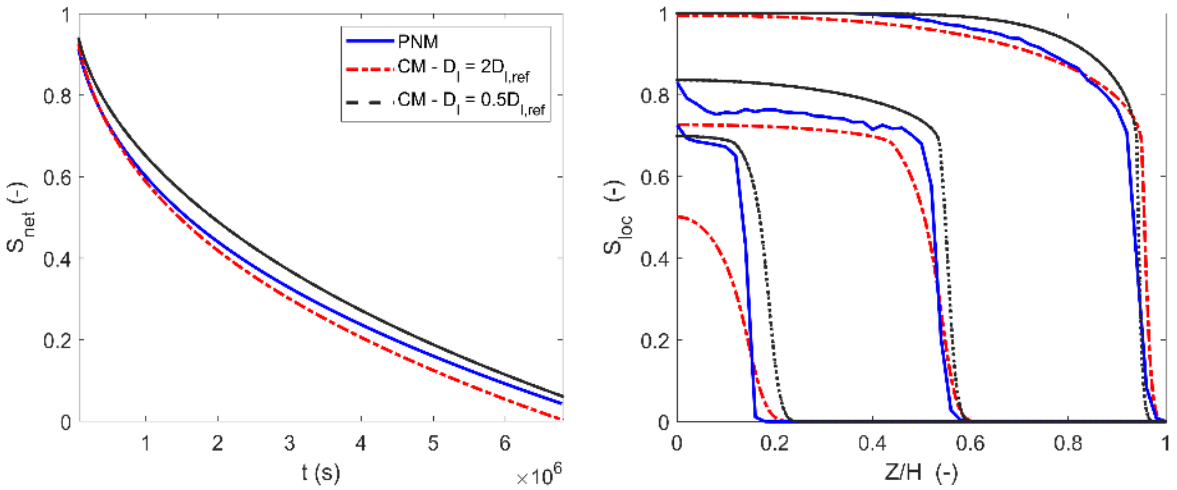

Fig. 4.10: Influence of D_l on evolution of network saturation and local saturation profiles with respect to drying time for three distinct times based on $2D_{l,ref}$ and $0.5D_{l,ref}$, where $D_{l,ref}$ is based on Eqs. (4.14) and (4.15) shown in Sect. 4.2.1. The legend on the figure on the left applies to the figure on the right as well. The saturation profiles on the right are plotted for times that correspond to S_{net} of 0.90, 0.40 and 0.10 for PNM simulation results. The evaporative surface lies at Z/H equal to 1.

As expected, drying becomes faster when liquid phase diffusivity is larger (see the variation of network saturation with respect to time presented in Fig. 4.10). This is because the capillary transport from slices deep in the network towards the drying front is enhanced. As a result, the drying front recedes relatively slower. This can also be observed from the saturation profiles corresponding to S_{net} of approximately 0.9 in Fig. 4.10, where the drying front corresponding to $D_l = 2D_{l,ref}$ lies closer to the boundary layer (around $Z/H = 1$) as compared to $D_l = 0.5D_{l,ref}$, even though the saturation of the slices deep in the network is lower for $D_l = 2D_{l,ref}$.

4.4.3 On the effective vapor phase diffusivity

Similar to the study of influence of macroscopic liquid diffusivity on drying behavior, we investigate the influence of effective vapor diffusivity with the help of two test cases based on $D^*_{eff} = 0.8D^*_{eff,ref}$ and $D^*_{eff} = 1.2D^*_{eff,ref}$, while the rest of the parameters are the same as the CM parameters described in Sec. 4.2. $D^*_{eff,ref}$ is the effective vapor diffusivity given in Sec. 4.2.2.

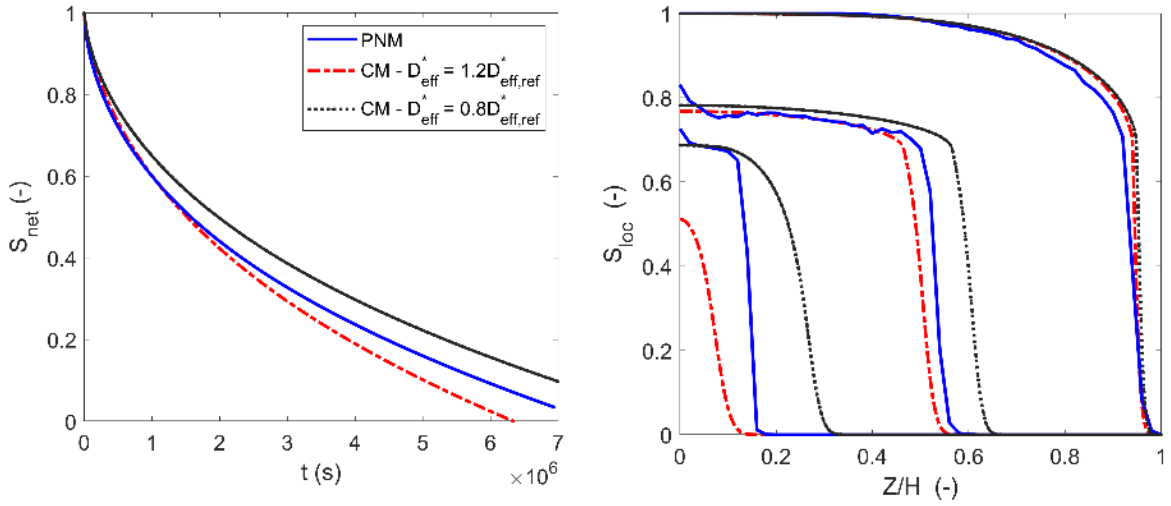

Fig. 4.11: Comparison of influence of effective vapor diffusivity on evolution of network saturation and saturation profiles based on D^*_{eff} corresponding to $0.8D^*_{eff,ref}$ and $1.2D^*_{eff}$. The legend on the figure on the left applies to the figure on the right as well. The saturation profiles on the right are plotted for times that correspond to S_{net} of 0.90, 0.40 and 0.10 for PNM simulation results.

The CM is very sensitive to the value of D^*_{eff}, therefore we vary it only by a fraction of 0.2 (Fig. 4.11). As expected, the saturation profile corresponding to network saturation of 0.9 does not show any impact to the change in D^*_{eff}. This is because as long as the network surface is saturated there is no impact of D^*_{eff} on the drying behavior, because the drying process is dictated by the vapor transport in the boundary layer, and effective vapor diffusivity caters for the vapor transport within the porous medium. As expected, D^*_{eff} influences the drying kinetics and drying becomes faster for larger values of D^*_{eff} as the resistance to vapor diffusion inside the porous medium decreases.

4.4.4 On the specific interfacial area

For the description of the drying process at the macroscopic scale, we not only need the local and network saturation but also the distribution of saturation inside the medium (Nowicki et al., 1992). The specific interfacial area which is a macroscopic parameter in the source/sink term of our NLE CM formulation provides a measure of the distribution of liquid inside the network. Since a_{gl} is a multiplier of mass exchange coefficient k in our CM formulation, we can estimate the influence of a_{gl} on the CM solution through the study of variation in k as presented in Sec. 4.4.1. This implies that, keeping all other factors constant, if the overall magnitude of a_{gl} increases, it would result in sharper drying front and a smaller NLE effect. Similarly, an overall decrease in magnitude of a_{gl} would result in a smoother drying front with a more pronounced NLE effect. A higher local specific interfacial area implies a more uniform local liquid phase distribution, i.e. a more fragmented liquid phase. This is correlated with a smaller NLE effect due to increase in tortuosity resulting in increased resistance to the local vapor transport. Similarly, a lower specific interfacial area implies a lower tortuosity resulting in a more pronounced NLE effect.

In Sec. 4.3, we presented a CM solution based on non-linear profile for $A_{surf,dry}$, i.e. for $A_{surf,dry} = \left(1 - S_{surf}\right)^2$. Here, we discuss briefly the impact of linear relationship between $A_{surf,dry}$ and S_{surf} on the CM solution. As illustrated in Fig. 4.12, the vapor partial pressure at the surface for linear profile of $A_{surf,dry}$ shows a sharp drop initially as the drying begins. However, this drop does not affect the CM solution (as it occurs

for a relatively minute period, after which the partial vapor pressure at the surface corresponds roughly to that reproduced by the non-linear relationship between $A_{surf,dry}$ and S_{surf}. The selection of non-linear function for $A_{surf,dry}$ results in a better reciprocation of the NLE effect at the surface. The phase distribution and drying kinetics for linear and non-linear profile for $A_{surf,dry}$ (not shown here as the difference in them is not visible) are essentially the same. We observe that the impact of selection of the profile for $A_{surf,dry}$ (linear vs non-linear function) on the CM solution is essentially limited to the NLE function at the surface.

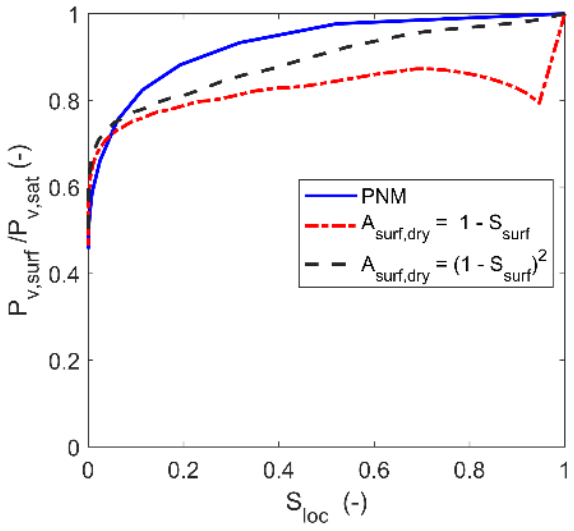

Fig. 4.12: Comparison of NLE effect at the surface based on linear and non-linear profiles for $A_{surf,dry}$ for k = 0.05 m/s.

4.5 The problem of length scale separation and the modeling of thin systems

As mentioned earlier, the size of the PNM is too short for imposing a good length scale separation. Similar to that in Attari Moghaddam et al. (2017), a still better agreement between the PNM results and the CM could be obtained by considering the macroscopic transport parameters such as the liquid and effective vapor diffusivities as functions of both the local saturation and the network (overall) saturation. As demonstrated in Attari Moghaddam et al. (2017), such an approach is an interesting way for taking into account the impact of the poor length scale separation and

modeling the drying process in thin systems using CMs. However, this double saturation approach lacks a theoretical basis and was developed essentially from a heuristic/empirical standpoint. In this thesis, the motivation was not the study of thin systems but the modeling of drying in classical porous media where the length scale separation is met. Because of the poor length separation, the PNM results were considered as simply providing guidance about the macroscopic parameters behavior. The latter were then freely modified, compared to the ones directly deduced from the PNM simulations, so as to obtain eventually a reasonable agreement between the PNM drying results and the CM ones. In doing so, it is our belief that the relevance of the two equation NLE CM could be established in spite of the poor length separation in the PNM simulations. Nevertheless, it would be certainly more convincing to perform PNM simulations over much larger network sizes that fulfil the criterion of length scale separation. However, this is not possible with the present version of our PNM code.

4.6 Remarks

In this work, a two-equation continuum model (CM) of drying aimed at capturing the non-local equilibrium (NLE) effect, for a porous medium fully saturated in the beginning of drying, was developed and the results were compared with pore network simulations. This CM is an extension of our previously developed CM (Ahmad et al., 2020; Chapter 3), which was valid for the limiting case of immobile liquid in a partially saturated porous medium. We approached the problem of mass transport at the surface by employing a closure relationship for the mass transfer at the surface based on the degree of occupancy of the surface pores. This allows predicting the NLE effect at the surface with a reasonable degree of accuracy. Also, it is conceptually more consistent with the drying PNM simulations as compared to the conventionally used continuum modeling approaches, e.g., Schlünder's model that does not consider the influence of dry surface pores on the surface evaporation dynamics (Attari Moghaddam et al., 2018; Haghighi et al., 2013; Lehmann et al., 2013; Schlünder, 1988; Talbi et al., 2019).

The NLE two-equation CM formulation is physically more consistent than the previously developed one-equation CM (Attari Moghaddam et al., 2017b), since it avoids using a NLE surface function relating the vapor partial pressure and the surface saturation as input parameter for the CM model. On the contrary, this function is an output of the model. Indeed, the results indicate that the newly developed two-equation CM reproduces independently the PNM simulation results, i.e. the drying kinetics, phase distribution profiles and the NLE effect with a reasonable degree of accuracy.

The sensitivity study of the macroscopic parameters provided useful insights into the process dynamics. We observed that the mass exchange coefficient has a significant impact on the local equilibrium dynamics. For higher values of the mass exchange coefficient, the CM approaches the LE situation where the drying front is sharper and more discontinuous. For lower values of mass exchange coefficient, the NLE effect becomes more significant and the drying front becomes smoother. As for other transport processes in porous media, it would be interesting to develop, via an upscaling procedure, the closure problem allowing to compute the mass exchange coefficient from digital images of microstructures.

In this chapter, we validated the NLE CM against PNM simulations. It would be interesting to test this model against experimental data. Also, a recurrent problem in the modeling of drying process is the possible impact of liquid films (Prat, 2007; Yiotis et al., 2012; Yiotis et al., 2004) and other secondary capillary structures such as liquid rings and bridges (Kharaghani et al., 2021; Vorhauer et al., 2015) that can be present in the pore space after the displacement of bulk menisci. These secondary capillary structures were not considered in the proposed CM model, nor in the PNM simulations. This would represent an interesting extension of the present model.

Chapter 5

Continuum model of drying with dissolved solute transport

This chapter is partly taken from "Ahmad, F., Rahimi, A., Tsotsas, E., Prat, M., Kharaghani, A.: From micro-scale to macro-scale modeling of solute transport in drying capillary porous media. Int. J. Heat Mass Transf. 165, 120722 (2021)".

As mentioned in Chapter 1, the drying of capillary porous media saturated with saline solution is an important process as it has several environmental and industrial applications. In this chapter, we aim to assess and evaluate the commonly used model based on the classical macroscopic advective-diffusive equation (ADE) (Guglielmini et al., 2008; Huinink et al., 2002; Sghaier et al., 2007). Similar to that of the previous chapters, we use pore network model (PNM) simulations as a benchmark. Recently, comprehensive pore network models for the drying-induced solute transport inside porous media have been presented (Dashtian et al., 2018; Rahimi, 2019). In this manuscript, we employ a 3D PNM which is based on Rahimi, (2019).

We focus on the capillary-dominated regime in a homogeneous porous medium. This is a regime frequently observed in laboratory experiments (e.g. Coussot, 2000; Eloukabi et al., 2013; Faiyas et al., 2017; Gupta et al., 2014; Pel et al., 2002). In this study, we focus on the CRP, which is also a period in which the liquid phase in the porous medium is connected to the porous medium evaporative surface. As reported in several previous works (e.g. Eloukabi et al., 2013; Lazhar et al., 2020; Shokri-Kuehni et

al., 2018; Shokri, 2014), salt crystallization is frequently observed at the porous medium surface during the CRP. This is fully consistent with the semi-analytical or numerical solutions of the commonly used ADE (Guglielmini et al., 2008; Huinink et al., 2002; Sghaier et al., 2007), which predict that the locus of the maximum solute concentration is at the drying surface. Since crystallization occurs when the solution concentration reaches a critical value, the most likely place of crystallization is the surface. As reported in Eloukabi et al. (2013), the crystallization process at the surface and the subsequent development of a salt crust on top of the porous medium (a classical situation where the evaporative surface is on top of the porous sample is assumed) can have a severe impact on the evaporation rate. In this chapter, we focus on the situation prior to the crystallization, i.e. on the solute distribution before the onset of crystallization.

Also, the influence of the solute concentration on the properties of the fluid is neglected in this study for simplicity. In this respect, the important feature is to impose the same fluid properties for the PNM simulations and the CM. Based on this, the value of initial solute concentration can be arbitrarily chosen and its influence on other parameters is not investigated in this work. Since the contact angle of a saline aqueous solution is relatively high, the development of liquid films is not favored (Sghaier et al., 2006). For this reason, liquid films are assumed to be negligible in this study.

5.1 Continuum model for drying with dissolved solute transport

As exemplified in, for instance, Guglielmini et al. (2008), Huinink et al. (2002), Sghaier et al. (2007), the continuum drying model in the presence of solute aims at predicting the evaporation rate, the liquid distribution, i.e. the saturation profiles, and the solute concentration distribution within the sample. While the corresponding model generally requires a numerical solution (Diouf et al., 2018; Hidri et al., 2013) for both the evolution of the saturation and the solute concentration, a much simpler approach is possible when only the CRP in the capillary regime is considered in the classical configuration where a homogeneous porous medium is limited by impervious walls at the bottom surface and along the lateral sides with evaporation only at the top surface. First, the evaporation flux j is constant in the CRP and therefore just an input.

Second, the fact that the saturation, S, is spatially uniform can be exploited (Huinink et al., 2002) to obtain its evolution as,

$$S = 1 - \frac{j}{\rho_l H \varepsilon}, \tag{5.1}$$

where ρ_l is the liquid mass density, ε the porosity and H is the height of the porous sample. The advective-diffusive equation classically used for modeling the solute transport during the drying process in the considered 1D macroscopic configuration reads (Sghaier et al., 2007)

$$\frac{\partial \rho_l \varepsilon S C}{\partial t} + \frac{\partial}{\partial z}(\rho_l \varepsilon U S C) = \frac{\partial}{\partial z}\left(\rho_l \varepsilon S D_s^* \frac{\partial C}{\partial z}\right), \tag{5.2}$$

where C is the solute concentration, z is the vertical spatial coordinate, U is the average liquid velocity, also referred to as the interstitial velocity, and D_s^* is the effective solute diffusion coefficient. The boundary condition needed to solve Eq. (5.2) is expressed by zero flux at both boundaries (top evaporative surface and the boundary on the opposite end of the surface) of the 1D domain expressed as

$$\rho_l \varepsilon U S C - \rho_l \varepsilon S D_s^* \frac{\partial C}{\partial z} = 0. \tag{5.3}$$

The effective solute diffusivity D_s^* is a function of liquid saturation S. The respective function is expressed using the classical formulation (Huinink et al., 2003; Moldrup et al., 2001), which depends on the pore-scale solute diffusivity, porosity and saturation percolation threshold S_c,

$$D_s^* = \frac{S - S_c}{1 - S_c} D_s^*(1), \tag{5.4}$$

where $D_s^*(1)$ is the value of effective solute diffusivity for fully saturated region, i.e., when S = 1. It is generally expressed as a function of porosity and tortuosity of the porous medium and pore-scale solute diffusion coefficient D_s. Since $D_s^*(1)$ depends on the microstructure of the considered porous medium, it needs to be determined for our particular porous medium, i.e. our pore network model. This is performed in Sec. 5.3.1. The value of D_s is considered as 1×10^{-9} m^2/s which is close to that of the common salts such as sodium chloride.

Like the saturation, the velocity field $U(z)$ in Eq. (5.2) can also be obtained analytically (Huinink et al., 2002) as

$$U = \frac{j}{\varepsilon \rho_l S}\left(\frac{z}{H}\right), \tag{5.5}$$

where z = 0 is at the porous domain bottom and $z = H$ at the evaporative surface. Equation (5.2) is solved numerically with MATLAB using the analytical solutions according to Eqs. (5.1) and (5.5) for the evolution of saturation and velocity.

5.2 PNM simulations

The three-dimensional PNM simulations are carried out on a network that consists of 25 computational nodes in each spatial direction. The pore size distribution is characterized by a mean throat radius of 250 µm with a standard deviation of 25 µm and a uniform throat length of 1 mm. The network porosity is 0.59 and drying occurs at room temperature and pressure. The average total drying flux j (which stays nearly constant with time as our study is limited to CRP) in the PNM and CM simulations is 3.025×10^{-6} kg/m^2/s. The competition between the advective and diffusive solute transport is characterized by the Péclet number defined as $Pe = \frac{jL_{ch}}{\varepsilon \rho_l D_s^*}$. The initial Péclet number is computed by using the total network height as the characteristic length L_{ch} and the initial effective solute diffusivity $D_s^*(1)$. In the simulations, $Pe = 0.2$ at the beginning of drying. This is relatively small but sufficient to have a noticeable advection effect. The advective transport becomes more dominant with time because the effective solute diffusivity decreases with the decrease in saturation.

As performed in Chapters 3 and 4, the macroscopic variables in the CM with dissolved solute transport are interpreted within the framework of the volume averaging method (Whitaker, 1977), where the macroscopic variables are expressed as volume averages of the corresponding microscopic variables over a representative averaging volume. For the comparison of the PNM results with the CM solution, the data obtained from PNM simulations are therefore transformed into macroscopic data by volume averaging. Hence, the three-dimensional PNM domain is vertically split into local averaging volumes or slices where each slice consists of vertical throats and their

bottom side neighbor horizontal throats. However, in this chapter, for the slice averaging method, a more simplified approach is followed. The configuration of all the slices in the network is the same, as opposed to that in Chapter 3 and 4 where the configuration of the surface slice is different from the rest of the network (see Fig. 3.2, where a slice of thickness Δz is indicated). We adopt a simpler approach in this chapter because here we only operate in CRP where the drying rate is fixed, eliminating the need to compare the kinetics (and hence, the consideration of macroscopic partial vapor pressure) in the comparison of CM solution with PNM.

As mentioned in Sec. 2.3 where the PNM for dissolved solute transport is described, we consider the pores as volume-less computational nodes. This assumption leads to an overestimation of the porous medium porosity (through the overlap region of all neighboring throats at each pore). However, as we consider the capillary dominated regime, the consideration of pore body volume does not impact the liquid fragmentation dynamics because based on the geometric constraints, the radius of the pore body is always larger or equal to its neighbor throat radii. This means that the invasion percolation dynamics is the same in PNM with and without pore body volumes. As the liquid fragmentation dynamics is not affected, the use of PNM without the pore body volume can be considered to be adequate in the capillary dominated regime. On the other hand, considering the pore body volumes can lead to lower irreducible saturation and a longer CRP if the mean throat radius is sufficiently high (see, e.g., Lu et al., 2020). Also, the mixing process taking place in the pores might depend on the pore body volume. Perfect mixing, i.e. a uniform solute concentration, is assumed in the pore bodies in our model. Although, we do not believe that the consideration of a pore network with pore body volumes would change the main conclusions of the present work, this aspect would deserve further investigations.

We perform multiple PNM simulations with different realizations of throat size distribution. Though the network saturation at the end of CRP may vary among simulations, it can be reliably considered that the CRP lasts in fact down to a network saturation of 0.7. Hence, in the CM simulations, the analysis is limited to a network saturation of 0.7. We have considered an arbitrarily chosen value of 10 kg/m^3 as the

initial solute concentration for all simulations in this work. In the capillary-dominated regime, the depletion of liquid from the network occurs such that the continuity of the liquid phase decreases as the initially connected bulk liquid phase is split into clusters and isolated single throats (Le Bray et al., 1999). At any instant during the drying process, the largest liquid cluster with respect to volume is characterized as the main cluster. All other liquid clusters are characterized as isolated clusters, because they are isolated from each other and more importantly from the main cluster which spans over the entire network height. Each isolated liquid cluster eventually breaks down to several single isolated liquid throats which are the smallest structural element of the liquid phase. This increasing discontinuity of the liquid phase directly influences the solute transport because solute transport can only occur between the connected liquid phase elements (as liquid films are not considered). Hence, it is important to represent the solute concentration with respect to the liquid phase elements, i.e. the main cluster, the isolated clusters and isolated single throats. In Fig. 5.1 we present the instantaneous mapping of the solute concentration for a 2D pore network of 100×100. The solute concentration gradient in the main cluster can be seen in Fig. 5.1a. The progressive fragmentation of the liquid phase from the main cluster into isolated clusters is also shown in the cut-outs in Figs. 5.1b-d, where the solute concentration increase that develops as a result of shrinking and further fragmentation of an isolated cluster can be clearly observed.

In Fig. 5.2 we present the instantaneous local solute concentration profiles and the corresponding saturation profiles for regular intervals of network saturation ranging between 0.9 and 0.7. The profiles are obtained using the slice averaging method. For the sake of simplicity, the isolated single throats are considered together with isolated clusters as part of the isolated liquid phase. The total liquid phase saturation in a slice is computed as

$$S = \frac{\sum_{i=1}^{i=n} S_{ti} V_{ti}}{\sum_{i=1}^{i=n} V_{ti}}, \tag{5.6}$$

where n is the number of throats in the slice, S_{ti} is the saturation in throat i (S_{ti} = 1 if the throat is fully filled with liquid, S_{ti} = 0 when the throat is empty), V_{ti} is the volume of throat i. Similarly, the main cluster saturation is computed as

$$S_{mc} = \frac{\sum_{i=1}^{i=n_{mc}} S_{ti} V_{ti}}{\sum_{i=1}^{i=n} V_{ti}}, \tag{5.7}$$

where n_{mc} is the number of throats of the main cluster in the considered slice. The isolated cluster saturation can be simply computed as $S_{ic} = S - S_{mc}$. The slice averaged solute concentration $\langle C \rangle$ in the total liquid is computed as

$$\langle C \rangle = \frac{\sum_{i=1}^{i=n} C_i S_{ti} V_{ti}}{\sum_{i=1}^{i=n} V_{ti}}. \tag{5.8}$$

The slice averaged concentration in the main cluster $\langle C \rangle_{mc}$ is computed as

$$\langle C \rangle_{mc} = \frac{\sum_{i=1}^{i=n_{mc}} C_i S_{ti} V_{ti}}{\sum_{i=1}^{i=n_{mc}} V_{ti}}. \tag{5.9}$$

While the slice averaged solute concentration in isolated clusters $\langle C \rangle_{ic}$ is computed as

$$\langle C \rangle_{ic} = \frac{\sum_{i=1}^{i=n_{ic}} C_i S_{ti} V_{ti}}{\sum_{i=1}^{i=n_{ic}} V_{ti}}, \tag{5.10}$$

where n_{ic} refers to the number of throats of isolated clusters in the considered slice. The saturation profiles in Fig. 5.2 reveal that the proportion of liquid in the isolated liquid elements increases for lower network saturations. At the network saturation of 0.7, the proportion of liquid in isolated liquid elements is approximately equal to that in the main cluster except for a few slices furthest away from the evaporative surface. Another important phenomenon is the presence of strong edge effect (Attari Moghaddam et al., 2018; Attari Moghaddam et al., 2017) (a sharp drop in saturation profiles) adjacent to the evaporative surface. A less marked edge effect is also visible in the region adjacent to the bottom surface. The focus being on what happens at the evaporative surface, the edge effect only refers to the vicinity of the evaporative surface in this study. In the early stages of drying, the number of meniscus throats per slice is the highest in the surface slice compared to all other slices in the network, since the network is open to evaporation only from the top. Consequently, it is more likely

that the meniscus with the largest radius is located in the surface slice, leading to higher degree of fragmentation of the liquid phase at the surface. Additionally, the higher evaporation rate at the surface and the lack of liquid compensation by capillary pumping leads to fast shrinking of the isolated clusters and single throats. It must be noted that such an edge effect is not expected to be visible in the saturation profile measurements reported in the literature. In the pore network simulations, the edge effect is typically in a region with a thickness of around 4-5 lattice spacings (the lattice spacing is the distance between two nodes in the network). This is much too small to be detected by the NMR set-ups used to measure the saturation profiles (e.g. Gupta et al., 2014). In addition, the interpretation of the NMR signal is much less obvious in the vicinity of the porous medium surface, where measurement artefacts might affect the saturation measurements. Another important difference in Fig. 5.2 with the experimental profiles (e.g. Gupta et al., 2014; Thiery et al., 2017), is that the PNM profile is not flat for high network overall saturations, i.e. in Fig. 5.2a (S_{net} = 0.90) and Fig. 5.2b (S_{net} = 0.85), whereas the profiles are typically flat for similar global saturations in the experiments (Gupta et al., 2014; Thiery et al., 2017). As discussed in Le Bray et al. (1999), this is a finite size effect due to the network small size. The profiles tend to get flat (except in the region of the edge effect) only after the breakthrough (BT), which is the moment when the gas phase reaches for the first time the porous medium opposite side. As discussed in Wilkinson (1986), the liquid saturation at BT scales as $1 - S_{BT} \propto N^{-0.48}$, where N is the network size (= the number of pores in one spatial direction). In our simulation N = 25 and $S_{BT} \approx 0.9$, whereas in the experiments $N >> 25$ and thus S_{BT} is expected to be very close to 1. Thus, the period before breakthrough is typically not documented in the experimental works and is typically not captured by the CM which predicts a flat saturation profile right from the beginning of the capillary regime. The edge effect is not predicted by the commonly used continuum model either, i.e. Eq. (5.1).

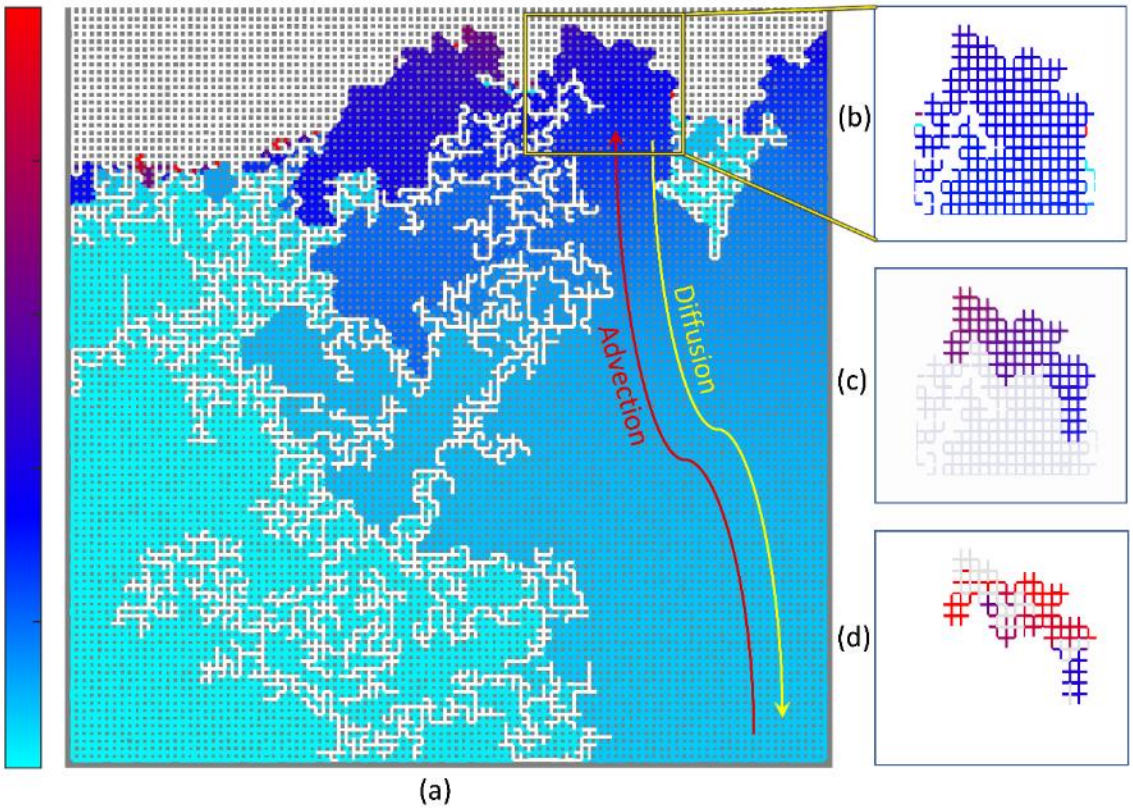

Fig. 5.1: A 2D PNM representation of the instantaneous distribution of solute in main cluster and isolated clusters for a network of 100 × 100 pores. The evaporative surface lies at the top of the network. The gas phase is shown in white in all plots, whereas the solid phase is shown in grey in (a) and in white in (b), (c) and (d). The subplot (b) is a cut-out from (a) and illustrates a section of the main cluster. The subplot (c) represents the splitting of an isolated cluster from its parent main cluster illustrated in (b), whereas (d) indicates the subsequent fragmentation and shrinking of the isolated cluster shown in (c). The color bar on the left indicates the range of solute concentration. Note that results of 3D PNM simulations are presented in the rest of the chapter.

As can be seen from Fig. 5.2, the edge effect in the saturation profiles can be observed in the main cluster as well as in the isolated liquid elements. The instantaneous solute concentration profiles in the main cluster and for the total liquid phase have the typical exponential-like shape resulting from a dominant convective effect (the back-diffusion is not sufficient to spatially equalize the concentration (Huinink et al., 2002)). As discussed in some details in Pel et al. (2018), two main effects contribute to the

concentration build-up in the porous medium top region: the advective transport of the ions toward the surface where they accumulate, and the saturation decrease (the concentration in a shrinking liquid volume necessarily increases). In the main cluster, both effects contribute to the concentration build-up since the main cluster spans the network, but the situation is actually subtler because the change in the main cluster saturation is due to two effects: the loss of water due to evaporation and the fragmentation. Isolated clusters initially form by detachment from the main cluster. The loss of water due to evaporation increases the concentration in the main cluster since again the same amount of salt is contained in a smaller volume of solution. The fragmentation affects only marginally the concentration in the main cluster (i.e. only in the vicinity of the throat whose invasion leads to an isolated cluster detachment). By contrast, the convective accumulation effect is expected to be limited in the isolated liquid clusters since there is no transport over a large distance. It is therefore expected that the change in concentration in the isolated clusters is mostly due to the cluster shrinking effect due to evaporation (as illustrated in Figs. 5.1c and 5.1d). This is consistent with the shape of the isolated cluster concentration profiles in Fig. 5.2. Owing to the so-called screening effect, i.e. the fact that the evaporation rate is very low inside the medium and only significant in the network top region, there is limited change in isolated cluster concentrations away from the top surface. This can also be observed in Fig. 5.1a on the left where the concentration in the isolated clusters that are screened from evaporation is the lowest (as these got fragmented from the main cluster in the early stages of drying and then got screened from evaporation by the main cluster on the right side and the isolated clusters and single liquid throats on the top). The concentration increase in the screened liquid clusters is mainly due to the birth of new isolated clusters with slightly higher concentration from the main cluster.

The abrupt increase in isolated cluster concentration in the network top region in Fig. 5.2 results from a combination of at least two effects. First, this is the evaporation active region. As a result, the isolated clusters shrink (as illustrated in Figs. 5.1c and 5.1d), which again leads to a concentration increase. Second, new isolated clusters are formed from the main cluster with a relatively high concentration (as illustrated in Figs. 5.1b and 5.1c), since the concentration in the main cluster is high in this region.

In this respect, the edge effect contributes to the concentration build-up since the saturation decrease is faster in the top region than elsewhere in the medium. Another interesting aspect lies in the fact that the concentration in the main cluster is slightly higher than the average concentration in the total liquid phase, except in the edge effect region where the main cluster concentration is comparable to or lower than in the total liquid phase. In particular, the concentration maximum at the surface is observed in the isolated clusters. This is a clear indication that the crystallization must start in isolated throats or clusters connected to the surface. However, since the corresponding volume of solution can be small, this does not lead necessarily to a significant crystal development. This point is addressed in more details further in this chapter.

The concentration profiles depicted in Fig. 5.2 are computed as indicated by Eqs. (5.7) to (5.9) and are therefore instantaneous solute concentration profiles. In Attari Moghaddam et al. (2017), it was shown that the spatial average, i.e. the slice averaging, should be combined with a time average to obtain meaningful macroscopic velocity profiles from the PNM velocity field. Thus, the question arises as to whether a similar time-averaging procedure should be combined with the slice averaging procedure as regards the concentrations. We do not think that this is necessary because the instantaneous concentration profiles actually integrate the time-averaging effect on the velocity field, i.e. the evolution of the velocity field in the network as a function of time up to the time the three concentration profiles are computed. Nevertheless, one can argue that the instantaneous profiles can be misleading in situations where the solute concentration in a single isolated throat increases sharply as the result of the liquid mass loss due to evaporation. However, such a single isolated throat with very high solute concentration usually corresponds to little liquid volume that consequently empties rapidly. Hence this instantaneous phenomenon does not result in a sharp fluctuation in the slice concentration. Since the local solute concentration is computed by considering liquid contained in all the throats in a slice, the contribution of the liquid and solute mass in a single throat is not significant. Moreover, the time for evaporation of the single isolated throats is relatively small, hence its influence on the time-averaged solute concentration profile would be small as well.

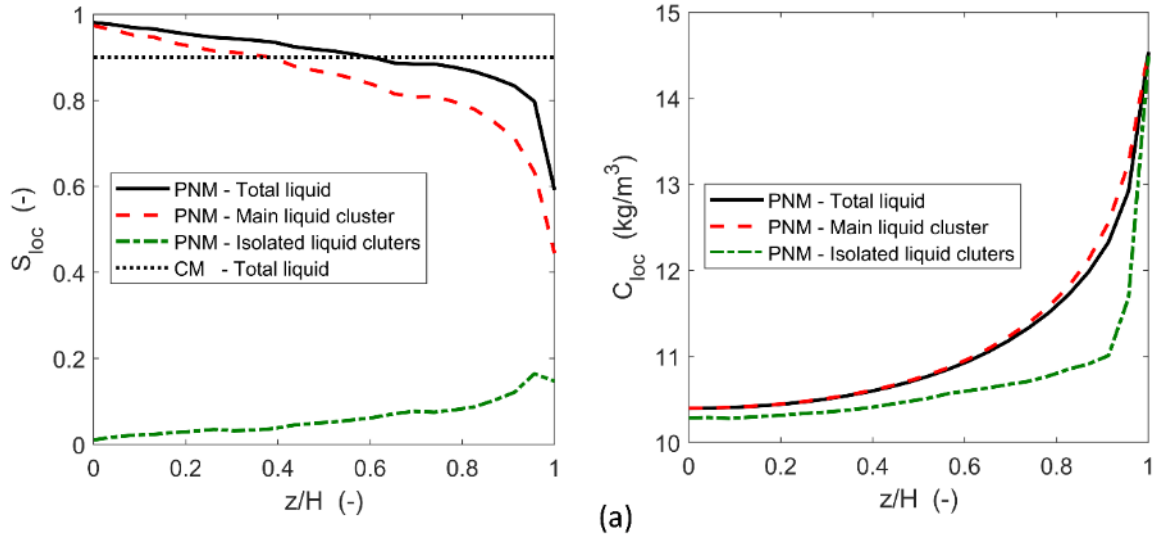
PNM - Total liquid
PNM - Main liquid cluster
PNM - Isolated liquid cluters
CM - Total liquid
S_{loc} (-)
z/H (-)
PNM - Total liquid
PNM - Main liquid cluster
PNM - Isolated liquid cluters
C_{loc} (kg/m^3)
z/H (-)

(a)

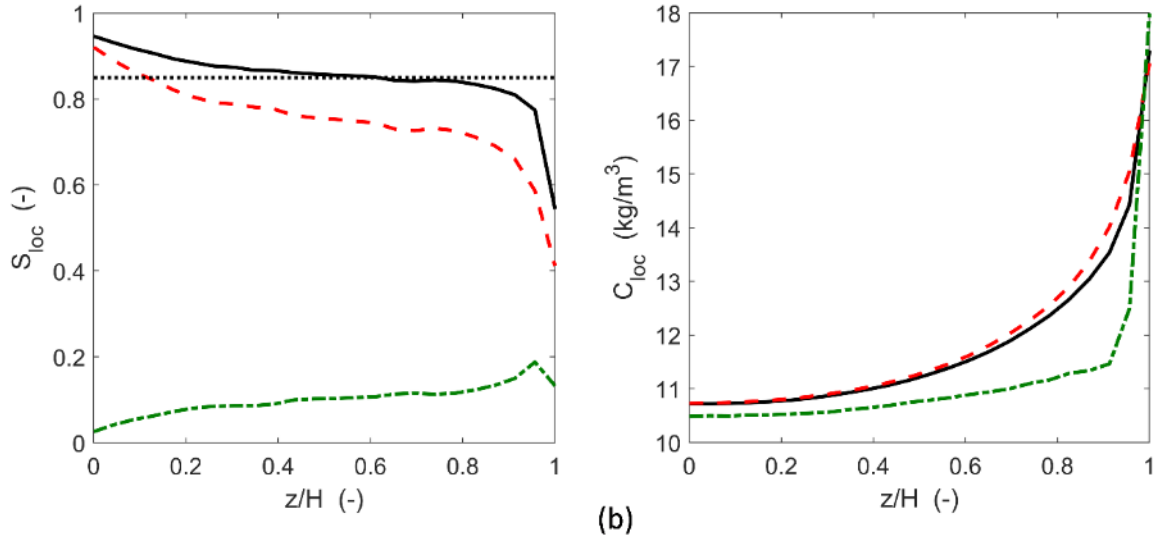
S_{loc} (-)
z/H (-)
C_{loc} (kg/m^3)
z/H (-)

(b)

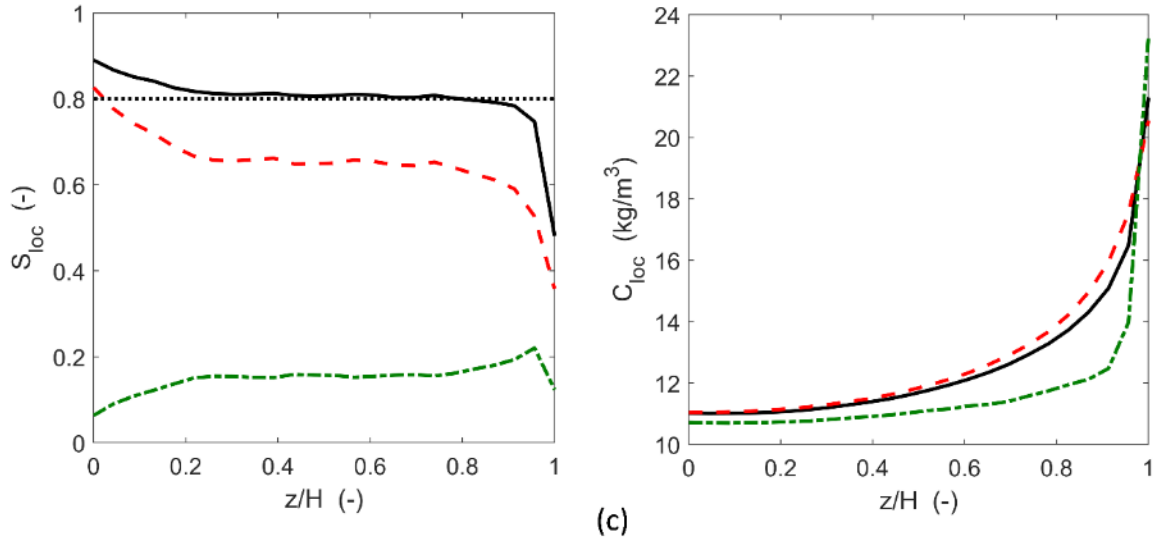
S_{loc} (-)
z/H (-)
C_{loc} (kg/m^3)
z/H (-)

(c)

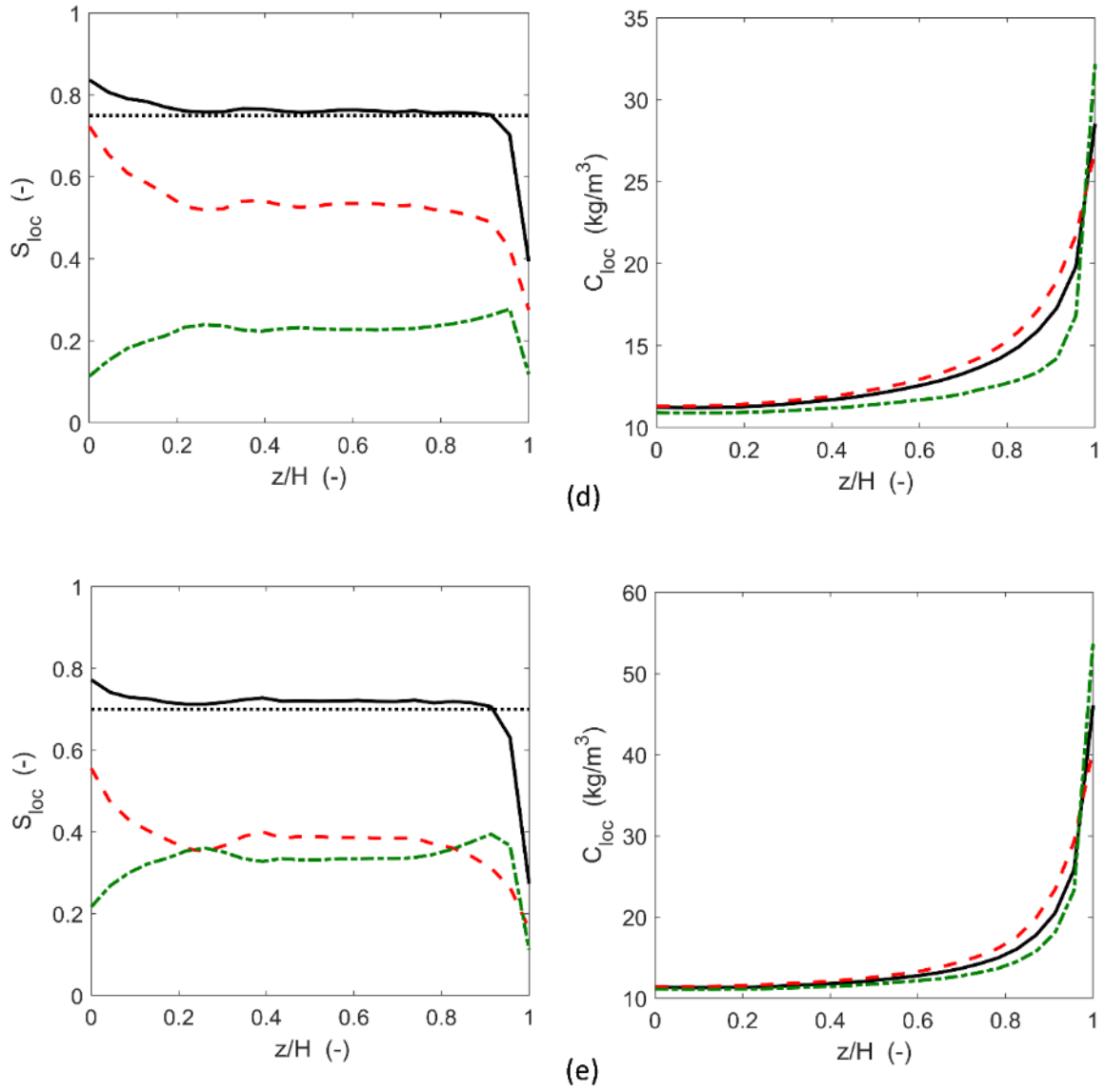

Fig. 5.2: Left: Saturation profiles for main liquid cluster, isolated liquid clusters including single isolated throats, and total liquid. Right: Solute concentration profiles for the respective liquid elements. The legends illustrated in (a) apply to the rest of the rows. Plots in (a) to (e) represent results for network saturation values of 0.90, 0.85, 0.80, 0.75 and 0.70, respectively. The profiles are averaged for data obtained from 15 PNM simulations, each with different realization of throat size distribution.

5.3 Solution of classical CM in comparison with PNM results

The only missing parameter for solving the commonly used CM summarized in Sec. 5.1 is the effective solute diffusion coefficient D_S^*. The method used for computation of this parameter for pore network simulations is explained in this section.

5.3.1 Extraction of effective solute diffusivity from PNM simulations

In this section, we compute the macroscopic solute diffusivity using the volume averaging method described in Sec. 5.2. In PNM simulations, the pore-scale solute diffusivity is fixed; however, similar to the classical CM formulation of effective diffusivity, the effective solute diffusivity computed from PNM simulations is a function of local saturation. Macroscopic solute diffusivity is computed from PNM simulation results based on

$$D_s^*(S) = \frac{j_{s,diff}}{\rho_l \varepsilon S \, \partial C/\partial z}, \tag{5.11}$$

where $j_{s,diff}$, S, $\partial C/\partial z$ denote the macroscopic solute diffusive flux, the slice average saturation and the gradient of the slice average concentration along the spatial coordinate z, respectively. The pore-scale solute diffusive flow rate across a vertical throat k is computed by

$$J_{s,diff,k} = A_k \, D_s \frac{\partial C}{\partial z}, \tag{5.12}$$

where A_k, D_s, and $\frac{\partial C}{\partial z}$ denote the cross-section area of the vertical throat k, the pore-scale solute diffusivity and the pore-scale concentration gradient across throat k, respectively. Using Eq. (5.12), the solute diffusive flow rate across all the vertical throats in a slice is computed and summed up to obtain the macroscopic diffusive flow through the slice. This macroscopic diffusive flow rate is divided by the macroscopic cross-section area of the slice to obtain the macroscopic solute diffusive flux $j_{s,diff}$ which is then used to compute the macroscopic solute diffusivity based on the macroscopic concentration gradient through the slice in consideration (Eq. (5.11)).

As Fig. 5.3 illustrates, the effective solute diffusivity computed from PNM simulation results is nearly a linear function of local saturation, consistently with the usual functional form given by Eq. (5.4). The data points in Fig. 5.3 have been computed by averaging the values of effective solute diffusivity for intervals of slice average saturation equivalent to 0.005. In fact, there are values of effective solute diffusivity

for local saturation smaller than 0.7, because as shown in the saturation profiles of Sec. 5.2, the local saturation is smaller in the region near the evaporative surface as compared to the rest of the network. However, in CM the local saturation is assumed to be uniform in space, hence, at any instant, the network saturation and local saturation are equal. Moreover, as mentioned early in Sec. 5.2, we consider a network saturation of 0.7 as the lower threshold value of CRP. Therefore, in Fig. 5.3, we do not consider values smaller than the threshold value of 0.7.

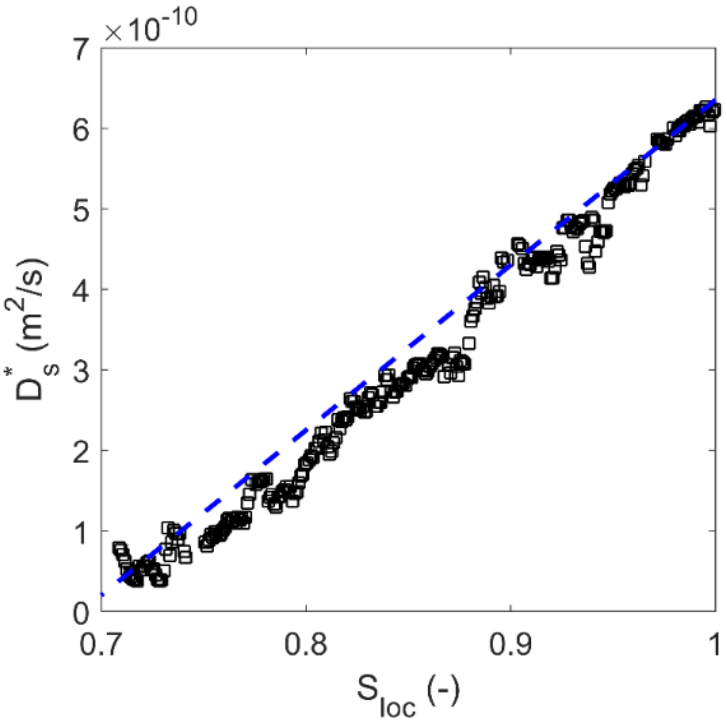

Fig. 5.3: Black square symbols represent the effective diffusivity obtained from PNM simulation results. The dashed blue line indicates fitted profile based on parameter adjustment of the classical formulation of effective diffusivity (Eq. (5.4)).

Figure 5.3 also shows the profile obtained from fitting the parameters using the classical formulation expressed by Eq. (5.3). This fitted profile is based on $D_s^*(1) = \varepsilon^{0.86} D_s$ and S_c = 0.69. As can be seen, Eq. (5.4) is quite well adapted to represent the PNM computed effective diffusion coefficient.

5.3.2 CM solution

In this section, we employ the effective solute diffusivity obtained from PNM simulation results to solve the CM. The solution of CM is compared with the PNM

slice averages in Fig. 5.4. The CM solution complies well with the concentration profiles obtained from PNM simulation results except for the region near the evaporative surface. For the comparison with CM solution, PNM results are considered for the whole bulk liquid regardless of the distinction between the main cluster and the isolated clusters.

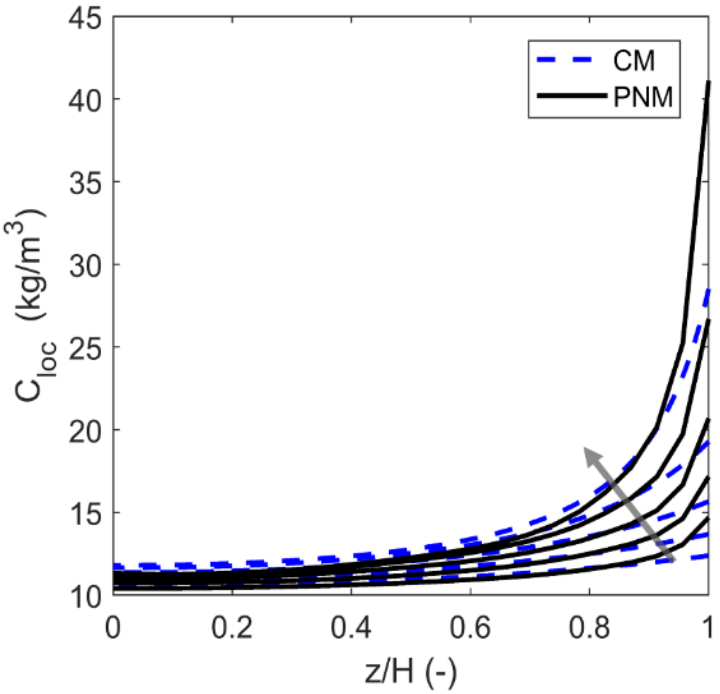

Fig. 5.4: CM solution based on effective diffusivity extracted from PNM simulation results compared with corresponding PNM simulation results. The profiles are presented for network saturations of 0.9, 0.85, 0.80, 0.75 and 0.70. The arrow indicates the trend of the profiles with decrease in overall network saturation S_{net}.

As can be seen, the CM solution underestimates the concentration at the surface. This means, for instance, that the CM model should predict the crystallization onset later than the PNM solution. This might explain why the time of first crystallization determined from CM simulation is longer than in the experiments (Hidri et al., 2013). Based on the non-compliance in CM solution adjacent to and at the evaporative surface, it is evident that in order to further improve the CM solution, an investigation dedicated to studying the dynamics of solute transport at the surface must be performed. In this regard, the pore scale insight offered by PNM simulations can be

exploited. To this end, we present a detailed analysis focused on transport at the porous medium surface in the following sections.

5.4 Liquid phase connectivity and solute transport at the surface

In Fig. 5.5, we present the instantaneous solute concentration and the liquid connectivity mapping for the liquid in vertical surface throats for various network saturation values. Note that the results presented in this section are based on one PNM simulation, as opposed to the results presented in Sec. 5.2 which are averages of multiple simulations, each with a different realization of throats size distribution.

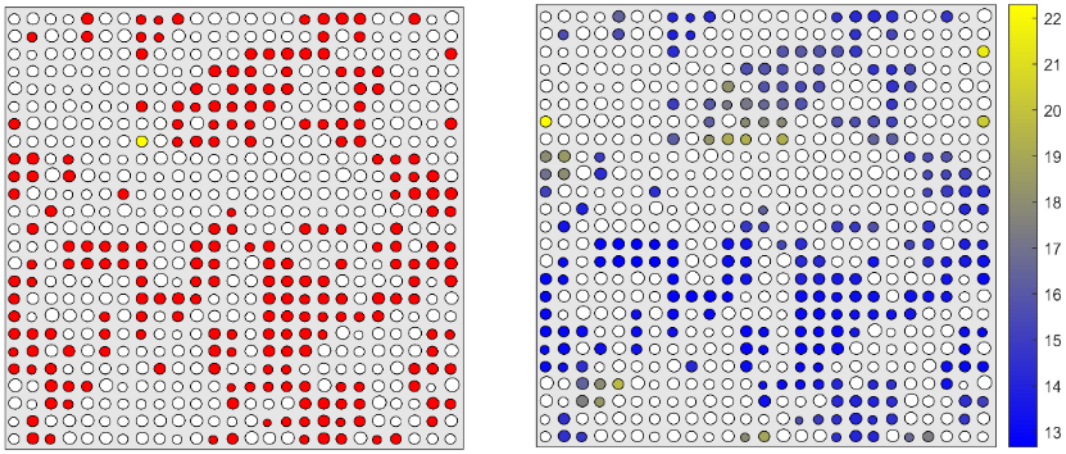

(a)

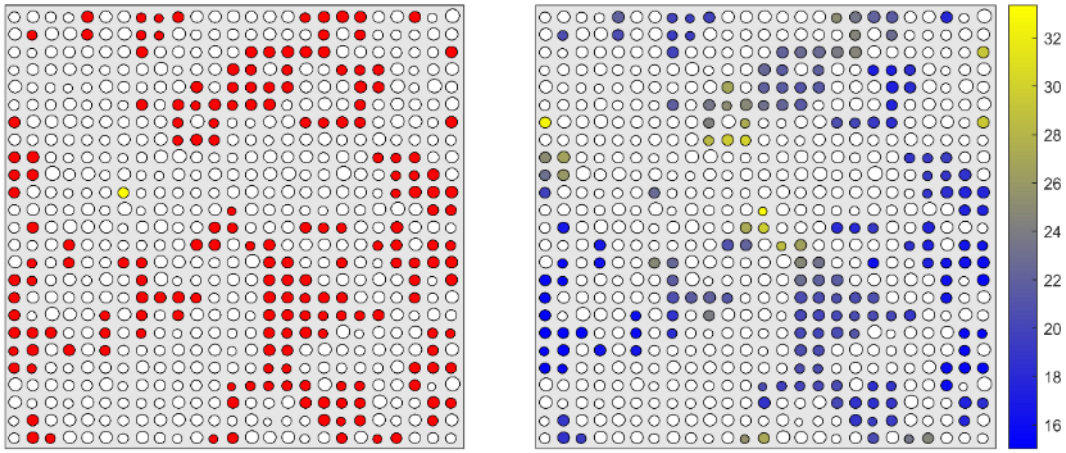

(b)

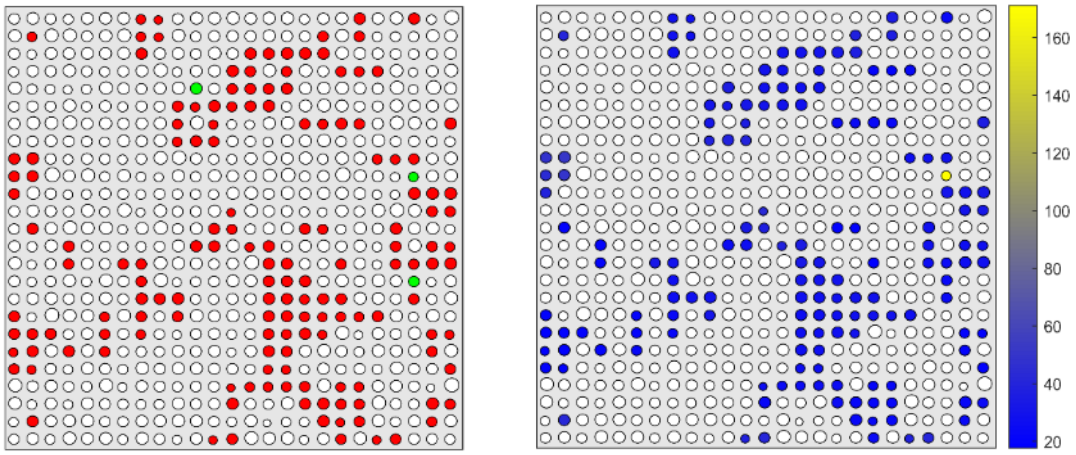

(c)

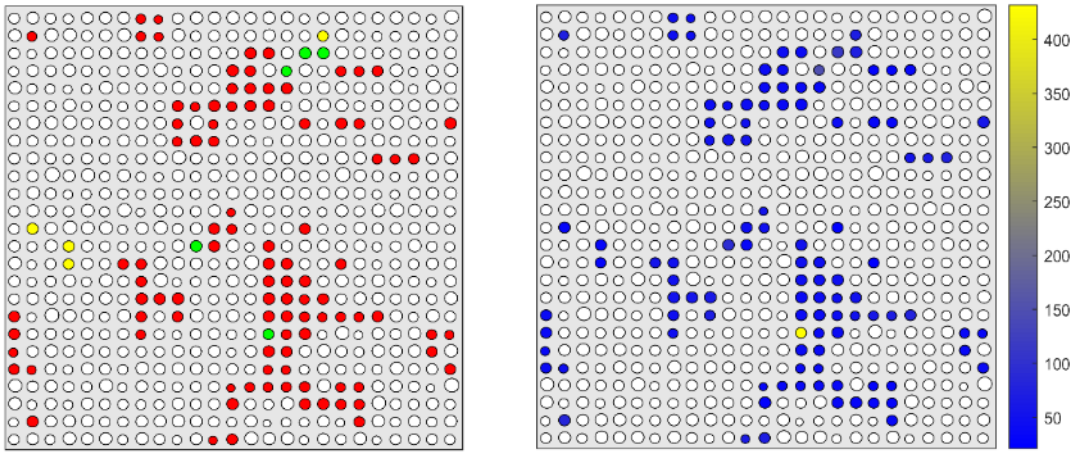

(d)

Fig. 5.5: The column on the left shows the liquid connectivity for vertical surface throats, where the red color represents throats that belong to the main cluster, green color represents the isolated single throats and yellow color represents the throats that belong to isolated liquid clusters. The column on the right maps the solute concentration for the corresponding throats, where the legend (vertical bar) indicates the range of solute concentration values in the throats. Plots in (a) to (d) represent results for network saturation values of 0.90, 0.80, 0.75 and 0.70, respectively. The size of the throats is scaled up for ease of visualization.

The liquid connectivity plots for various network saturation values presented in Fig. 5.5 reveal that the majority of surface throats belong to the main cluster. Moreover, there is no distinct trend in the variation of the proportion of isolated liquid phase with decrease in network saturation. This is because, as mentioned in Sec. 5.2, the

surface throats that belong to isolated liquid phase get evaporated quickly because of their limited volume (and hence limited supply of liquid through capillary pumping) and higher evaporation rate on the surface (no evaporation screening effect because of direct exposure to the boundary layer). The proportion of surface throats that belong to isolated liquid phase is an important factor as the solute concentration values in the isolated clusters and isolated single throats are relatively high as compared to that in the main cluster, regardless of the network saturation value.

The solute concentration maps presented in Fig. 5.5 reveal that the solute concentration fluctuates spatially in the main cluster at the surface. This is more visible for the network saturations S_{net} = 0.9 and 0.8. For the lower saturations, the concentration fluctuations in the main cluster are hidden by the quite large concentration variation range due to the very high concentrations reached in a few isolated throats. For this reason, the concentration distribution in the main cluster at the surface for S_{net} = 0.75 and 0.7 are more specifically shown in Fig. 5.6. As discussed in Veran-Tissoires et al. (2014) for the simpler evaporation-wicking situation, two main factors explain the concentration fluctuations in the main cluster. The first one is referred to as the internal disorder effect. Due to the internal disorder of the pore space, i.e. the fact that the throat sizes vary randomly, the pore-scale velocity field also fluctuates spatially. This means that the mean velocity in a throat varies from one throat to the other. Also, the velocity field in the throats fluctuates in time due to the main cluster mass loss and fragmentation. As a result of these fluctuations, the concentration, which greatly depends on the advective transport, also fluctuates. The second factor is referred to as the surface disorder effect. As a result of the throat size variation at the surface and the formation of wet patches of different sizes (a wet patch refers to a 2D cluster of saturated throats (Attari Moghaddam et al., 2018) at the surface which is surrounded by gas throats), the evaporation rate varies from one wet throat to the other at the surface. These evaporation rate variations induce velocity variations in the vertical wet throats connecting the network to the surface, which, in turn, induce concentration variations. In particular, the spacing between the wet patches at the surface plays a key role on the diffusive vapor flux per pore (see e.g., Chauvet et al., 2009). Similarly, a dry patch refers to a 2D cluster of gas throats surrounded by liquid

throats. Larger dry patches between the wet patches may result in higher evaporation fluxes through the wet patches, therefore higher solute concentration pores that have higher evaporation rate. The liquid patch on the mid-left of Fig. 5.6, for network saturation of 0.75, is an example of the high solute concentration as a result of high evaporation rate because it is surrounded by large dry patches.

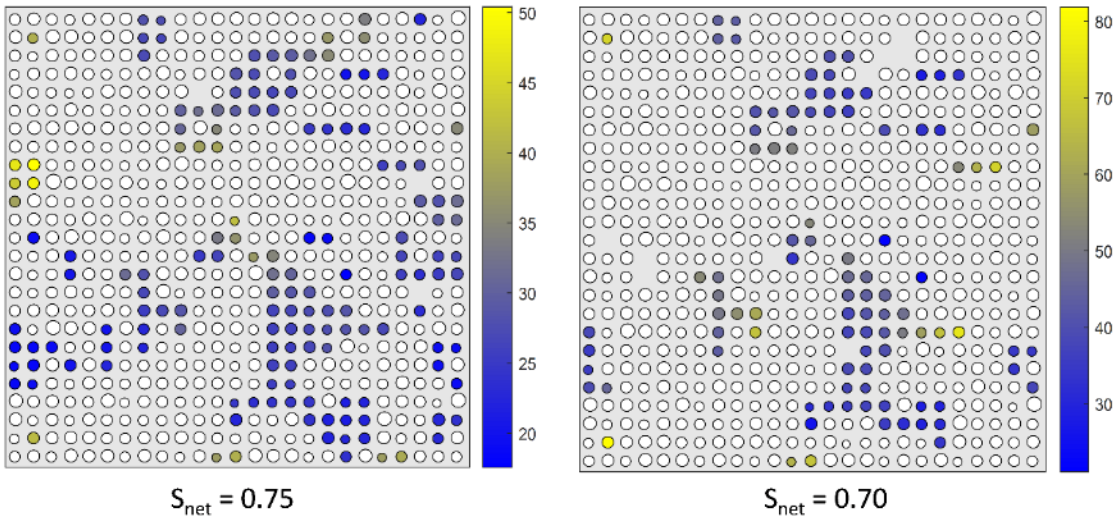

Fig. 5.6: Solute concentration maps for main cluster surface throats for network saturations of 0.75 and 0.70. The saturated throats that belong to isolated liquid phase are not shown. Legend (vertical bar) indicates the range of solute concentration values in the throats.

The solute concentration maps for network saturations of 0.75 and 0.70 presented in Fig. 5.5 show that solute concentration can rise to very high values in the isolated liquid phase compared to the main cluster. This is due to two main factors in case of single isolated throats. First the lifespan of such a throat is quite short since the volume of solution in it is small and evaporation is intense at the surface. Thus, the concentration is already high in such a throat when it forms, since it forms as the result of fragmentation of the main cluster or an isolated cluster where the concentration is high. Then the volume of solution in the throat rapidly decreases due to evaporation, which leads to a sharp increase in solute concentration. A similar process occurs in isolated clusters connected to the surface, with in addition subsequent fragmentations and increases in the concentration due to the solution volume shrinking effect.

5.5 Statistical analysis of transport at the surface based on PNM Monte Carlo simulations

As presented in Sec. 5.4, the evolution of solute concentration at the surface is strongly linked to the evolution of liquid structure at the surface. However, the heterogeneity in liquid phase structure is strongly dependent on the throat size distribution which varies in each PNM simulation. Therefore, in this section, we characterize stochastically the evolution of liquid phase structure and solute concentration at the surface. Moreover, as the main purpose of the PNM simulations is to provide a benchmark for the CM solution, a key parameter in this comparison can be the onset of crystallization based on a threshold value of solute concentration. Due to the averaging of data on the scale of local slices and the subsequent averaging of these results among multiple simulations with different realizations of throat size distribution, it is possible that the onset of crystallization on the pore scale in a PNM simulation may not be visible in the resulting instantaneous saturation and solute concentration profiles presented in Sec. 5.2. Therefore, we need to perform a dedicated study at the pore scale. For this purpose, we conduct a thorough analysis based on Monte Carlo simulations by performing 70 PNM simulations with varying realizations of the throat size distribution. Similar to the surface analysis presented in Sec. 5.4, the statistical analysis is focused only on the vertical surface throats.

Based on the data obtained from the Monte Carlo simulations, we characterize the liquid phase heterogeneity with respect to varying network saturation values and present the results in the form of a histogram. As indicated in Fig. 5.7, nearly all of the saturated surface throats are likely to be part of the main cluster until S_{net} = 0.8. Also, for network saturation of 0.75, the probability that a saturated surface throat belongs to the main cluster is still 0.97. However, when network saturation reaches 0.7, the probability that a saturated surface throats belong to the main cluster decreases to 0.917, whereas that of belonging to isolated clusters and single isolated throats is 0.052 and 0.031, respectively.

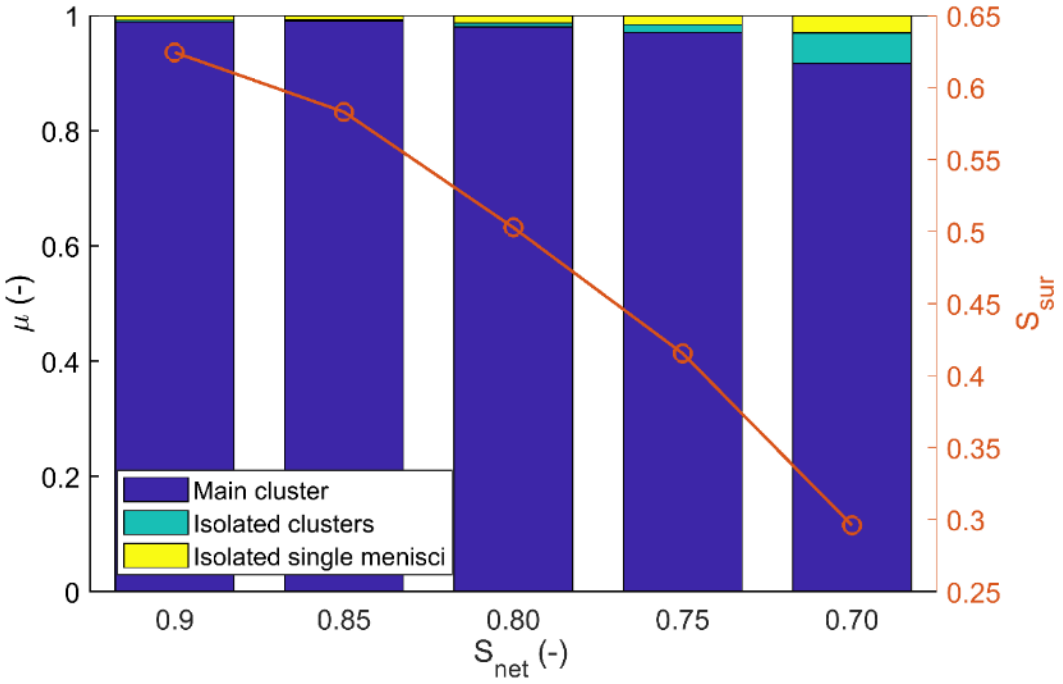

Fig. 5.7: Statistical analysis of the liquid phase heterogeneity based on Monte Carlo PNM simulations. The bars quantify the probability of a saturated surface throat being part of the main cluster, part of an isolated cluster or a single isolated throat. The line plot (corresponding to y-axis on the right) quantifies the surface slice saturation with respect to different network saturation values.

Apart from the stochastic characterization of liquid connectivity of surface throats, Fig. 5.7 also illustrates the variation of surface slice saturation with network saturation. Interestingly, for the initial 10 % decrease in network saturation, there is a dramatic decrease of approximately 38 % in saturation of the surface slice. Afterwards, the decrease in surface slice saturation is for further 10 % decrease in network saturation, i.e. from S_{net} = 0.90 to 0.80, is relatively small, i.e. S_{sur} decreases from 0.62 to 0.50. As network saturation decreases from 0.80 to 0.70, the surface slice saturation decreases from 0.50 to approximately 0.30. Overall, the decrease in surface slice saturation is the highest as network saturation decreases from 1 to 0.90. The edge effect is therefore quite significant with significantly less saturation in the top slice compared to the bulk.

Figure 5.8 illustrates the probability of reaching of specified threshold concentration value, denoted by C_{th}. In this example, C_{th} is equal to 50 kg/m^3 whereas the initial concentration is as mentioned before C_0 = 10 kg/m^3. Thus, the threshold value corresponds here to an increase of the concentration by a factor 5 compared to the initial concentration. The line plot (corresponding to the y-axis on the right) represents the absolute probability of reaching the threshold value in a saturated surface throat (absolute probability does not distinguish between the main cluster and isolate liquid phase).

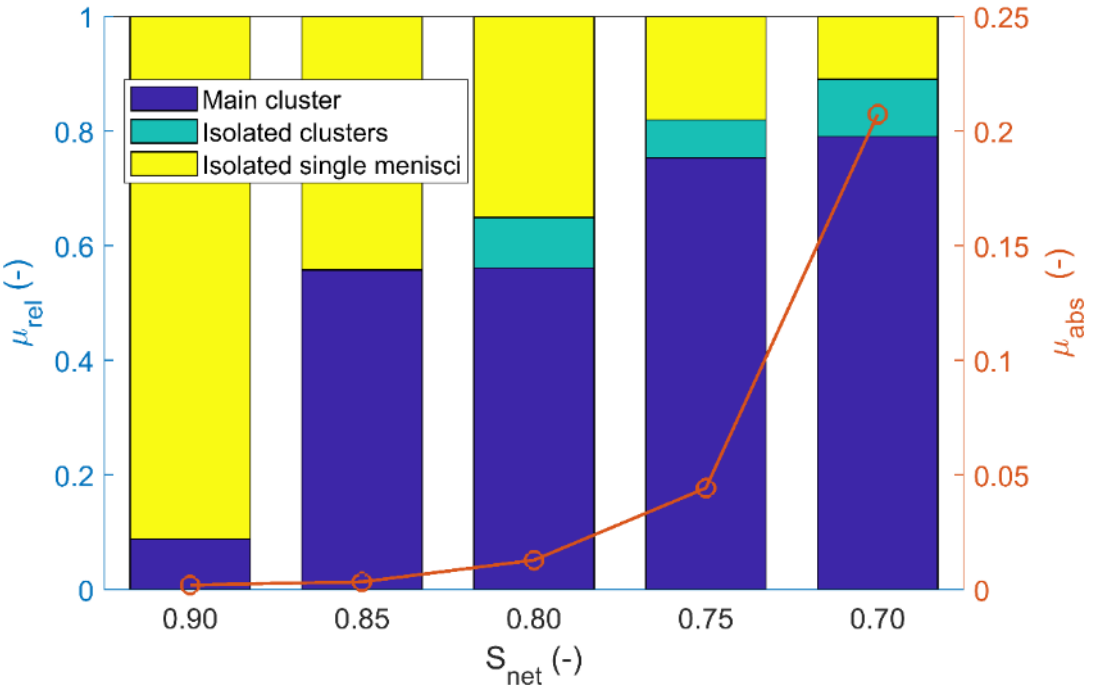

Fig. 5.8: Statistical analysis quantifying the probability of reaching a concentration threshold value equal to 5 times the initial concentration. The line plot (corresponding to y-axis on the right) quantifies the absolute probability of reaching the concentration threshold value in surface throats with respect to different network saturation values. The bars (corresponding to the y-axis on the left) quantify the probability of reaching the concentration threshold value within the respective liquid phase elements with respect to the total number of throats in which the concentration threshold value is reached.

As can be observed, the probability of reaching the threshold value for S_{net} values of 0.90 and 0.85 is extremely low, while the probability of reaching the threshold value

is higher in single isolated throats as compared to the main cluster (as illustrated by the respective histograms). In other words, if one assumes for instance that the ratio C_{th} / C_0 = 5 corresponds to the onset of crystallization, Fig. 5.8 shows that the probability of crystallization in this example for S_{net} values of 0.90 and 0.85 is quite low and that the crystallization, when it happens, occurs with a much greater probability in an isolated single throat than at the top of the main. As network saturation decreases from 0.75 to 0.70, the absolute probability of reaching the concentration threshold value for all saturated vertical surface throats increases significantly from 0.044 to 0.21. It can be observed that the probability of reaching the concentration threshold value in a saturated surface throat increases exponentially as the end of CRP is approached.

At intermediate network saturation values, e.g. 0.80, the probability of reaching the concentration threshold value in isolated liquid phase approximately matches that of the main cluster. It is obvious that the commonly used CM cannot capture these effects which reflect the impact of heterogeneities at a scale lower than the Representative Elementary Volume (REV) scale typically associated with the macroscopic modeling.

At first glance, the results reported in Fig. 5.8 could be seen as in contradiction with the solute concentration profiles depicted in Fig. 5.2. Fig. 5.2 shows that the greater concentration at the surface is observed in the isolated cluster for all the considered network saturations. On the other hand, Fig. 5.8 shows that the concentration threshold value at the surface is reached with a greater probability in the main cluster when the network saturation is sufficiently low, for example $S\ net$ = 0.7, in the case considered. The latter result simply reflects the fact that, as illustrated in Fig. 5.5, there are much more surface throats belonging to the main cluster than to isolated clusters. For instance, if the concentration threshold was selected such that the solute concentration is greater than the considered concentration threshold value in all liquid throats at the surface, the probabilities plotted in Fig. 5.8 would be simply given by

$$\mu_{abs-mc} = \frac{number\ of\ surface\ throats\ in\ main\ cluster}{number\ of\ liquid\ surface\ throats} \tag{5.13}$$

$$\mu_{abs-ic} = \frac{number\ of\ surface\ throats\ in\ isolated\ clusters}{number\ of\ liquid\ surface\ throats} \quad (5.14)$$

with $\mu_{rel-mc} = \mu_{abs-mc}$, $\mu_{rel-ic} = \mu_{abs-ic}$ for this particular case.

In terms of probability of crystallization during the CRP, the results can be summarized as follows. As shown in Fig. 5.2, the crystallization should systematically start in the isolated clusters. This is because the fast evaporation of the isolated clusters connected to the surface leads to a rapid increase in the solute concentration. However, these clusters can be small or even can simply be liquid bridges (the single isolated throats in our simulations). As a result, this crystallization is likely to correspond to a relatively small amount of crystals. As a result, the formation of these crystals could only marginally affect the evaporation process. After a while, the crystallization concentration should be reached in the main cluster at the surface (as indicated by Fig. 5.2 and Fig. 5.8). Then, the development of crystals (efflorescence) can be expected to be much more important since the main cluster corresponds to a much greater amount of salt compared to an isolated cluster. A detailed analysis of the above dynamics would however require to include the crystallization process in the modeling and to couple the efflorescence development with the modeling of evaporation and solute transport processes. This is a quite challenging objective, which has not yet been addressed in the framework of pore network modeling.

5.6 Remarks

The drying pore network simulations reported in this study show two striking differences compared with the predictions of the commonly used continuum model as regards the saturation profiles during the CRP in the capillary dominant regime, which was the focus of this study. First the saturation profiles become flat in the bulk only after an initial period which is typically not seen with the CM, nor in the experiments (e.g. Gupta et al., 2014). Second a quite significant edge effect is observed leading to a significantly reduced saturation in the top region of the network

compared to the bulk. The ratio between the saturation in the bulk and at the surface can be greater than 2. The first effect is a finite size effect due to the small size of the considered network compared to the typical size of the porous medium in experiments. Therefore, this effect needs not specific consideration since it is expected to be negligible with usual porous media. However, it might need consideration in applications involving thin porous media, such as in fuel cells, for example, Prat et al. (2015). The second effect, referred to as the edge effect, is more problematic. Unlike the first effect, preliminary simulations (not shown in this study) suggest that it is not network size dependent.

The comparison between the predictions of the commonly used continuum model (CM) and the pore network model as regards the solute transport shows that the CM underpredicts the concentration at the evaporative surface compared to the PNM simulations. This can be mainly attributed to the edge effect since the saturation variations are one of the important factors controlling the evolution of solute concentration. The greater saturation variation in the edge region leads to greater solute concentration compared to the predictions of the CM. This is an indication that the traditional continuum model should overpredict the crystallization onset time at the porous medium surface.

Another important feature, which is not captured by the traditional CM, is related to the liquid phase structuration in liquid clusters. The PNM simulations show that the dominant mechanisms controlling the solute concentration variations in the porous medium top region are different in the percolating main cluster and the isolated clusters. The solute concentration variations are mainly due to the saturation variations in the isolated clusters and the combination of advective transport and saturation variations in the main cluster. The solute concentration at the surface is greater in the isolated clusters than in the main cluster. This suggests that an improvement should be to develop a drying continuum model making an explicit distinction between the main cluster, i.e. the percolating liquid phase, and the isolated cluster, i.e. the non-percolating liquid phase.

In this chapter, the macroscopic data were obtained from the PNM simulations by volume averaging considering relatively thin slices as averaging volumes. Then the question arises as to whether the slices can be considered as a truly representative averaging volume. In this respect, it would be interesting to consider thicker averaging volumes and perform simulations over larger networks. This is not possible with the current version of the drying PNM code used in this chapter. Although the traditional length scale separation criterion is therefore not fully met in our simulations, we however consider our work to give valuable insights into the shortcomings of the conventional continuum model.

Chapter 6

Summary and outlook

6.1 Summary

In this thesis, we addressed a series of shortcomings in the current state of the art of continuum modeling of drying capillary porous media. We used numerical pore network simulations to elucidate how the pore scale phenomena impact the macroscopic scale both at the surface and inside the porous medium. Also, the information obtained from pore network simulations guided the development of theoretical framework for more advanced continuum models. The main macroscopic transport parameters that were computed from PNM simulations are the effective vapor diffusivity, specific interfacial area, liquid phase diffusivity, interfacial area at the porous medium surface and effective solute diffusivity. The key aspects that were addressed include: the flawed assumption of local equilibrium between liquid and gas phases, the poor modeling of mass transfer at the porous medium surface, and in-depth assessment of the continuum model of dying with dissolved solute transport. Throughout this thesis, we consider drying at ambient conditions and neglect any temperature variations. The considered porous medium is rigid, homogenous and non-hygroscopic. We do not consider heat transfer in the modeling approach and assume that evaporation is controlled by mass transfer.

In addressing the erroneous assumption of local equilibrium between the liquid and vapor phases in a drying capillary porous medium, a two-equation continuum model was formulated based on an upscaling technique. In the two-equation CM, saturation accounts for the liquid phase and partial vapor pressure accounts for the respective

mass transport in the vapor phase. The liquid and vapor phase equations are coupled by a source/sink term that considers the NLE mass exchange between the two phases. In order to simplify the problem, it was decided to address the problem in two steps.

In the first step, we neglected the macroscopic capillary transport in the liquid phase by considering an initial phase distribution in which the liquid is distributed into small disconnected clusters. The NLE CM was derived based on the volume averaging method. The formulation of the NLE mass exchange term, which couples the two equations of the NLE CM, is based on specific interfacial area, the deviation of vapor pressure from saturation vapor pressure and a mass exchange coefficient. The macroscopic parameters needed for the CM solution were computed from PNM simulations based on a network of 25×25×50. These parameters were computed from the averaged results of a number of PNM simulations each with a different realization of throat size distribution and location of the isolated liquid clusters inside the network.

The method of slice averaging, which was used to extract the macroscopic parameters from the 3D PNM simulations, is similar to what was recently used by Attari Moghaddam et al. (2017) with the exception of the configuration of the slice. A change in the slice discretization scheme was needed because of the consideration of partial vapor pressure as a process variable. For the solution of the NLE CM, effective diffusivity and specific interfacial area were computed from PNM simulations of drying. The mass exchange coefficient was not computed from PNM simulations and instead it was used as a fitting parameter such that a good agreement is obtained between the NLE CM solution and the PNM results. The comparison between the solution of NLE CM and the PNM simulations was based on saturation profiles, vapor pressure profiles, the NLE effect and the total evaporation rate. It was shown that the NLE CM produced the aforementioned PNM results with a good degree of accuracy.

Following the development of the two-equation CM for the limiting case of immobile liquid phase, this CM was extended in order to consider the drying of a fully saturated capillary porous medium, such that in addition to the vapor diffusion, the evaporation

induced capillary-viscous transport in the liquid phase is also considered. Owing to the consideration of macroscopic transport in the liquid phase, the solution of the two-equation CM required the formulation of boundary condition for the vapor phase. This means that we also addressed the problem of mass transport at the porous medium surface by introducing coupled formulations for the boundary conditions of the liquid and gas phase equations.

Similar to the case of NLE CM for the limiting case of immobile liquid phase, the comparison between the solution of NLE CM for full drying and the PNM simulation results was made in terms of the drying time. This is different from what was previously considered in the work on the one-equation CM by Attari Moghaddam et al. (2017) where the comparisons between PNM and CM results were based on network saturation values. Comparing the state of the system in terms of drying time is more logical in terms of assessing the prediction capability of the CM.

The derivation of the two-equation NLE CM was based on an upscaling technique, which permits the translation of the pore scale phenomena to the macroscopic scale on a firmer basis. The upscaling led to the introduction of specific interfacial area as a key macroscopic parameter in the NLE phase change term. Also, the formulation of the two-equation CM permits to distinguish between the process of local evaporation and the diffusive transport of the evaporated vapor. The CM formulation suggests that the presence of liquid phase does not influence the vapor transport other than acting as a mere inert hindrance similar to that of the solid phase. In other words, no enhancement factor is considered in the vapor diffusion model.

The formulation of the two-equation NLE CM captures the transport phenomena involved in the drying of a non-hygroscopic porous medium in a more physically realistic way as compared to the aforementioned one-equation CM. Unlike the one-equation CM, the two-equation CM does not require the NLE surface relationship between the vapor partial pressure and the surface saturation as an input parameter. Instead, this NLE relationship is an output of the two-equation CM. The results showed that the NLE two-equation CM for the fully saturated porous medium can

independently reproduce the reference PNM data, i.e. the drying kinetics, the phase distributions and the NLE effect with a reasonable degree of accuracy.

Additionally, the NLE two-equation CM was investigated by performing a sensitivity study of the macroscopic parameters. It was observed that mass exchange coefficient is a key factor that directly affects the dynamics towards the local equilibrium. For example, the CM approaches the LE situation for higher values of mass exchange coefficient resulting in a sharper drying front. For lower values of mass exchange coefficient, the NLE effect becomes stronger and as a result the drying front is smoother and more continuous.

In this thesis, the macroscopic advective-diffusive transport equation was investigated in its ability to reproduce the evolution of solute concentration in a drying capillary porous medium, while focusing only on the constant rate period (CRP). For this purpose, using PNM simulations as a guide and reference for comparison, the influence of liquid phase fragmentation (splitting of main liquid cluster into isolated elements, i.e. isolated clusters and isolated single meniscus throats) on the solute concentration profiles was elucidated. The CM was solved with the help of effective solute diffusivity obtained from PNM simulations.

The solute concentration profiles obtained from the solution of CM of drying with dissolved solute transport showed a discrepancy with the corresponding PNM results in the edge effect region near the porous medium surface i.e. the CM underpredicted the solute concentration in this edge effect region. Hence, a dedicated study focusing on the transport at the surface was performed with the help of PNM simulations. This study consisted of 2D mapping of the solute concentration in the surface throats and a statistical analysis of the evolution of liquid connectivity and solute concentration in the surface throats with the help of PNM Monte Carlo simulations. Based on an arbitrarily selected threshold value for saturation concentration, the prediction capacity for the onset of crystallization was statistically analyzed.

Based on the detailed analysis with the help of PNM simulations, it was observed that the larger saturation variation in the edge effect region is the main reason for the larger

solute concentration in this region as compared to the rest of the network. As the traditional CM does not consider the edge effect, therefore it would overpredict the time for onset of crystallization.

PNM simulations showed that the dominant mechanisms controlling the solute concentration variations in the porous medium top region are different in the main cluster and in the isolated parts of the liquid phase: the solute concentration variations are due to advective transport and saturation variations in the main cluster, whereas, for the isolated liquid phase, they are due to the birth of isolated clusters as they get fragmented from the main cluster and their subsequent shrinkage. However, the classical CM does not capture these phenomena of fragmentation in the liquid clusters. Therefore, it is important to consider these heterogeneities related to the evolution of liquid structure in the CM formulation in order to make the CM more accurate and physical realistic.

6.2 Outlook

The size of the REV (determined in previous works with the existing PNM codes for the capillary controlled invasion percolation simulations) is 25×25×25. The maximum size for the pore network used in this thesis is 25×25×50, i.e. twice the REV size. This violates the length scale separation criterion, which is a requirement that needs to be fulfilled in order to compute volume averaged data from PNM simulation results. Thus, pore network simulations on significantly larger networks (e.g. with 300 pores in the direction of the boundary layer) should be performed. However, this is not possible with the current form of the PNM codes, which can take up to 100 days on a multi-core computer (Attari Moghaddam, 2017) for one realization in capillary-gravity regime (without consideration of secondary capillary structures or dissolved solute transport) for a network of 100×100×101 nodes. Hence, it is important to develop PNM codes that are suitable for high performance computing (HPC) on workstations that can take advantage of the power of parallel computing. Once the HPC codes for the simple drying situation are developed, they can be extended to consider drying in presence of secondary capillary structures and dissolved solute

transport. Then, comparisons between the volume averaged data obtained from HPC PNM simulations and the corresponding solutions of CM can be performed for the purpose of validation and assessment. HPC PNM simulations of drying will also shed light on the transport phenomenon at the porous medium surface and will help to validate the boundary conditions for the two-equation CM as well. Using the HPC PNM codes, an extensive statistical analysis can also be performed based on Monte Carlo simulations with variations in throat radius, throat length, throat size distribution, Bond number, capillary number and Péclet number.

Regarding the improvement in the classical CM for drying in presence of dissolved solute transport, a logical next step is to take into account the liquid phase fragmentation process in the continuum model formulation. This implies developing a drying continuum model that makes an explicit distinction between the main cluster, i.e. the percolating liquid phase, and the isolated liquid elements, i.e. the non-percolating liquid phase. This CM would be termed as a three-equation CM which consists of a transport equation based on vapor phase, percolating liquid phase saturation and the non-percolating liquid phase saturation, respectively. A starting point for approaching this problem can be a model that has been proposed for the two-phase flow in porous media in Doster et al. (2010), which can be extended and adapted to the situation of drying.

An important phenomenon which was not considered in this thesis is the presence of secondary capillary structures. In this respect, an attractive option is to consider the liquid in the film region as a distinct phase, such that the liquid phase saturation is characterized by the film saturation and bulk saturation, respectively. Here, a PNM of drying with continuous liquid films, which is based on the work by Prat (2007), already exists and can be used for pores scale insights and benchmark results. As a first step, the problem can be approached in simplified manner by considering a regime in which the bulk liquid is distributed into isolated clusters and the mass transport towards the evaporative surface is through capillary liquid films (as no dry zone would form within the network). This transport regime, which is in fact analogous to the problem of drying (without liquid films) in the presence of immobile

liquid phase (see Chapter 3), can be referred to as drying with hyperdeveloped continuous liquid films. The mass transfer from the bulk liquid to the liquid in the film region can be characterized by a source/sink term based on the specific interfacial area between films and bulk menisci and the deviation of the film saturation from the maximum film saturation (which is known a priori). Once, the simplified version of the CM is validated, it can then be extended for the situation in which the vapor phase exists within the network as well. However, the fact that the current form of the PNM with continuous liquid films does not consider the inter-cluster mass transport through liquid films, can be a challenge in this respect. In this regard, one option is to characterize the secondary capillary structures experimentally consisting of X-ray microtomography based drying in 3D random packings of glass beads.

Bibliography

Ahmad, F., Talbi, M., Prat, M., Tsotsas, E., Kharaghani, A.: Non-local equilibrium continuum modeling of partially saturated drying porous media: Comparison with pore network simulations. Chem. Eng. Sci. 228, 115957 (2020). https://doi.org/10.1016/j.ces.2020.115957

Altaf, H., Vorhauer, N., Tsotsas, E., Vidaković-Koch, T.: Steady-state water drainage by oxygen in anodic porous transport layer of electrolyzers: A 2D pore network study. Processes. 8, 362 (2020). https://doi.org/10.3390/pr8030362

Attari Moghaddam, A.: Parameter estimation and assessment of continuum models of drying on the basis of pore network simulations (Doctoral thesis), Otto-von-Guericke-Universität Magdeburg, Germany, http://dx.doi.org/10.25673/4780, (2017)

Attari Moghaddam, A., Kharaghani, A., Tsotsas, E., Prat, M.: Kinematics in a slowly drying porous medium: Reconciliation of pore network simulations and continuum modeling. Phys. Fluids. 29, (2017)(a). https://doi.org/10.1063/1.4975985

Attari Moghaddam, A., Kharaghani, A., Tsotsas, E., Prat, M.: A pore network study of evaporation from the surface of a drying non-hygroscopic porous medium. AIChE J. 64, 1435–1447 (2018). https://doi.org/10.1002/aic.16004

Attari Moghaddam, A., Prat, M., Tsotsas, E., Kharaghani, A.: Evaporation in capillary porous media at the perfect piston-like invasion limit: Evidence of nonlocal equilibrium effects. Water Resour. Res. 53, 10433–10449 (2017)(b). https://doi.org/10.1002/2017WR021162

Bénet, J.-C., Lozano, A.-L., Cherblanc, F., Cousin, B.: Phase change of water in a hygroscopic porous medium: Phenomenological relation and experimental analysis for water in soil. J. Non-Equilibrium Thermodyn. 34, (2009). https://doi.org/10.1515/JNETDY.2009.008

Bénet, J.C., Jouanna, P.: Phenomenological relation of phase change of water in a porous medium: Experimental verification and measurement of the phenomenological coefficient. Int. J. Heat Mass Transf. 25, 1747–1754 (1982). https://doi.org/https://doi.org/10.1016/0017-9310(82)90154-5

Blunt, M.J., Jackson, M.D., Piri, M., Valvatne, P.H.: Detailed physics, predictive capabilities and upscaling for pore-scale models of multiphase flow. Adv. Water Resour. 25, 1069–1089 (2001)

Börnhorst, M., Walzel, P., Rahimi, A., Kharaghani, A., Tsotsas, E., Nestle, N., Besser, A., Kleine Jäger, F., Metzger, T.: Influence of pore structure and impregnation–drying conditions on the solid distribution in porous support materials. Dry. Technol. 34, 1964–1978 (2016). https://doi.org/10.1080/07373937.2016.1147048

van Brakel J.: Mass transfer in convective drying. In: Mujumdar, A.S. (ed.) Advances in drying. pp. 217–267. Hemisphere, New York (1980)

Le Bray, Y., Prat, M.: Three-dimensional pore network simulation of drying in capillary porous media. Int. J. Heat Mass Transf. 42, 4207–4224 (1999). https://doi.org/10.1016/S0017-9310(99)00006-X

Carrère, P., Prat, M.: Optimisation of gas access through a thin porous layer with a partially occluded inlet surface. Transp. Porous Media. 133, 49–69 (2020). https://doi.org/10.1007/s11242-020-01413-0

Chauvet, F., Duru, P., Geoffroy, S., Prat, M.: Three periods of drying of a single square capillary tube. Phys. Rev. Lett. 103, 1–4 (2009). https://doi.org/10.1103/PhysRevLett.103.124502

Chen, X.Y.: Evaporation from a salt-encrusted sediment surface: Field and laboratory studies. Aust. J. Soil Res. 30, 429–442 (1992). https://doi.org/10.1071/SR9920429

Coussot, P.: Scaling approach of the convective drying of a porous medium. Eur. Phys. J. B. 15, 557–566 (2000). https://doi.org/10.1007/s100510051160

Culligan, K.A., Wildenschild, D., Christensen, B.S.B., Gray, W.G., Rivers, M.L.: Pore-scale characteristics of multiphase flow in porous media: A comparison of air-water and oil-water experiments. Adv. Water Resour. 29, 227–238 (2006). https://doi.org/10.1016/j.advwatres.2005.03.021

Dashtian, H., Shokri, N., Sahimi, M.: Pore-network model of evaporation-induced salt precipitation in porous media: The effect of correlations and heterogeneity. Adv. Water Resour. 112, 59–71 (2018). https://doi.org/10.1016/j.advwatres.2017.12.004

Diouf, B., Geoffroy, S., Chakra, A.A., Prat, M.: Locus of first crystals on the evaporative surface of a vertically textured porous medium. EPJ Appl. Phys. 81, 1–14 (2018). https://doi.org/10.1051/epjap/2018170340

Doster, F., Zegeling, P.A., Hilfer, R.: Numerical solutions of a generalized theory for macroscopic capillarity. Phys. Rev. E. 81, 036307 (2010). https://doi.org/10.1103/PhysRevE.81.036307

Eloukabi, H., Sghaier, N., Ben Nasrallah, S., Prat, M.: Experimental study of the effect of sodium chloride on drying of porous media: The crusty-patchy efflorescence transition. Int. J. Heat Mass Transf. 56, 80–93 (2013). https://doi.org/10.1016/j.ijheatmasstransfer.2012.09.045

Faiyas, A.P.A., Erich, S.J.F., Huinink, H.P., Adan, O.C.G.: Transport of a water-soluble polymer during drying of a model porous media. Dry. Technol. 35, 1874–1886 (2017). https://doi.org/10.1080/07373937.2017.1283515

García-Salaberri, P.A., Gostick, J.T., Hwang, G., Weber, A.Z., Vera, M.: Effective diffusivity in partially-saturated carbon-fiber gas diffusion layers: Effect of local saturation and application to macroscopic continuum models. J. Power Sources. 296, 440–453 (2015). https://doi.org/10.1016/j.jpowsour.2015.07.034

Geoffroy, S., Prat, M.: A review of drying theory and modelling approaches. In: Delgado, J.M.P.Q. (ed.) Drying and Wetting of Building Materials and Components. pp. 145–173. Springer (2014)

Gomez, I., Sala, J.M., Milln, J.A.: Characterization of moisture transport properties for lightened clay brick: Comparison between two manufacturers. J. Build. Phys. 31, 179–194 (2007). https://doi.org/10.1177/1744259107082687

Goudie, A.S., Viles, H.: Weathering hazards. In: Alcántara, I., Goudie, A.S. (ed.) Geomorphological Hazards and Disaster Prevention, 145–160, Cambridge University Press, (2010). https://doi.org/10.1017/CBO9780511807527.012

Guglielmini, L., Gontcharov, A., Aldykiewicz, A.J., Stone, H.A.: Drying of salt solutions in porous materials: Intermediate-time dynamics and efflorescence. Phys. Fluids. 20, 1–7 (2008). https://doi.org/10.1063/1.2954037

Gupta, S., Huinink, H.P., Prat, M., Pel, L., Kopinga, K.: Paradoxical drying of a fired-clay brick due to salt crystallization. Chem. Eng. Sci. 109, 204–211 (2014). https://doi.org/10.1016/j.ces.2014.01.023

Haghighi, E., Shahraeeni, E., Lehmann, P., Or, D.: Evaporation rates across a convective air boundary layer are dominated by diffusion. Water Resour. Res. 49, 1602–1610 (2013). https://doi.org/10.1002/wrcr.20166

Hassanizadeh, S.M., Gray, W.G.: Mechanics and thermodynamics of multiphase flow in porous media including interphase boundaries. Adv. Water Resour. 13, 169–186 (1990). https://doi.org/10.1016/0309-1708(90)90040-B

Hassanizadeh, S.M., Gray, W.G.: Thermodynamic basis of capillary pressure in porous media. Water Resour. Res. 29, 3389–3405 (1993). https://doi.org/10.1029/93WR01495

Hidri, F., Sghaier, N., Eloukabi, H., Prat, M., Nasrallah, S. Ben: Porous medium coffee ring effect and other factors affecting the first crystallisation time of sodium chloride at the surface of a drying porous medium. Phys. Fluids. 25, (2013). https://doi.org/10.1063/1.4834356

Huinink, H.P., Pel, L., Michels, M.A.J.: How ions distribute in a drying porous medium: A simple model. Phys. Fluids. 14, 1389–1395 (2002). https://doi.org/10.1063/1.1451081

Huinink, H.P., Pel, L., Michels, M.A.J.: Structure and transport properties of liquid clusters in a drying porous medium. Phys. Rev. E. 68, 1–7 (2003). https://doi.org/10.1103/PhysRevE.68.056114

Irawan, A.: Isothermal drying of pore networks: Influence of pore structure on drying kinetics (Doctoral thesis), Otto-von-Guericke-Universität Magdeburg, Germany, (2006).

Jabbari, Y., Tsotsas, E., Kirsch, C., Kharaghani, A.: Determination of the moisture transport coefficient from pore network simulations of spontaneous imbibition in capillary porous media. Chem. Eng. Sci. 207, 600–610 (2019). https://doi.org/10.1016/j.ces.2019.07.002

Joekar-Niasar, V., Hassanizadeh, S.M., Dahle, H.K.: Non-equilibrium effects in capillarity and interfacial area in two-phase flow: Dynamic pore-network modelling. J. Fluid Mech. 655, 38–71 (2010). https://doi.org/10.1017/S0022112010000704

Joekar-Niasar, V., Hassanizadeh, S.M., Leijnse, A.: Insights into the relationships among capillary pressure, saturation, interfacial area and relative permeability using pore-network modeling. Transp. Porous Media. 74, 201–219 (2008). https://doi.org/10.1007/s11242-007-9191-7

Joekar-Niasar, V., Majid Hassanizadeh, S.: Effect of fluids properties on non-equilibrium capillarity effects: Dynamic pore-network modeling. Int. J. Multiph. Flow. 37, 198–214 (2011). https://doi.org/10.1016/j.ijmultiphaseflow.2010.09.007

Kharaghani, A.: Drying and wetting of capillary porous materials: Insights from imaging and physics-based modeling (Habilitation thesis), Otto-von-Guericke-Universität Magdeburg, German, (2020).

Kharaghani, A., Mahmood, H.T., Wang, Y., Tsotsas, E.: Three-dimensional visualization and modeling of capillary liquid rings observed during drying of dense particle packings. Int. J. Heat Mass Transf. 177, 121505 (2021). https://doi.org/10.1016/j.ijheatmasstransfer.2021.121505

Komiyama, M.: Design and preparation of impregnated catalysts. Catal. Rev. 27, 341–372 (1985). https://doi.org/10.1080/01614948508064738

Larsen, F., Tran, L.V., Van Hoang, H., Tran, L.T., Christiansen, A.V., Pham, N.Q.: Groundwater salinity influenced by Holocene seawater trapped in incised valleys in the Red River delta plain. Nat. Geosci. 10, 376–381 (2017). https://doi.org/10.1038/ngeo2938

Laurindo, J.B., Prat, M.: Numerical and experimental network study of evaporation in capillary porous media: Phase distributions. Chem. Eng. Sci. (1996). https://doi.org/10.1016/S0009-2509(96)00341-7

Lazhar, R., Najjari, M., Prat, M.: Combined wicking and evaporation of NaCl solution with efflorescence formation: The efflorescence exclusion zone. Phys. Fluids. 32, (2020). https://doi.org/10.1063/5.0007548

Le, K.H., Kharaghani, A., Kirsch, C., Tsotsas, E.: Pore network simulations of heat and mass transfer inside an unsaturated capillary porous wick in the dry-out regime. Transp. Porous Media. 114, 623–648 (2016). https://doi.org/10.1007/s11242-016-0737-4

Lehmann, P., Assouline, S., Or, D.: Characteristic lengths affecting evaporative drying of porous media. Phys. Rev. E. 77, 056309 (2008). https://doi.org/10.1103/PhysRevE.77.056309

Lehmann, P., Or, D.: Effect of wetness patchiness on evaporation dynamics from drying porous surfaces. Water Resour. Res. 49, 8250–8262 (2013). https://doi.org/10.1002/2013WR013737

Li, Z., Vanderborght, J., Smits, K.M.: Evaluation of model concepts to describe water transport in shallow subsurface soil and across the soil–air interface. Transp. Porous Media. 128, 945–976 (2019). https://doi.org/10.1007/s11242-018-1144-9

Licsandru, G., Noiriel, C., Duru, P., Geoffroy, S., Abou Chakra, A., Prat, M.: Dissolution-precipitation-driven upward migration of a salt crust. Phys. Rev. E. 100, 1–9 (2019). https://doi.org/10.1103/PhysRevE.100.032802

Lockington, D.A., Parlange, J.Y., Barry, D.A., Leech, C.A.: Drying of porous building materials: Hydraulic diffusivity and front propagation. Mater. Struct. Constr. 36, 448–452 (2003). https://doi.org/10.1617/13791

Lu, X., Kharaghani, A., Tsotsas, E.: Transport parameters of macroscopic continuum model determined from discrete pore network simulations of drying porous media: Throat-node vs. throat-pore configurations. Chem. Eng. Sci. 223, 115723 (2020). https://doi.org/10.1016/j.ces.2020.115723

Luikov, A. V.: Systems of differential equations of heat and mass transfer in capillary-porous bodies (review). Int. J. Heat Mass Transf. (1975). https://doi.org/10.1016/0017-9310(75)90002-2

Marchand, R.G., Kumaran, M.K.: Moisture diffusivity of cellulose insulation. J. Therm. Insul. Build. Envel. 17, 362–377 (1994). https://doi.org/10.1177/109719639401700406

Médici, E.F., Allen, J.S.: Evaporation, two phase flow, and thermal transport in porous media with application to low-temperature fuel cells. Int. J. Heat Mass Transf. 65, 779–788 (2013). https://doi.org/10.1016/j.ijheatmasstransfer.2013.06.035

Metzger, T.: A personal view on pore network models in drying technology. Dry. Technol. 37, 497–512 (2019). https://doi.org/10.1080/07373937.2018.1512502

Metzger, T., Irawan, A., Tsotsas, E.: Erratum: Extension of Hoshen-Kopelman algorithm to non-lattice environments (Physica A: Statistical Mechanics and Its

Applications (2003) 321 (665-678)). Phys. A Stat. Mech. its Appl. 363, 558–560 (2006). https://doi.org/10.1016/j.physa.2005.08.026

Metzger, T., Tsotsas, E.: Influence of pore size distribution on drying kinetics: A simple capillary model. Dry. Technol. 23, 1797–1809 (2005). https://doi.org/10.1080/07373930500209830

Metzger, T., Tsotsas, E., Prat, M.: Pore-network models: A powerful tool to study drying at the pore level and understand the influence of structure on drying kinetics. In: Tsotsas, E., Mujumdar, A.S. (ed.) Modern Drying Technology: Computational Tools at Different Scales. 1, 57–102, (2007).

Millington, R.J., Quirk, J.P.: Permeability of porous solids. Trans. Faraday Soc. 57, 1200–1207 (1961). https://doi.org/10.1039/TF9615701200

Moldrup, P., Olesen, T., Komatsu, T., Schjønning, P., Rolston, D.E.: Tortuosity, diffusivity, and permeability in the soil liquid and gaseous phases. Soil Sci. Soc. Am. J. 65, 613–623 (2001). https://doi.org/10.2136/sssaj2001.653613x

Mujumdar, A.S. (ed.): Handbook of Industrial Drying. CRC Press (2014)

Naillon, A., Joseph, P., Prat, M.: Ion transport and precipitation kinetics as key aspects of stress generation on pore walls induced by salt crystallization. Phys. Rev. Lett. 120, 34502 (2018). https://doi.org/10.1103/PhysRevLett.120.034502

Nowicki, S.C., Davis, H.T., Scriven, L.E.: Microscopic determination of transport parameters in drying porous media. Dry. Technol. 10, 925–946 (1992). https://doi.org/10.1080/07373939208916488

Øren, P.E., Bakke, S., Arntzen, O.J.: Extending predictive capabilities to network models. SPE J. 3, 324–335 (1998). https://doi.org/10.2118/52052-pa

Ouedraogo, F., Cherblanc, F., Naon, B., Bénet, J.C.: Water transfer in soil at low water content: Is the local equilibrium assumption still appropriate? J. Hydrol. 492, 117–127 (2013). https://doi.org/10.1016/j.jhydrol.2013.04.004

Patankar, S.: Numerical Heat Transfer and Fluid Flow. CRC Press (1980)

Pel, L., Brocken, H., Kopinga, K.: Determination of moisture diffusivity in porous media using moisture concentration profiles. Int. J. Heat Mass Transf. 39, 1273–1280 (1996). https://doi.org/10.1016/0017-9310(95)00201-4

Pel, L., Huinink, H., Kopinga, K.: Ion transport and crystallization in inorganic building materials as studied by nuclear magnetic resonance. Appl. Phys. Lett. 81, 2893–2895 (2002)(a). https://doi.org/10.1063/1.1512329

Pel, L., Landman, K.A., Kaasschieter, E.F.: Analytic solution for the non-linear drying problem. Int. J. Heat Mass Transf. (2002)(b). https://doi.org/10.1016/S0017-9310(02)00025-X

Pel, L., Pishkari, R., Casti, M.: A simplified model for the combined wicking and evaporation of a NaCl solution in limestone. Mater. Struct. Constr. 51, 1–10 (2018). https://doi.org/10.1617/s11527-018-1187-y

Philip, J.R., De Vries, D.A.: Moisture movement in porous materials under temperature gradients. Trans. Am. Geophys. Union. 38, 222 (1957). https://doi.org/10.1029/TR038i002p00222

Plourde, F., Prat, M.: Pore network simulations of drying of capillary porous media. Influence of thermal gradients. Int. J. Heat Mass Transf. 46, 1293–1307 (2003). https://doi.org/10.1016/S0017-9310(02)00391-5

Plumb, O.A., Gu, L., Webb, S.W.: Drying of porous materials at low moisture content. Dry. Technol. 17, 1999–2011 (1999). https://doi.org/10.1080/07373939908917669

Prat, M.: Recent advances in pore-scale models for drying of porous media. Chem. Eng. J. 86, 153–164 (2002). https://doi.org/10.1016/S1385-8947(01)00283-2

Prat, M.: On the influence of pore shape, contact angle and film flows on drying of capillary porous media. Int. J. Heat Mass Transf. 50, 1455–1468 (2007). https://doi.org/10.1016/j.ijheatmasstransfer.2006.09.001

Prat, M., Agaësse, T.: Thin porous media. In: Vafai, K. (ed.) Handbook of Porous Media. pp. 89–112. CRC Press (2015)

Prat, M., Bouleux, F.: Drying of capillary porous media with a stabilized front in two dimensions. Phys. Rev. E. 60, 5647–5656 (1999). https://doi.org/10.1103/PhysRevE.60.5647

Pujol, A., Debenest, G., Pommier, S., Quintard, M., Chenu, D.: Modeling composting processes with local equilibrium and local non-equilibrium approaches for water exchange terms. Dry. Technol. 29, 1941–1953 (2011). https://doi.org/10.1080/07373937.2011.599506

R. W. Schrage: A Theoretical Study of Interphase Mass Transfer. Columbia Univ. Press, New York (1953)

Rahimi, A.: Discrete modeling of drying induced ion transport and crystallization in porous media (Doctoral thesis), Otto-von-Guericke-Universität Magdeburg, Germany, (2019)

Rahimi, A., Metzger, T., Kharaghani, A., Tsotsas, E.: Interaction of droplets with porous structures: Pore network simulation of wetting and drying. Dry. Technol. 34, 1129–1140 (2016). https://doi.org/10.1080/07373937.2015.1099106

Rijniers, L.A., Pel, L., Huinink, H.P., Kopinga, K.: Salt crystallization as damage mechanism in porous building materials: A nuclear magnetic resonance study. Magn. Reson. Imaging. 23, 273–276 (2005). https://doi.org/10.1016/j.mri.2004.11.023

Scherer, G.W.: Stress from crystallization of salt. Cem. Concr. Res. 34, 1613–1624 (2004). https://doi.org/10.1016/j.cemconres.2003.12.034

Schlünder, E.-U.: On the mechanism of the constant drying rate period and its relevance to diffusion controlled catalytic gas phase reactions. Chem. Eng. Sci. 43, 2685–2688 (1988). https://doi.org/10.1016/0009-2509(88)80012-5

Schoeber, W.J.A..: Regular regimes in sorption processes: Calculation of drying rates and determination of concentration dependent diffusion coefficients (Doctoral thesis), Eindhoven, the Netherlands: Technical University. (1976). https://doi.org/10.6100/IR130384

Sghaier, N., Prat, M.: Effect of efflorescence formation on drying kinetics of porous media. Transp. Porous Media. 80, 441–454 (2009). https://doi.org/10.1007/s11242-009-9373-6

Sghaier, N., Prat, M., Ben Nasrallah, S.: On the influence of sodium chloride concentration on equilibrium contact angle. Chem. Eng. J. 122, 47–53 (2006). https://doi.org/10.1016/j.cej.2006.02.017

Sghaier, N., Prat, M., Nasrallah, S. Ben: On ions transport during drying in a porous medium. Transp. Porous Media. 67, 243–274 (2007). https://doi.org/10.1007/s11242-006-9007-1

Shahidzadeh-Bonn, N., Desarnaud, J., Bertrand, F., Chateau, X., Bonn, D.: Damage in porous media due to salt crystallization. Phys. Rev. E. 81, 066110 (2010). https://doi.org/10.1103/PhysRevE.81.066110

Sheng, Q.: Pore-to-continuum multiscale modeling of two-phase flow in porous media (Doctoral thesis), Louisiana State University and Agricultural and Mechanical College, (2013).

Sherwood, T.K.: The drying of solids, Part 1. Ind. Eng. Chem. 21, 12–16 (1929). https://doi.org/10.1021/ie50229a004

Shokri-Kuehni, S.M.S., Bergstad, M., Sahimi, M., Webb, C., Shokri, N.: Iodine k-edge dual energy imaging reveals the influence of particle size distribution on solute transport in drying porous media. Sci. Rep. 8, 1–9 (2018). https://doi.org/10.1038/s41598-018-29115-0

Shokri, N.: Pore-scale dynamics of salt transport and distribution in drying porous media. Phys. Fluids. 26, (2014). https://doi.org/10.1063/1.4861755

Stauffer, D., Aharony, A.: Introduction to Percolation Theory. CRC Press (2018)

Surasani, V.K., Metzger, T., Tsotsas, E.: Consideration of heat transfer in pore network modelling of convective drying. Int. J. Heat Mass Transf. 51, 2506–2518 (2008). https://doi.org/10.1016/j.ijheatmasstransfer.2007.07.033

Talbi, M., Prat, M.: About Schlünder's model: A numerical study of evaporation from partially wet surfaces. Dry. Technol. 37, 513–524 (2019). https://doi.org/10.1080/07373937.2018.1506929

Thiery, J., Rodts, S., Weitz, D.A., Coussot, P.: Drying regimes in homogeneous porous media from macro- to nanoscale. Phys. Rev. Fluids. 2, 1–15 (2017). https://doi.org/10.1103/PhysRevFluids.2.074201

Veran-Tissoires, S., Prat, M.: Evaporation of a sodium chloride solution from a saturated porous medium with efflorescence formation. J. Fluid Mech. 749, 701–749 (2014). https://doi.org/10.1017/jfm.2014.247

Vorhauer, N., Metzger, T., Tsotsas, E.: Empirical macroscopic model for drying of porous media based on pore networks and scaling theory. Dry. Technol. 28, 991–1000 (2010). https://doi.org/10.1080/07373937.2010.497088

Vorhauer, N., Tsotsas, E., Prat, M.: Drying of thin porous disks from pore network simulations. Dry. Technol. 36, 651–663 (2018). https://doi.org/10.1080/07373937.2017.1319853

Vorhauer, N., Wang, Y.J., Kharaghani, A., Tsotsas, E., Prat, M.: Drying with formation of capillary rings in a model porous medium. Transp. Porous Media. 110, 197–223 (2015). https://doi.org/10.1007/s11242-015-0538-1

Vu, H.T., Tsotsas, E.: A framework and numerical solution of the drying process in porous media by using a continuous model. Int. J. Chem. Eng. 2019, (2019). https://doi.org/10.1155/2019/9043670

Wang, J.P., Lambert, P., De Kock, T., Cnudde, V., François, B.: Investigation of the effect of specific interfacial area on strength of unsaturated granular materials by X-ray tomography. Acta Geotech. 2, (2019). https://doi.org/10.1007/s11440-019-00765-2

Whitaker, S.: Simultaneous heat, mass, and momentum transfer in porous media: A theory of drying. Adv. Heat Transf. 13, 119–203 (1977). https://doi.org/10.1016/S0065-2717(08)70223-5

Whitaker, S.: Flow in porous media, Part 2: The governing equations for immiscible, two-phase flow. Transp. Porous Media. 1, 105–125 (1986). https://doi.org/10.1007/BF00714688

Whitaker, S.: The Method of Volume Averaging. Springer Science & Business Media (2013)

Wilkinson, D.: Percolation effects in immiscible displacement. Phys. Rev. A. 34, 1380–1391 (1986). https://doi.org/10.1103/PhysRevA.34.1380

Yiotis, A.G., Boudouvis, A.G., Stubos, A.K., Tsimpanogiannis, I.N., Yortsos, Y.C.: Effect of liquid films on the isothermal drying of porous media. Phys. Rev. E. 68, 037303 (2003). https://doi.org/10.1103/PhysRevE.68.037303

Yiotis, A.G., Boudouvis, A.G., Stubos, A.K., Tsimpanogiannis, I.N., Yortsos, Y.C.: Effect of liquid films on the drying of porous media. AIChE J. 50, 2721–2737 (2004). https://doi.org/10.1002/aic.10265

Yiotis, A.G., Salin, D., Tajer, E.S., Yortsos, Y.C.: Drying in porous media with gravity-stabilized fronts: Experimental results. Phys. Rev. E. 86, 026310 (2012). https://doi.org/10.1103/PhysRevE.86.026310

Appendix A: Simulation parameters

Table A.1: Physical properties or materials used in simulations at temperature of 293.15 K and pressure of 1 atm.

Physical property	**Unit**	**Value**
Air-vapor binary diffusion coefficient	m^2/s	2.56×10^{-5}
Vapor pressure in bulk air	Pa	0
Equilibrium vapor partial pressure	Pa	2339
Molar mass of water vapor	kg/kmol	18.02
Surface tension between water and air	N/m	0.07274
Universal gas constant	J/kmolK	8314.5
Solute diffusion coefficient (pore scale)	m^2/s	1×10^{-9}

Table A.2: Structure and fluid physical parameters used for simulations in Chapter 3. The right most column shows the parameters used for the simulation results illustrated in Fig. 3.8.

Parameter	**Unit**	**Chapter 3**	**Fig. 3.8**
Network size (nodes)	-	25×25×50	25×25×50
Boundary layer discretization	-	25×25×4	25×25×4
Boundary layer thickness	mm	4	4
Mean throat radius	mm	0.25	0.25
Standard deviation of throat radius	mm	0.025	0.025
Throat length	mm	1	1
Network porosity	-	0.594	0.594
Initial network saturation	-	0.26	0.24, 0. 20, 0.14, 0.08
Number of realizations	-	45	15 each

Table A.3: Structure and fluid physical parameters used for simulations in Chapter 4.

Parameter	**Unit**	**Chapter 4**
Network size (nodes)	-	25×25×51
Boundary layer discretization	-	25×25×10
Boundary layer thickness	mm	10
Mean throat radius	mm	0.25
Standard deviation of throat radius	mm	0.025
Throat length	mm	1
Network porosity	-	0.594
Initial network saturation	-	1
Number of realizations	-	15
Viscosity of liquid phase	m^2/s	0.028

Table A.4: Simulation parameters used in Chapter 5 with distinction with respect to the corresponding chapter sections.

Parameter	**Unit**	**Sec. 5.2 - 5.4**	**Sec. 5.5**
Network size (nodes)	-	25×25×25	25×25×25
Imposed drying rate	$kg/m^2/s$	3.025×10^{-6}	3.025×10^{-6}
Mean throat radius	mm	0.25	0.25
Standard deviation of throat radius	mm	0.025	0.025
Throat length	mm	1	1
Network porosity	-	0.594	0.594
Initial network saturation	-	1	1
Number of realizations	-	15	70
Initial Péclet number	-	0.2	0.2
Initial solute concentration	kg/m^3	10	10
Threshold solute concentration	kg/m^3	-	50

Student works

The following student work was conducted within the framework of this thesis:

1. Aliasghar Hajhariri, Characterization of liquid structure and solute concentration profiles in capillary-dominated drying regime. Master thesis, chair of thermal process engineering, Otto von Guericke University Magdeburg, Magdeburg, February, 2020.

Publications and presentations

Own publications and presentations related to this thesis in national and international journals and conferences are listed the following.

Publications in national and international journals

1. Ahmad, F., Talbi, M., Prat, M., Tsotsas, E., Kharaghani, A. Non-local equilibrium continuum modeling of partially saturated drying porous media: Comparison with pore network simulations. Chemical Engineering Science, 228, 115957 (2020).
2. Ahmad, F., Rahimi, A., Tsotsas, E., Prat, M., Kharaghani, A. From micro-scale to macro-scale modeling of solute transport in drying capillary porous media. International Journal of Heat and Mass Transfer, 165, 120722 (2021).
3. Ahmad, F., Prat, M., Tsotsas, E., Kharaghani, A. Two-equation continuum model of drying appraised by comparison with pore network simulations. Submitted to a peer-reviewed journal.

Oral and poster presentations in national and international conferences

1. Ahmad, F., Kharaghani, A., Tsotsas, E., Prat, M. Two-equation continuum model of drying: A limiting case of immobile phase. Oral presentation in Interpore 2019, 06 - 10 May, 2019, Valencia, Spain.
2. Ahmad, F., Kharaghani, A., Prat, M., Tsotsas, E. Advanced modeling of the drying process in porous media. Oral presentation in Jahrestreffen der ProcessNet-Fachgruppen Wärme- und Stoffübertragung, Trocknungstechnik und Mischvorgänge, 18. - 20 March, 2019, Essen, Germany.
3. Ahmad, F., Rahimi, A., Kharaghani, A., Prat, M., Tsotsas, E. Modeling and simulations of solute transport in drying porous media. Oral presentation in 4th Indo-German Workshop on Advances in materials, reaction & separation processes, 23 - 26 February, 2020, Berlin, Germany.

4. Ahmad, F., Rahimi, A., Prat, M., Kharaghani, A., Tsotsas, E. Insights on solute transport in drying porous media gained from discrete and continuum model simulations. Poster presentation in Jahrestreffen der ProcessNet-Fachgruppe Wärme- und Stoffübertragung 12. - 13. March, 2020, Erfurt, Germany.
5. Ahmad, F., Rahimi, A., Prat, M., Tsotsas, E., Kharaghani, A. Transition from micro-scale to macro-scale modeling of solute transport in drying porous media. Pre-recorded online video presentation in Interpore 2020, 31 August - 04 September, 2020, Online.